Study of Muonic Decays of Doubly Charged Higgs Bosons with the CMS Detector

by

Tanja Rommerskirchen

Diploma Thesis in Physics

presented to the

Faculty for Mathematics, Computer Science and Natural Sciences
of Aachen University, Germany

in June 2006

performed in the

III. Physics Institute A
Prof. Dr. Thomas Hebbeker

Abstract

An analysis of the discovery potential of doubly charged Higgs bosons at the CMS detector is presented in this diploma thesis. Investigated are doubly charged Higgs bosons, which are pair produced through the Drell-Yan mechanism, in pp collisions at $\sqrt{s} = 14$ TeV. The decay branching ratio into muon pairs is assumed to be 100%. The pure muonic decay channel yields a clear signal which is almost free of background. Doubly charged Higgs bosons with masses in the range 100 to 900 GeV are studied, for a low luminosity scenario of $\mathcal{L} = 2 \times 10^{33}\mathrm{cm}^{-2}\mathrm{s}^{-1}$. The full detector simulation is used. Doubly charged Higgs bosons in this production and decay channel with masses $m_{H^{\pm\pm}} \leq 650$ GeV are expected to be observable at CMS with a significance exceeding 5σ at $10fb^{-1}$ of integrated luminosity. If no signal will be detected for this integrated luminosity, the existence of a doubly charged Higgs Boson with $m_{H^{\pm\pm}} \leq 760$ GeV can be excluded at 95% confidence level. This exceeds the current exclusion limit $m_{H^{\pm\pm}} \leq 136$ GeV, set by CDF at Tevatron Run II, by 624 GeV.

Contents

Chapter 1

Introduction

Particle Physics is fundamental research. Its purpose is to find the smallest constituents of matter and to understand the forces between them.

The basic building blocks of particle physics are summarized in the Standard Model. It retraces the complexity of particle interactions found in several experiments to a few fundamental symmetries, called local gauge symmetries. In the Standard Model particles interact by exchanging gauge bosons. For example, in weak interactions the W and Z bosons are exchanged. One of the problems of gauge theories is that they predict massless W and Z bosons, which is a contradiction to results from collider experiments.

One of the simplest ways of explaining massive gauge bosons and keeping the concept of gauge theories as well is the Higgs mechanism. It predicts an additional particle, which is called Higgs boson. By interacting with this Higgs boson the particles acquire their mass.

One of the aims of the future Large Hadron Collider (LHC) at the particle research center CERN, is to collide particles with energies high enough to make the generation of Higgs bosons possible. The task of the Compact Muon Solenoid (CMS) detector at the LHC is to discover this Higgs boson, or to exclude its existence.

Except for simplicity there are no reasons why there cannot be more than one Higgs boson. Some models like the "Left-Right Symmetric Model" and the "Higgs Triplet Model" (HTM) introduce a more complex Higgs sector, with several Higgs bosons including a doubly charged Higgs boson. These Higgs triplet models can give an answer to the question why neutrinos are not massless as assumed in the Standard Model. The detection of a doubly charged Higgs boson would provide evidence for these Higgs triplet models.

Previous searches at lepton and hadron colliders excluded the existence of doubly charged Higgs boson with masses smaller than 136 GeV. The future LHC will be able to collide protons with a centre of mass energy of 14 TeV. Therefore it will extent the current exclusion mass limit to a much higher value or discover the doubly charged Higgs boson.

This diploma thesis studies the possible generation of pair produced doubly charged Higgs bosons with the LHC and the feasibility of finding or excluding the existence of these particles with the CMS detector.

The thesis starts with an introduction to the theory of particle physics presenting the Standard Model and models beyond. Chapters 4 and 5 describe the experimental setup used in this analysis, the "hardware" and "software" of the CMS detector. In chapters 6 to 9 the possibility of distinguishing signal and background with several selection criteria is studied. The remaining signal and background events after the final selection are analyzed in a statistical way in chapter 10. Mass limits for the discovery or exclusion of the signal are obtained. The uncertainties of these mass limits are finally discussed in chapter 11.

Chapter 2

The Standard Model

The Standard Model is the established theory of particle physics. It deals with physics at scales smaller than 1 fm. At such distances even protons and neutrons, the constituents of atomic nuclei, do not appear as pointlike, but can be found to consist of other particles, the so called quarks. Until now no substructure of quarks has been discovered. Therefore they are assumed to be elementary particles. Electrons, surrounding atomic nuclei, are another kind of particles which are assumed as elementary. The electron belongs to a class of particles called leptons. Quarks and leptons are spin 1/2 particles, called fermions. An overview over the fundamental fermions in the Standard Model is given in Table 2.1.

	family			electrical charge
	I	II	III	$[e]$
leptons	e	μ	τ	1
	ν_e	ν_μ	ν_τ	0
quarks	u	c	t	2/3
	d	s	b	-1/3

Table 2.1: The different fermions and their electrical charges

As shown in this table, fermions can be subdivided into so called families. The particle mass increases from one family to the next, but charge and other intrinsic particle properties stay the same.

To each of these fermions belongs an anti-particle with opposite quantum numbers, like the charge, but the same mass.

The forces between fermions are carried by particles with an integer spin, the gauge bosons. Table 2.2 shows the fundamental forces, the corresponding gauge bosons and the fermions which interact with these gauge bosons.

Except the gravitational force, all fundamental forces are described by the Standard Model. The gravitational force is very weak, and plays therefore no role at the scales of particle physics. Furthermore, the graviton has not been detected yet, and the opinions about its existence are controversial.

force	gauge bosons	fermions
strong	gluon	quarks
weak	W and Z boson	all fermions
electromagnetic	photon	all charged fermions
gravity	"graviton"	all fermions

Table 2.2: The fundamental forces, the corresponding gauge bosons, and the fermions which interact with these bosons

As the Standard Model is a relativistic quantum field theory, fermions are substituted by four-component wave functions $\psi(\vec{x},t)$. The four components of $\psi(\vec{x},t)$ correspond to particles and anti-particles with the two possible spin projections $\pm 1/2$. Instead of $\psi(\vec{x},t)$, which is a function of space and time, the state of a particle can also be defined as a function of its momentum and energy.

Spin and momentum of a particle can be combined to form another quantity, the helicity λ. The helicity is the projection of the spin $\vec{s}$ onto the momentum $|\vec{p}|$.

$$\lambda = \vec{s} \cdot \vec{p} / |\vec{p}| \tag{2.1}$$

The helicity of massless particles is invariant under a Lorentz boost. In the special case of massless particles the helicity of a particle can be identified with its chirality. Chirality projection operators separate the wave function of a particle into a "left" and a "right handed" component. Massive particles can change their helicity under a Lorentz boost, but their chirality stays the same.

The interactions between fermions and bosons are described by gauge theories. The next subchapter explains the concept of gauge theories at the example of Quantum ElectroDynamics (QED), further information about gauge theories and the Standard Model can be found in [2] and [3].

2.1 QED and symmetries

In QED, the equation of motion for a free fermion is the Dirac equation.

$$(i\gamma^\mu \partial_\mu - m)\,\psi = 0, \tag{2.2}$$

where γ^μ are the 4×4 γ-matrices. An equivalent way of describing the propagation is via the Lagrangian:

$$\mathcal{L} = \bar{\psi}\,(i\,\gamma^\mu\,\partial_\mu - m)\,\psi \tag{2.3}$$

Gauge theories like QED are build upon local gauge symmetries.
What is meant by symmetry?
Feynman: "A thing is symmetrical, if there is something we can do to it so that after we have done it, it looks the same as before."
Adapted to gauge theories this means, that if a system is symmetrical under a certain

operation, this operation should not change the equation of motion. If ψ is a solution to the Dirac equation, the transformed $\psi' = U\psi$, where U is the symmetry operator, should also be a solution.

A special kind of transformations are gauge transformations. A gauge transformation transforms the phase factor of a wave function.

$$\psi \rightarrow \psi' = U\,\psi \qquad U = e^{i\,Q\,\alpha}, \tag{2.4}$$

where Q is the fermion charge. The important thing about gauge theories like QED is, that they require the Lagrangian to be invariant under local gauge transformations. For local gauge transformations the phase factor α depends upon space and time.

If the transformed ψ is inserted into the Lagrangian (2.3), an additional term proportional to the derivative of α will be produced. To cancel this term and keep the Lagrangian invariant under gauge transformations, the covariant derivative D^μ with a new field A^μ is introduced:

$$\partial^\mu \Rightarrow D^\mu = \partial^\mu + i\,Q\,A^\mu \tag{2.5}$$

where A^μ transforms as:

$$A_\mu \rightarrow A'_\mu = A_\mu - \partial_\mu\,\alpha(x), \tag{2.6}$$

Thus the additional term in the Lagrangian is cancelled. A_μ is associated with the photon field.

The gauge transformation U(α) forms a mathematical group, U(1). In the following this U(1) group will be called U$(1)_{em}$, to distinguish it from other U(1) gauge groups.

It is also possible to require invariance against local gauge transformations with respect to more complex groups, for example the SU(3) group in the gauge theory of strong interactions, Quantum ChromoDynamics (QCD).

2.2 QCD

QCD is the theory of strong interactions between quarks and gluons. The knowledge about QCD is therefore crucial for the understanding of physics at proton-proton colliders like the LHC.

To each quark a charge called colour is attributed. The possible colours are red, green and blue for quarks and antired, antigreen and antiblue for antiquarks. Detectable particles have to be colour neutral. Thus a detectable particle has to consist of at least three quarks in red, green and blue, or of a quark and an antiquark of a certain colour and its corresponding anticolour. A single quark can not be colour neutral and hence can not exist separated.

The Lagrangian which describes a free quark is:

$$\mathcal{L} = \bar{q}\,(i\;\gamma^\mu\,\partial_\mu - m)\,q \tag{2.7}$$

Where q is a colour triplet of wave functions:

$$q = (q_{red},\, q_{green},\, q_{blue}) \tag{2.8}$$

The requirement of invariance against local gauge transformations becomes in this theory a requirement of invariance against colour transformations for a SU(3) group. The operator $U(x)$ looks like:

$$U(x) = e^{i\, g\, \theta_s(x)\, t^s}, \tag{2.9}$$

where g is the equivalent to the charge in QED and determines the strength of the coupling. t^s are the generators of the SU(3) group. They can be represented as 8 linear independent matrices. The generators behave like:

$$t^r\, t^s - t^s\, t^r = i\, f_t^{r\,s} t^t, \tag{2.10}$$

where $f_t^{r\,s}$ are totally antisymmetric SU(3) structure-constants. So in general neither the generators nor the corresponding operators $U(x)$ commute.

To make the QCD Lagrangian invariant under local gauge transformations, one has to introduce a covariant derivative and new fields, the gluon fields G_μ.

$$D^\mu = \partial^\mu + i t_s\, G^{s,\mu}. \tag{2.11}$$

The gluon field transforms like:

$$t_r\, G_\mu^r \rightarrow U\, (t_r\, G_\mu^r)\, U^{-1} - \frac{1}{g}\, U\, \partial_\mu\, U^{-1} \tag{2.12}$$

These gluon fields can be associated with the gluons.

One difference between QED and QCD is, that the gauge bosons of QCD couple with equal strength to all types of quarks, whereas the gauge boson of QED couples with different strength to fermions with different charges.

A consequence of the non-commuting operators in QCD are terms in the Lagrangian which are proportional to G^3 and G^4. This corresponds to three and four gluon interactions. In contrast to the photons in QED, gluons can interact with other gluons. Self-interacting gluons lead to a weaker coupling for higher energies. This is called asymptotic freedom. For reactions where a huge momentum is transferred, quarks behave as almost free particles.

As mentioned before quarks can only exist in colour neutral combinations, due to the strong force. The strong force between the quarks increases with the distance between the quarks. If the energy of the force field gets high enough, a new colour neutral pair of quarks is produced. Together with the initial quarks the produced quarks can form new particles. This is called fragmentation or hadronization.

Another gauge theory is the Glashow-Salam-Weinberg (GSW) theory, which combines the description of electromagnetic and weak interactions.

2.3 Electroweak Interactions

One example of a weak interaction is the β-decay in which a neutron decays to a proton, an electron and an anti-neutrino.
An important property of weak interactions is, that left and right handed particles interact differently. This implies parity violation. The parity operator P basically exchanges left and right handed fields. Electroweak interactions are not symmetric under parity transformation, and therefore there is a difference in the interaction of left and right handed fields. The simplest gauge-group which can explain the measured properties of weak interactions is SU(2)×U(1). The gauge fields corresponding to the SU(2) group are called W^1, W^2, W^3, and the gauge field corresponding to the U(1) group is called B.

The SU(2) gauge fields couple only to left handed fermions while the U(1) field couples to left and right handed fermions. In order to coincide with observations, fermions can be arranged as multiplets of the weak isospin I:

Doublets ($I = 1/2$) of chiral left handed fields:

$$L: \quad \begin{pmatrix} \nu_e \\ e^- \end{pmatrix}_L \quad \begin{pmatrix} \nu_\mu \\ \mu^- \end{pmatrix}_L \quad \begin{pmatrix} \nu_\tau \\ \tau^- \end{pmatrix}_L \quad \begin{pmatrix} u \\ d \end{pmatrix}_L \quad \begin{pmatrix} c \\ s \end{pmatrix}_L \quad \begin{pmatrix} t \\ b \end{pmatrix}_L \tag{2.13}$$

The third component I_3 of the weak isospin I equals $1/2$ for the upper components of the doublets and $-1/2$ for the lower components.

Singlets ($I = 0$) of chiral right handed fields:

$$R: \quad e^-_{\mathrm{R}} \quad \mu^-_{\mathrm{R}} \quad \tau^-_{\mathrm{R}} \quad u_{\mathrm{R}} \quad d_{\mathrm{R}} \quad c_{\mathrm{R}} \quad s_{\mathrm{R}} \quad t_{\mathrm{R}} \quad b_{\mathrm{R}} \tag{2.14}$$

There are no wave functions in the Standard Model for right handed neutrinos. They have no charge, so they do not interact electromagnetically and no right handed neutrinos have been found in weak interactions. As they seem not to interact at all, they are assumed to be non-existent in the Standard Model[1].

The local gauge transformations, for left handed wave functions ψ_L and right handed wavefunctions ψ_R, are:
For U(1):

$$\psi_L \to e^{i\,(g'/2)\,Y_L\,\alpha(x)}\,\psi_L \qquad \psi_R \to e^{i\,(g'/2)\,Y_R\,\alpha(x)}\,\psi_R, \tag{2.15}$$

where g' is the general gauge coupling for U(1) and Y_L and Y_R determine the different coupling strengths for left and right handed fermions, they are called weak hypercharges.

For SU(2):

$$\psi_L \to e^{i\,(g/2)\,\vec{\sigma}\,\cdot\,\vec{\beta}(x)}\,\psi_L, \tag{2.16}$$

where $\vec{\sigma}$ is a vector of the three Pauli matrices and g is the general gauge coupling for SU(2).

[1] Some theories predict the existence of so called sterile neutrinos, which do not interact. These neutrinos might explain the non-vanishing neutrino mass

To emphasize the relation between the gauge groups and the hypercharge and isospin, SU(2)×U(1) is often written as $\mathrm{SU}(2)_L \times \mathrm{U}(1)_Y$.
The Gell-Mann-Nishijima-Relation between Y and I_3 is:

$$Q = \frac{Y}{2} + I_3, \tag{2.17}$$

where Q is the measured electromagnetic charge.

The Lagrangian for free Dirac fields can be written as:

$$\mathcal{L} = i\,\bar{\psi_L}\,\gamma^\mu\,\partial_\mu\,\psi_L + i\,\bar{\psi_R}\,\gamma^\mu\,\partial_\mu\,\psi_R. \tag{2.18}$$

To make this Lagrangian invariant under $\mathrm{SU}(2)_L$ and $\mathrm{U}(1)_Y$ gauge transformations the derivative ∂_μ is substituted by the covariant derivative D_μ:

$$D_\mu = \partial_\mu + i\,g\,I\,\vec{\sigma}\cdot\vec{W}_\mu + i\,\frac{g'}{2}\,Y\,B_\mu, \tag{2.19}$$

where ψ is the wave function of a fermion. ψ can be symbolically denoted by:

$$\psi = \begin{pmatrix} \nu_{e\mathrm{L}} \\ e_{\mathrm{L}} \\ \vdots \\ t_{\mathrm{R}} \end{pmatrix} \tag{2.20}$$

The W and B fields can be linearly combined to the A^μ field, which is associated with the photon, and to the Z^μ field, which is associated with the Z boson.

$$A^\mu = \cos(\theta_W)\cdot B^\mu + \sin(\theta_W)\cdot W^{3,\mu} \qquad Z^\mu = -\sin(\theta_W)\cdot B^\mu + \cos(\theta_W)\cdot W^{3,\mu} \tag{2.21}$$

Since photons shouldn't couple to neutrinos, the so called "Weinberg-Angle" has to solve the following equations:

$$\cos(\theta_W) = \frac{g}{\sqrt{g^2+g'^2}} \qquad \sin(\theta_W) = \frac{g'}{\sqrt{g^2+g'^2}} \tag{2.22}$$

The resulting part of the Lagrangian which corresponds to electromagnetic currents is:

$$\mathcal{L} = \cdots + \sqrt{g^2+g'^2}\,\cos(\theta_W)\,\sin(\theta_W)\left(\bar{e}_L\,\gamma^\mu\,e_{\mathrm{L}} - \frac{Y_R}{2}\,\bar{e}_R\,\gamma^\mu\,e_{\mathrm{R}}\right)A_\mu \tag{2.23}$$

In electromagnetic interactions there is no difference between left and right handed currents, therefore:

$$\Rightarrow Y_R = -2 \tag{2.24}$$

The coupling strength of the photon is determined by the electric charge Q.

$$\Rightarrow Q = \sqrt{g^2+g'^2}\,\cos(\theta_W)\,\sin(\theta_W) \tag{2.25}$$

The resulting part of the Lagrangian for neutral weak currents is:

$$\begin{aligned} \mathcal{L} \;=\; \cdots \;+\; & \frac{Q}{\cos(\theta_W)\sin(\theta_W)} \\ & \cdot\;\left(-\frac{1}{2}\,\bar{\nu}_{\mathrm{L}}\,\gamma^\mu\,\nu_{\mathrm{L}} + \frac{1}{2}\,\bar{e}_{\mathrm{L}}\,\gamma^\mu\,e_{\mathrm{L}} + \sin^2(\theta_W)\,\bar{e}_{\mathrm{L}}\,\gamma^\mu\,e_{\mathrm{L}} + \sin^2(\theta_W)\,\bar{e}_{\mathrm{R}}\,\gamma^\mu\,e_{\mathrm{R}}\right)Z_\mu \end{aligned} \tag{2.26}$$

W^1 and W^2 can be combined to the force carriers of charged weak currents W^+ and W^-.

$$W^+ = (W^1 + iW^2)/\sqrt{2} \qquad W^- = (W^1 - iW^2)/\sqrt{2} \tag{2.27}$$

The part of the Lagrangian for charged weak currents becomes:

$$\begin{aligned} \mathcal{L} \;=\; \cdots \;-\; & \frac{Q}{\sqrt{2}\sin(\theta_W)}\,\bar{\nu}_{\mathrm{L}}\,\gamma^\mu\,e_{\mathrm{L}}\,W^+_\mu \\ -\; & \frac{Q}{\sqrt{2}\sin(\theta_W)}\,\bar{e}_{\mathrm{L}}\,\gamma^\mu\,\nu_{\mathrm{L}}\,W^-_\mu \end{aligned} \tag{2.28}$$

So far W and Z bosons are assumed to be massless, this is disproved by experiments. Nevertheless, a possible inclusion of mass-terms:

$$m_B^2 B^\mu B_\mu, \tag{2.29}$$

in the Lagrangian would break the gauge invariance. Another way has to be found. The way chosen in the Standard Model is the Higgs mechanism.

2.4 Higgs-Mechanism

In order to give mass to W and Z bosons, two complex valued scalar fields in an isospin doublet ϕ are introduced:

$$\phi = \begin{pmatrix} \phi^+ \\ \phi^0 \end{pmatrix} \qquad (I = 1/2, Y = 1), \tag{2.30}$$

with the corresponding Lagrangian:

$$\mathcal{L} = (D_\mu\phi)^\dagger(D^\mu\phi) - V(\phi) \qquad V(\phi) = -\mu^2\phi^\dagger\phi + \lambda^2(\phi^\dagger\phi)^2 \tag{2.31}$$

D_μ is the already known covariant derivative of the GSW theory.

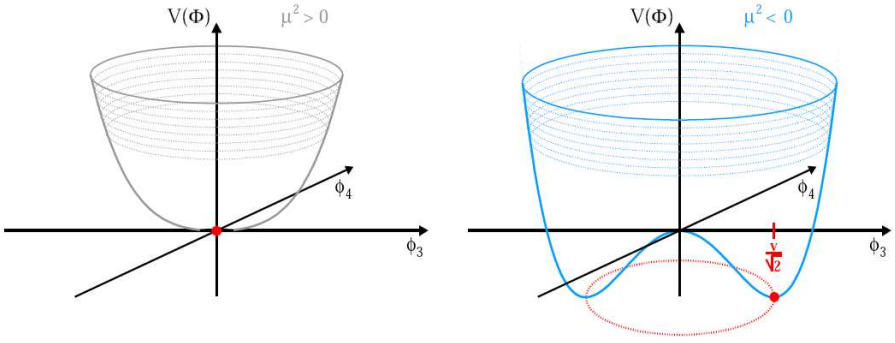

Figure 2.1: The Higgs Potential [4], for $\mu^2 > 0$ and $\mu^2 < 0$.

Figure 2.1, shows the potential of the Higgs field. A non trivial minimum exists only for $\mu^2 < 0$.

In this case the ground state is degenerate, a whole ring of minima exists, with the radius:

$$|\phi| \equiv \frac{v}{\sqrt{2}} = \sqrt{-\frac{\mu^2}{2\lambda^2}} \tag{2.32}$$

Arbitrarily the following state is chosen as ground state:

$$\phi_0 = \begin{pmatrix} 0 \\ \frac{v}{\sqrt{2}} \end{pmatrix} \quad \text{using} \quad v \equiv \frac{\mu}{\lambda}, \tag{2.33}$$

where $\nu/\sqrt{2}$ is the so called vacuum expectation value. The field can now be expanded around this ground state:

$$\phi = \frac{1}{\sqrt{2}} \cdot \begin{pmatrix} \xi_1 + i\xi_2 \\ v + \eta + i\varsigma \end{pmatrix}, \tag{2.34}$$

and inserted into the Lagrangian of equation 2.31, to obtain the interaction of this field with the gauge bosons W and Z.

ξ_1, ξ_2 and ς can be eliminated by a gauge transformation and η can be assumed as small. Therefore the Lagrangian becomes:

$$\mathcal{L} \approx \left[\frac{1}{2}\left(\partial^\mu \eta\right)\left(\partial_\mu \eta\right) - \mu^2\eta^2\right] + \frac{g^2v^2}{8}(\left|W_\mu^+\right|^2 + \left|W_\mu^-\right|^2) + \frac{g^2v^2}{8\,\cos^2(\theta_W)}\left|Z_\mu\right|^2 \tag{2.35}$$

This Lagrangian includes three mass-terms. The mass of the W boson is:

$$m_W = \frac{gv}{2} \tag{2.36}$$

The mass of the Z boson is:

$$m_Z = \frac{g\,v}{2\,\cos(\theta_W)} \tag{2.37}$$

The third mass term is the mass term of a new neutral scalar particle, the Higgs boson:

$$m_H = \sqrt{2}\,\mu \tag{2.38}$$

By the arbitrary choice of a special vacuum state the $\mathrm{SU}(2)_L$ and the $\mathrm{U}(1)_Y$ symmetry are broken. The vacuum is filled with a field, the Higgs field. Particles acquire mass by interacting with this field. The charged component of the chosen vacuum expectation value is zero, so the photon doesn't couple to the Higgs field and stays massless as required by experiment. The $\mathrm{U}(1)_{em}$ symmetry remains untouched.

This breaking scheme can be symbolically denoted by:

$$\mathrm{SU}(2)_L \times \mathrm{U}(1)_Y \xrightarrow{v} \mathrm{U}(1)_{em} \tag{2.39}$$

To explain fermion masses another term is added to the Lagrangian. This term describes the so called Yukawa coupling of fermions to the Higgs field.

$$\mathcal{L}_{Yukawa} = -\tilde{g}_f \left(\bar{R}\,(\phi^\dagger\, L) + (\bar{L}\,\phi)\, R\right) \tag{2.40}$$

Where L and R are the left handed fermion-doublet and the right handed fermion-singlet.

By inserting the different fermion families one gets the following coupling constants for the coupling of a fermion f to the Higgs field:

$$\tilde{g}_f = \sqrt{2}\,\frac{m_f}{v} \tag{2.41}$$

The coupling strength of fermions to the Higgs field is proportional to the fermion mass. The Yukawa coupling connects left handed and right handed fermion fields. As there are no right handed neutrinos in the Standard Model, neutrinos do not couple to the Higgs field and therefore gain no mass.

However recent neutrino oscillation experiments show that neutrinos have a tiny but non-zero mass. In order to explain these neutrino masses, the Standard Model has to be extended.

Chapter 3

Beyond the Standard Model

3.1 Neutrino Oscillations

The term "Neutrino Oscillation" describes the phenomenon that a neutrino of a certain flavour, for example ν_μ, changes into a neutrino of another flavour ν_e or ν_τ (for details see [5]). This is only possible if neutrinos have a non-vanishing mass, and their mass eigenstates are not equal to their flavour eigenstates. In this case the flavour eigenstates ν_α ($\alpha = e, \mu, \tau$) can be composed out of different mass eigenstates ν_i ($i = 1, 2, 3$) in the following way.

$$\nu_\alpha = U_{\text{MNS}}\, \nu_i \tag{3.1}$$

Where U_{UMNS} is a unitary matrix called the Maki-Nakagawa-Sakata-matrix (MNS matrix) and can be parametrized by three angles and one complex phase.

$$U_{\text{MNS}} = \begin{pmatrix} c_{12}c_{13} & s_{12}c_{13} & s_{13} \\ -s_{12}c_{23} - c_{12}s_{23}s_{13}e^{i\phi} & c_{12}c_{23} - s_{12}s_{23}s_{13}e^{i\phi} & s_{23}c_{13} \\ s_{12}s_{23} - c_{12}s_{23}s_{13}e^{i\phi} & -c_{12}s_{23} - s_{12}c_{23}s_{13}e^{i\phi} & c_{23}c_{13} \end{pmatrix} \tag{3.2}$$

Where $s_{ij} = \sin(\theta_{ij})$, $c_{ij} = \cos(\theta_{ij})$ (i,j = 1,2,3) and θ_{ij} are the three mixing angles.
The neutrino mass matrix elements m_{ij} of the flavour eigenstates are related to the masses m_i of the neutrino mass eigenstates by:

$$m_{ij} = U_{\text{MNS}}\; diag(m_1, m_2, m_3)\; U^T_{\text{MNS}}, \tag{3.3}$$

The neutrino mass eigenstates are stationary states and show a time dependence according to:

$$\nu_i(x,t) = e^{-iE_it}\nu_i(x,0), \tag{3.4}$$

where E is the neutrino energy. Using relation (3.1) and (3.4) the transition probability for a flavour conversion $\nu_\alpha \to \nu_\beta$ can be calculated. The transition probability depends on the square of the mass differences Δm^2_{ij} of the mass-eigenstates, on the mixing angles θ_{ij}, on the energy E of the neutrino and on the distance L the neutrino has travelled.

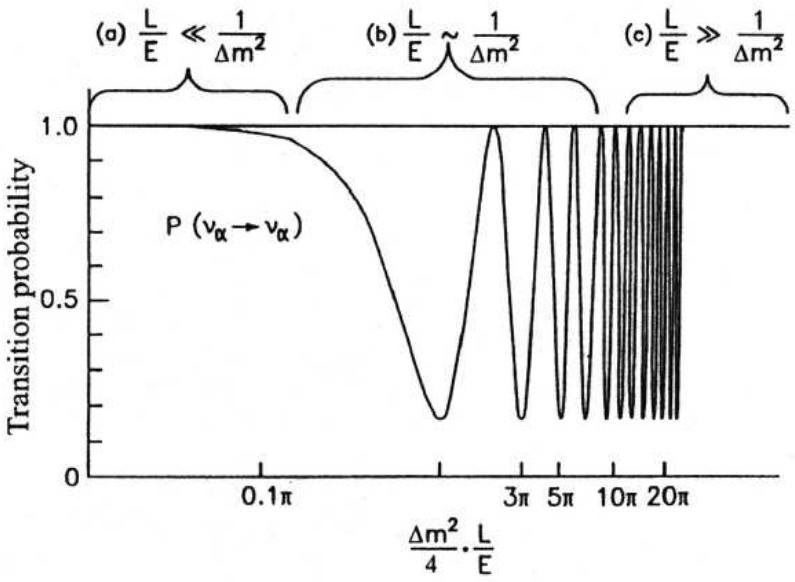

Figure 3.1: Logarithmic plot of the transition probability $P(\nu_\alpha \to \nu_\alpha)$ as a function of L/E for $\sin^2 2\theta = 0.83$. The brackets denote three possible cases: (a) no oscillation for $(L/E << 1/\Delta m^2)$; (b) oscillation $(L/E \approx 1/\Delta m^2)$ and (c) average oscillations for $(L/E >> 1/\Delta m^2)$ [5].

Figure 3.1 shows the transition probability $\mathrm{P}(\nu_\alpha \to \nu_\alpha)$ as a function of $\frac{\Delta m^2}{4}\frac{L}{E}$

Since an oscillation changes the flavour of the neutrino, such processes violate the lepton family number conservation. The number of electron, muon or tau neutrinos L_e, L_μ, L_τ changes, but $L = \Sigma L_i$ is still conserved.

Several oscillation experiments study the transition probability of neutrino flavours at a variety of energies and travelling distances to probe the different mixing angles and mass differences.

The most recent results from these studies are [6]:

- $\Delta m^2_{12} = (8.0 \pm 0.3)10^{-5} eV^2$
- $|\Delta m^2_{23}| = (2.5 \pm 0.3)10^{-3} eV^2$
- $\tan^2(\theta_{12}) = 0.45 \pm 0.05$
- $\sin^2(2\theta_{23}) = 1.02 \pm 0.04$
- $\sin^2(2\theta_{13}) = 0 \pm 0.05$

As oscillation experiments only determine mass differences, there are two possible mass hierarchies for three neutrino flavours, see Figure 3.2.

One possibility to explain neutrino masses is the Higgs Triplet Model (HTM).

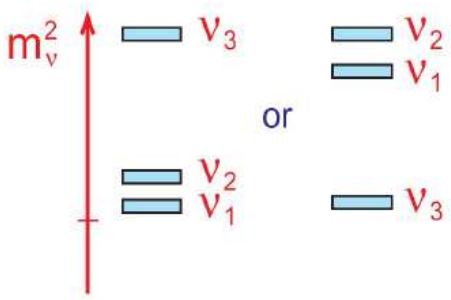

Figure 3.2: "Normal" and "inverted" mass hierarchy for three neutrino flavours [7].

3.2 Higgs Triplet Model

The Higgs Triplet Model [8] is a particularly simple model to explain the non-zero neutrino mass without introducing a right handed neutrino. In the Higgs Triplet Model a complex Higgs triplet $(\delta_1, \delta_2, \delta_3)$ with the quantum numbers $(I = 1, Y = 2)$ is added to the Standard Model Higgs sector. The Lepton number L is explictly violated in this model, by assigning $L = -2$ to the Higgs triplet. In common notation the Higgs triplet is written in a 2×2 representation $(\Delta \equiv \vec{\sigma} \cdot \vec{\delta})$.

$$\Delta \equiv \begin{pmatrix} \Delta^+/\sqrt{2} & \Delta^{++} \\ \Delta^0 & -\Delta^+/\sqrt{2} \end{pmatrix}, \tag{3.5}$$

where the charges of the matrix members are determined by the Gell-Mann-Nishijima-Relation:

$$Q\,\Delta = \left[\frac{\sigma_3}{2}, \Delta\right] + 1 \cdot \Delta \tag{3.6}$$

The triplet Higgs fields have the following Yukawa couplings to leptons:

$$\mathcal{L} = h_{ij}\, L_{iL}^T\, C\, i\sigma_2\, \Delta\, L_{jL} + h.c., \tag{3.7}$$

where h_{ij} are coupling constants for the Higgs-Lepton coupling, L_L is a left handed lepton doublet $L_{iL} = (\nu_{iL}, l_{iL})$, i,j are flavour indices and C is the Dirac charge conjugation operator.

The Higgs potential including the Standard Model Higgs sector $\phi = (\phi^+, \phi^0)^T$, is:

$$\begin{aligned} V &= m^2\,(\phi^\dagger\phi) + \lambda_1\,(\phi^\dagger\phi)^2 + M^2 \mathrm{Tr}(\Delta^\dagger\Delta) + \lambda_2\,[\mathrm{Tr}(\Delta^\dagger\Delta)]^2 + \lambda_3\,\mathrm{Det}(\Delta^\dagger\Delta) \\ &+ \lambda_4\,(\phi^\dagger\phi)\,\mathrm{Tr}(\Delta^\dagger\Delta) + \lambda_5\,(\phi^\dagger\,\sigma_i\,\phi)\mathrm{Tr}(\Delta^\dagger\,\sigma_i\,\Delta) + \left(\frac{1}{\sqrt{2}}\mu\left(\phi^T\,i\sigma_2\,\Delta^\dagger\,\phi\right) + h.c.\right), \end{aligned} \tag{3.8}$$

where λ_i are dimensionless quartic couplings, μ is a dimensionful trilinear coupling and M is the common triplet mass $(M^2\Delta^\dagger\Delta)$. From this potential a vacuum expectation value v_Δ for the neutral member of the triplet Δ_0 can be derived:

$$v_\Delta = \frac{\mu\, v^2}{2\, M^2} \tag{3.9}$$

The neutrinos acquire mass by Yukawa coupling to the neutral Higgs triplet member. The neutrino mass matrix elements (see eq. (3.3)) are proportional to the coupling constants h_{ij} and to the vacuum expectation value v_Δ:

$$m_{ij} = \sqrt{2}\, h_{ij}\, v_\Delta \tag{3.10}$$

The HTM states the existence of 7 Higgs bosons ($H^{++}, H^{--}, H^+, H^-, H^0, A^0, h^0$). $H^{\pm\pm}$ consists only of triplet fields, the other Higgs bosons are mixtures of doublet and triplet fields. Except for h_0 the Higgs bosons are composed mainly of triplet fields, h_0 is a Standard Model like Higgs boson and composed mainly of doublet fields. In the HTM the masses of the physical Higgs bosons are related in the following way:

$$m^2_{H^{\pm\pm}} = M^2 + 2\,\frac{\lambda_4 - \lambda_5}{g^2}\, M_W^2 \tag{3.11}$$

$$m^2_{H^{\pm}} = m^2_{H^{\pm\pm}} + 2\,\frac{\lambda_5}{g^2}\, M_W^2 \tag{3.12}$$

$$m^2_{H^0, A^0} = m^2_{H^{\pm}} + 2\,\frac{\lambda_5}{g^2}\, M_W^2 \tag{3.13}$$

The observation of a doubly charged Higgs boson would be the most striking signature of the HTM, as it decays into equally charged particles. In addition, the measurement of the leptonic decay rates of $H^{\pm\pm}$ and therefore of h_{ij} could help to determine the neutrino mass matrix. The decay rate for $H^{\pm\pm} \to l_i^\pm l_j^\pm$ is related to h_{ij} by:

$$\Gamma(H^{\pm\pm} \to l_i^\pm l_j^\pm) = S\,\frac{m_{H^{\pm\pm}}}{8\pi}\,|h_{ij}|^2, \tag{3.14}$$

where S = 1 (2) for $i = j$ ($i \neq j$).

The production and decay processes are determined by the couplings of the H^{++} boson. H^{++} couples to leptons, photons, W and Z bosons, singly charged Higgs bosons and to itself. Triplet Higgs fields do not couple to quarks. This supresses all couplings of $H^\pm$, A^0 and h^0 Higgs bosons to quarks.

Another possibility to explain non-zero neutrino masses and also the smallness of these masses are Left-Right Symmetric Models.

3.3 Left-Right Symmetric Models

Left-Right Symmetric Models [9–12] not only lead to a natural explanation of the smallness of neutrino masses but give also a better understanding of parity violation.

In these models the lepton sector is symmetrized. The right handed fermion singlets of the Standard Model and newly introduced right handed neutrinos are put together to form SU(2) doublets:

$$u_R, d_R \to \begin{pmatrix} u_R \\ d_R \end{pmatrix} \qquad \nu_R, l_R \to \begin{pmatrix} \nu_R \\ l_R \end{pmatrix} \tag{3.15}$$

According to the $SU(2)_L$ gauge fields which couple only to left handed particles a new gauge group $SU(2)_R$ is introduced. The gauge fields of $SU(2)_R$ couple only to right handed particles. The gauge group of electroweak interactions $SU(2)_L$ x $U(1)_Y$ changes into $SU(2)_L$ x $SU(2)_R$ x $U(1)_Y$. The modified Gell-Mann-Nishijima-Relation for the Left-Right Symmetric Model is:

$$Q = I_{3L} + I_{3R} + \frac{Y}{2} \tag{3.16}$$

In Left-Right Symmetric Models, in contrast to the Standard Model, Y can easily be calculated for quarks and leptons in the following way [12]:

$$Y = B - L, \tag{3.17}$$

where B is the Baryon number, $B = 1/3$ for quarks, $B = -1/3$ for anti quarks and $B = 0$ for leptons. L is the Lepton number, $L = -1$ for leptons, $L = 1$ for anti leptons and $L = 0$ for quarks.

To each left and right handed quark doublet Q_L, Q_R and lepton doublet L_L, L_R the following quantum numbers (I_L,I_R,$B - L$) can be associated [12]:

$$Q_L : \left(\frac{1}{2}, 0, \frac{1}{3}\right) \qquad Q_R : \left(0, \frac{1}{2}, \frac{1}{3}\right) \tag{3.18}$$

$$L_L : \left(\frac{1}{2}, 0, -1\right) \qquad L_R : \left(0, \frac{1}{2}, -1\right), \tag{3.19}$$

Associated to $SU(2)_R$ are three new gauge fields W_{R1}, W_{R2}, W_{R3} which couple only to right handed fermions.

The left and right handed fermions get equal masses by Yukawa coupling to a 2×2 matrix ϕ of scalar fields with the quantum numbers $(I_L, I_R, B - L) = (1/2, 1/2, 0)$ [12].

$$\phi = \begin{pmatrix} \phi_1^0 & \phi_1^+ \\ \phi_2^- & \phi_2^0 \end{pmatrix}, \tag{3.20}$$

ϕ fulfills the modified Gell-Mann-Nishijima-Relation.

The Lagrangian which describes the Yukawa coupling of fermions to ϕ is [11]:

$$\mathcal{L}_Y(\phi) = - \sum_{\psi=Q,L} \left[\bar{\psi}_{Li} \, \Gamma_{ij}^{\psi} \, \phi \, \psi_{Rj} + \bar{\psi}_{Li} \, \Xi_{ij}^{\psi} \, \tilde{\phi} \, \psi_{Rj} + h.c. \right], \tag{3.21}$$

where ψ_L and ψ_R are left and right handed wave functions. Γ_{ij}^{ψ} and Ξ_{ij}^{ψ} are coupling parameters which have yet to be determined.

As right handed neutrinos with masses equal to the Standard Model neutrino masses seem not to exist, the Left-Right Symmetry has to be a broken symmetry.

The symmetry can be spontaneously broken if the Higgs sector is enlarged. Scalar triplets with the following quantum numbers (I_L,I_R,$B - L$) are introduced [12]:

$$\Delta_L : (1, 0, 2) \quad \text{and} \quad \Delta_R : (0, 1, 2) \tag{3.22}$$

The Yukawa couplings of the triplets are given by [11]:

$$\mathcal{L}_Y(\Delta) = L_{Li}^T\, h_{Lij}\, C^{-1}\, i\,\sigma_2\, \Delta_L\, L_{Lj} + L_{Ri}^T\, h_{Rij}\, C^{-1}\, i\,\sigma_2\, \Delta_R\, L_{Rj} + h.c., \tag{3.23}$$

h_L and h_R are the coupling matrices. In the same manner as the Higgs triplet in the HTM, Δ_L and Δ_R are written in common notation as [12]:

$$\Delta_{L,R} = \begin{pmatrix} \frac{1}{\sqrt{2}}\Delta^+_{L,R} & \Delta^{++}_{L,R} \\ \Delta^0_{L,R} & -\frac{1}{\sqrt{2}}\Delta^+_{L,R} \end{pmatrix} \tag{3.24}$$

The Higgs potential involving ϕ, Δ_L and Δ_R can be constructed in such a way that the minimum of the potential corresponds to the following vacuum expectation values [12]:

$$\langle\phi\rangle_0 = \begin{pmatrix} \kappa & 0 \\ 0 & \kappa' \end{pmatrix} \qquad \langle\Delta_{L,R}\rangle = \begin{pmatrix} 0 & 0 \\ v_{L,R} & 0 \end{pmatrix} \tag{3.25}$$

The choice of v_R breaks the $SU(2)_R$ x $U(1)_{B-L}$ spontaneously to $U(1)_Y$. The non-zero vacuum expectation values of the bidoublet breaks the remaining $SU(2)_L$ x $U(1)_Y$ to $U(1)_{em}$. The following breaking scheme is obtained:

$$SU(2)_L \times SU(2)_R \times U(1)_{B-L} \times P \overset{v_R}{\rightarrow} SU(2)_L \times U(1)_Y \overset{\kappa,\kappa'}{\rightarrow} U(1)_{em} \tag{3.26}$$

P symbolically denotes the parity symmetry, which is broken by the choice of u_R.

The gauge bosons W_m and Z_m (m = 1, 2) of Left-Right Symmetric Models are composed of the Standard Model like gauge fields W_{Li}, which couple only to left handed fermions, and the newly introduced fields W_{Ri} (i=1,2,3), which couple only to right handed fermions, and the U(1) gauge field B.

The masses of the gauge bosons are given by [12]:

$$m^2_{W_1} \simeq \frac{1}{2}\, g^2\, (\kappa^2 + \kappa'^2 + 2\, v_L^2) \tag{3.27}$$

$$m^2_{W_2} \simeq \frac{1}{2}\, g^2\, (\kappa^2 + \kappa'^2 + 2\, v_R^2) \tag{3.28}$$

$$m^2_{Z_1} \simeq \frac{g^2}{2\cos^2\theta_W}\, (\kappa^2 + \kappa'^2 + 4\, v_L^2) \tag{3.29}$$

$$m^2_{Z_2} \simeq 2\, (g^2 + g'^2)\, v_R^2 \tag{3.30}$$

It is assumed that $g_L = g_R$ as is natural in Left-Right Symmetric Models. g is used instead of g_L and g_R. W_1 and Z_1 couple mostly to left handed fermions and can be identified with the Standard Model W and Z bosons. W_2 couples mostly to right handed fermions. To preserve the Standard Model relation between W_1 and Z_1, v_L has to be small ($v_L \ll max(\kappa, \kappa')$). v_R is forced to be large [$v_R \gg \kappa, \kappa'$], by experimental results from the mixing of long and short lived K mesons [12]. A large value of v_R leads to heavy W_2 bosons.

Left-Right Symmetric Models state the existence of fourteen physical Higgs bosons [12]. Four doubly charged Higgs bosons, four singly charged Higgs bosons and six neutral Higgs

bosons. The doubly charged members of the two Higgs triplet representations $\Delta_L^{\pm\pm}$ and $\Delta_R^{\pm\pm}$ remain unmixed and correspond to physical Higgs bosons. They are completly different particles and do not need to have the same mass or couplings.

The physical singly charged Higgs bosons ($\kappa' = 0$ assumed) are [10]:

$$h^{\pm} = \frac{1}{\sqrt{1+\frac{\kappa^2}{2\,v_R^2}}}\,(\phi_1^{\pm} + \frac{\kappa}{\sqrt{2}\,v_R}\,\Delta_R^{\pm}) \tag{3.31}$$

$$\delta^{\pm} = \frac{1}{\sqrt{1+\frac{2\,v_L^2}{\kappa^2}}}\,(\Delta_L^{\pm} + \frac{\sqrt{2}\,v_L}{\kappa}\,\phi_2^{\pm}) \tag{3.32}$$

κ' needs to be zero if all the following requirements should be fulfilled [10]:

- no negative masses should be generated,
- Left-Right Symmetric Models should be consistent with experiments on flavour changing neutral currents,
- Left-Right Symmetric Models should be consistent with the experimentally obtained mass ratios of Standard Model W and Z boson.

3.3.1 Neutrino Mass

In Left-Right Symmetric Models neutrinos obtain mass by two mechanisms [11]. Firstly they can gain mass by the Standard Model Higgs mechanism, where the Yukawa coupling to the bidoublet field ϕ connects left handed with right handed fermions (3.21). The neutrino mass matrix (3x3) generated by this mechanism is:

$$M_{Yuk} = \frac{1}{\sqrt{2}}(\kappa\,\Gamma_L + \kappa'^{*}\,\Xi_L) \tag{3.33}$$

Since neutrinos are chargeless leptons, they can also gain a majorana mass by the coupling of a neutrino and its hermitian conjugate neutrino to the triplet scalars $\Delta_{L,R}$, see equation (3.23).

A vector Ω_L can be defined with all 6 left handed degrees of freedom for the neutrinos:

$$\Omega_L = \begin{pmatrix} \nu_L \\ (\nu_R)^c \end{pmatrix} \qquad \nu_{\mathrm{L,R}} = \begin{pmatrix} \nu_e \\ \nu_\mu \\ \nu_\tau \end{pmatrix}_{L,R} \tag{3.34}$$

With this vector the neutrino mass term including both types of mechanism is given by:

$$\mathcal{L}_\nu^m = \frac{1}{2}\,\Omega_L^T\,C^{-1}\,M_\nu\,\Omega_L + h.c., \tag{3.35}$$

with M_ν as the whole neutrino mass matrix (6×6):

$$M_\nu = \begin{pmatrix} \sqrt{2}\,v_L\,h_L & M_{Yuk}^{*} \\ M_{Yuk}^{\dagger} & \sqrt{2}\,v_R^{*}\,h_R^{*} \end{pmatrix} \tag{3.36}$$

Unless there is an extraordinary hierarchy among the couplings, the requirements on v_L and v_R lead to $\sqrt{2}v_L h_L \ll M^*_{Yuk} \ll \sqrt{2}v_R h_R$.

After diagonalization of M_ν one gets three heavy majorana neutrinos N and three light neutrinos ν_l with approximate masses:

$$m_N \simeq \sqrt{2}\, v_R^* h_R^* \qquad m_{\nu_L} \simeq M^\dagger_{Yuk} (\sqrt{2}\, v_R^* h_R^*)^{-1} M^*_{Yuk} \tag{3.37}$$

In this way the existence of three neutrinos which are much lighter than the other leptons, could be explained by the existence of three very heavy neutrinos. This is called the "see-saw" mechanism.

3.3.2 Couplings of $\Delta^{\pm\pm}_{L,R}$

The $U(1)_{B-L}$ symmetry prevents quarks from coupling to Higgs triplet members. $\Delta^{\pm\pm}_L$ and $\Delta^{\pm\pm}_R$ couple to leptons, vector bosons and singly and doubly charged Higgs bosons, but they differ in their coupling strength.

Δ_L can be identified with the Higgs triplet of the HTM. The production and decay processes of $\Delta^{\pm\pm}_L$ and of $H^{\pm\pm}$ of the HTM are the same. The next sections will deal with the production and decay processes of $\Delta^{\pm\pm}_L$ and $\Delta^{\pm\pm}_R$.

3.4 Production Processes

1. $q\bar{q} \to \gamma/Z^*_{1,2} \to \Delta^{++}_{L,R}\Delta^{--}_{L,R}$ (Fig. 3.3):
   The doubly charged Higgs bosons are pair produced by the Drell-Yan process.
   - $q\bar{q} \to \gamma/Z^*_1 \to \Delta^{++}_L\Delta^{--}_L$ [13]:
     This is the process studied in this diploma thesis. Z_1 can be identified with the known Standard Model Higgs boson. The cross section of this process depends only on the mass of the doubly charged Higgs boson.
   - $q\bar{q} \to \gamma/Z^*_2 \to \Delta^{++}_R\Delta^{--}_R$:
     The cross section of this process depends on the unknown mass of Z_2 and on the doubly charged Higgs boson mass. The results of the study presented in this diploma thesis are for $\Delta^{\pm\pm}_L$ only. Nevertheless, the used analysis method is sensitive to this process, if four muon final states are possible for pair produced $\Delta^{\pm\pm}_R$.
2. Production by $W^\pm_{1,2}H^\pm\Delta^{\pm\pm}$ vertex (Fig. 3.4) ($H^\pm$ stands for $\delta^\pm$ and $h^\pm$):
   $\Delta^{\pm\pm}_L$ couples only to the fields W_L and $\Delta^\pm_L$ whereas $\Delta^{\pm\pm}_R$ couples only to the fields W_R and $\Delta^\pm_R$. Thus the following production processes are possible:
   - Production by $W^\pm_1\delta^\pm\Delta^{\pm\pm}_L$ vertex [8]:
     $\Delta^{\pm\pm}_L$ can be produced either by the process $q\bar{q} \to W^{\pm *}_1 \to \Delta^{\pm\pm}_L\delta^\mp$ or by fusion of $W^\pm_1$ and $\delta^\pm$.

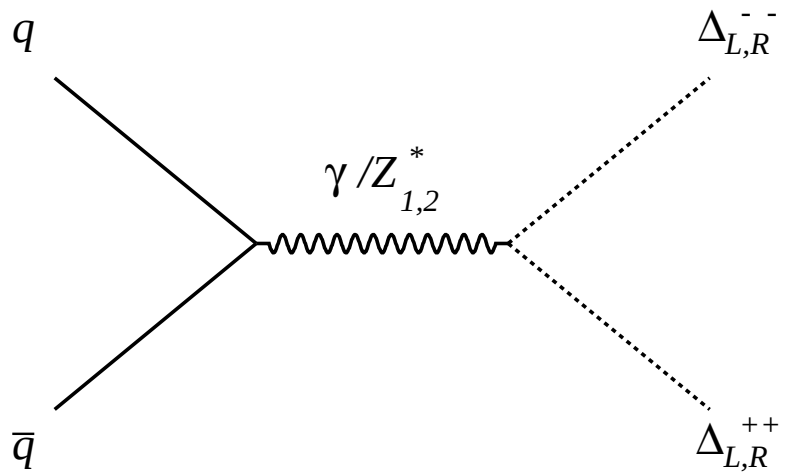

Figure 3.3: Feynman diagram for pair production of doubly charged Higgs bosons in leading order.

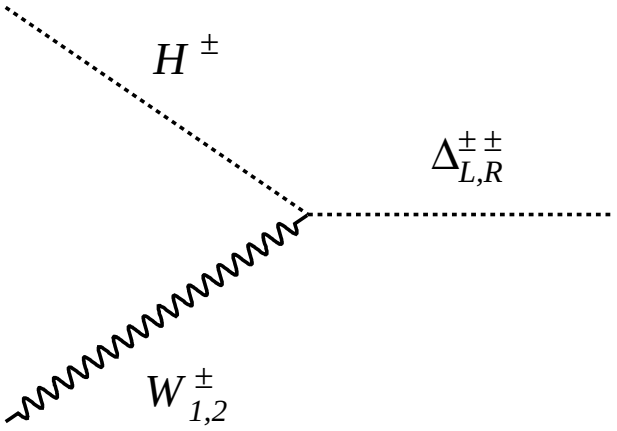

Figure 3.4: Single production of $\Delta^{\pm\pm}$ by the $W^{\pm}_{1,2}H^{\pm}\Delta^{\pm\pm}$ vertex.

The associated production of $\delta^{\mp}$ and $\Delta^{\pm\pm}$ proceeds via a gauge coupling constant and is not supressed by any small factor. For equal masses of $\delta^{\mp}$ and $\Delta^{\pm\pm}$ the probability of this process is of comparable size to the probability of the Drell-Yan process.
The production of $\Delta_L^{\pm\pm}$ by fusion of $W_1^{\pm}$ and $\delta^{\pm}$ is surpressed as only the bidoublet part $\delta^{\pm}$, which has a small weight $\frac{\sqrt{2}v_L}{\kappa}$, couples to quarks.

- Production by $W_2^{\pm}h^{\pm}\Delta_R^{\pm\pm}$ vertex (Fig. 3.5):
This process is supressed as only the $\Delta_R^{\pm}$ component of $h^{\pm}$ couples to $\Delta_R^{\pm\pm}$ and $W_{R\mu}$. $\Delta_R^{\pm}$ has only a small weight $\frac{\kappa}{\sqrt{2}v_R}$ in $h^{\pm}$.

3. Production by $W_{1,2}^{\pm}W_{1,2}^{\pm}\Delta_{L,R}^{\pm\pm}$ vertex (Fig. 3.5):
$\Delta_{L,R}^{\pm\pm}$ can be produced in this processes, either by real or by virtual W bosons,

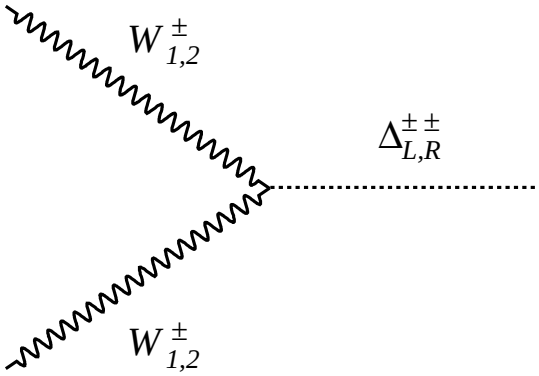

Figure 3.5: Single production of $\Delta^{\pm\pm}$ by the $W_{1,2}^{\pm}W_{1,2}^{\pm}\Delta^{\pm\pm}$ vertex.

depending on the mass of $\Delta_{L,R}^{\pm\pm}$ and $W_{1,2}^{\pm}$. The vertex of this process is given by:

$$\frac{1}{\sqrt{2}}g_{L,R}^2 v_{L,R} W_{1,2}^{\pm}W_{1,2}^{\pm}\Delta_{L,R}^{\pm\pm} \tag{3.38}$$

The coupling strength is therefore proportional to $v_{L,R}$

- Production by $W_1^{\pm}W_1^{\pm}\Delta_L^{\pm\pm}$ vertex:
Due to the small value of v_L this production process is in most cases negligible.

- Production by $W_2^{\pm}W_2^{\pm}\Delta_R^{\pm\pm}$ vertex [9]:
The larger v_R is, the stronger is the coupling, but also the heavier is W_R. For a $\Delta_R^{\pm\pm}$ mass higher than 1 TeV and a W mass lower than 1500 GeV, this cross section exceeds the production cross section of the Drell-Yan process.

4. Production by $H^{\pm}H^{\pm}\Delta_{L,R}^{\pm\pm}$ vertex (Fig. 3.6) [9]:
The coupling between two singly charged Higgs bosons and $\Delta_{L,R}^{\pm\pm}$ arises by the following quadratic term of the Higgs potential:

$$\beta_1 Tr(\phi\Delta_R\phi^{\dagger}\Delta_L^{\dagger}) + \beta_2 Tr(\tilde{\phi}\Delta_R\phi^{\dagger}\Delta_L^{\dagger}) + \beta_3 Tr(\phi\Delta_R\tilde{\phi}^{\dagger}\Delta_L^{\dagger}), \tag{3.39}$$

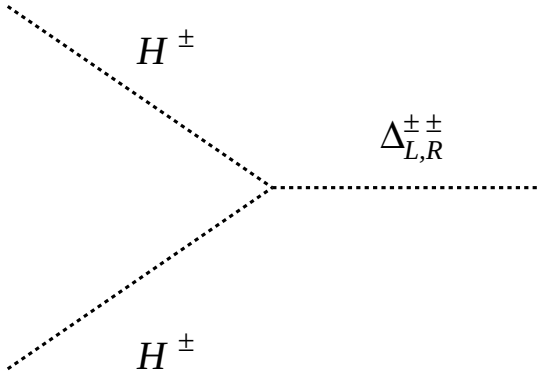

Figure 3.6: Single production of $\Delta^{\pm\pm}$ by the $H^{\pm}H^{\pm}$ vertex.

where β_i are coupling constants. This process is supressed by the small value of β_i. Large β_i would lead to a serious fine tuning problem. In the case of $\delta^{\pm}$ this coupling is also supressed by the small weight $\frac{\sqrt{2}v_L}{\kappa}$ of ϕ_2.

The production process studied in this diploma thesis is: $q\bar{q} \to \gamma/Z_1^* \to \Delta_L^{++}\Delta_L^{--}$.

3.5 Decay Processes

Assuming the Higgs boson which are mainly triplet to have masses similar to the mass of $\Delta_R^{\pm\pm}$ and $\Delta_L^{\pm\pm}$, the most probable decay processes are [9]:

- $\Delta_{L,R}^{\pm\pm} \to l_i l_j$:
  This is the kinematically most favoured decay and yields a very clear signal. The decay width of this process depends on the lepton-number violating couplings $h_{(L,R),ij}$. These couplings have to be determined by experiment. The current experimental limits on $h_{(L,R),ij}$ will be given later in this thesis. This diploma thesis arbitrarily assumes a pure muonic decay of doubly charged Higgs bosons. The results obtained with this assumption can easily be rescaled for other branching ratios. The decay width is given by [8]:

$$\Gamma(\Delta_{L,R}^{\pm\pm} \to l_{(L,R),i}^{\pm} l_{(L,R),j}^{\pm}) = S\frac{m_{\Delta_{L,R}^{\pm\pm}}}{8\pi}\left|h_{(L,R)ij}\right|^2, \tag{3.40}$$

  where S = 1(2) for i=j (i≠j) and $l_{L,R}$ are respectively left and right handed leptons. The decay width determines if doubly charged Higgs bosons decay inside the detector or are quasi-stable particles (Section 3.6.2).

- $\Delta_{L,R}^{\pm\pm} \to H^{\pm}W_{1,2}^{\pm}$ where $H^{\pm}$ stands for $\delta^{\pm}$ and $h^{\pm}$:
  - $\Delta_L^{\pm\pm} \to \delta^{\pm}W_1^{\pm}$ [8]:
    This process is driven by the SU(2) gauge coupling, and is not supressed by any small factor. Depending on $|m_{\Delta_L^{\pm\pm}} - m_{\delta^{\pm}}|$ this mode could dominate the signals

of a doubly charged Higgs boson over a substantial region of the parameter space.

  - $\Delta_R^{\pm\pm} \to h^\pm W_2$ [9]:
    As the corresponding production process $h^\pm W_2^\pm \to \Delta^{\pm\pm}$ this decay process is supressed by the small weight of $\Delta_R^\pm$ in $h^\pm$. $\Delta_R^\pm$ is the component of $h^\pm$, which couples to $\Delta_R^{\pm\pm}$. For small values of the mass of $\Delta_R^{\pm\pm}$ this decay width is considerably smaller than the width of the lepton pair channel.

- $\Delta_{L,R}^{\pm\pm} \to W_{1,2}^\pm W_{1,2}^\pm$ [9]:
  $\Delta_{L,R}$ couples to $W_{1,2}^\pm W_{1,2}^\pm$ proportional to $v_{L,R}$ (see section 3.4 Production Processes). This decay mode is supressed for the decay of $\Delta_L^{\pm\pm}$, due to the small vacuum expectation value v_L, but not for the decay of $\Delta_R^{\pm\pm}$. For $M_{W_2^\pm} \leq 0.5$ TeV, $M_{\Delta_R} \geq 2$ TeV and $h_{R,l_i l_j}$ of order one the branching ratio of the process $\Delta_R^{\pm\pm} \to W_2^\pm W_2^\pm$ exceeds the branching ratio of $\Delta_R^{\pm\pm} \to l_i l_j$.

In this diploma thesis doubly charged Higgs bosons are assumed to decay purely muonic.

3.6 Previous Experiments

The experiments which test the existence of doubly charged Higgs bosons can be sorted into two categories, indirect searches and direct searches. Direct searches try to detect the doubly charged Higgs boson directly with particle detectors like the CMS detector at the LHC or the CDF detector at the Tevatron. Indirect searches test the existence of lepton number violating processes, which might take place if a doubly charged Higgs boson is exchanged. These searches can set upper limits on the non-diagonal couplings h_{ij}.

3.6.1 Indirect Searches

Mode	upper limit on h_{ij}
$\mu \to \bar{e}ee$	$h_{\mu e}h_{ee} < 3.2 \times 10^{-11}$ GeV$^{-2} \cdot M^2_{\Delta^{\pm\pm}}$
$\mu \to e\gamma$	$h_{\mu e}h_{\mu\mu} \leq 2 \times 10^{-10}$ GeV$^{-2} \cdot M^2_{\Delta^{\pm\pm}}$
$e^+e^- \to e^+e^-$	$h^2_{ee} \leq 9.7 \times 10^{-6}$ GeV$^{-2} \cdot M^2_{\Delta^{\pm\pm}}$
$(g-2)_\mu$	$h^2_{\mu\mu} \to 2.5 \times 10^{-5}$ GeV$^{-2} \cdot M^2_{\Delta^{\pm\pm}}$

Table 3.1: The various modes which indirectly test the existence of $\Delta^{\pm\pm}$ and the corresponding upper limits on h_{ij} [9]

Table 3.1 shows recent limits on h_{ij}, obtained by studying different processes which would be affected by the existence of doubly charged Higgs bosons. The limit on $h^2_{\mu\mu}$, which is shown in the last row of the table, is obtained by measuring $(g-2)_\mu$, the anomalous magnetic moment of the muon. The magnetic moment strongly depends on possible new physics like doubly charged Higgs bosons which couple to the muon. The limits in Table 3.1 depend on the mass of $\Delta_R^{\pm\pm}$ and $\Delta_L^{\pm\pm}$. From the condition of vacuum stability, upper

limits can be derived which do not depend on the doubly charged Higgs boson mass [9]: $h_{ee}, h_{\mu\mu} \leq 1.2$.

3.6.2 Direct Searches

Direct searches for the existence of doubly charged Higgs bosons have been done at experiments at e^+e^- colliders like LEP [14] and at the proton anti-proton collider Tevatron.

The currently strongest limits have been set by the CDF collaboration at Tevatron [15]. The region $10^{-5} < h_{ij} < 0.5$ has been probed. This coupling region corresponds to narrow resonances which decay promptly ($c\tau < 10\mu$m, where τ is the lifetime of the doubly charged Higgs boson). Assuming exclusive same sign lepton decays, lower limits of the $\Delta_L^{\pm\pm}$ mass have been set. The limits are 133 GeV, 136 GeV and 115 GeV for the decay channels ee, $\mu\mu$ and $e\mu$, respectively. On the mass of $\Delta_R^{\pm\pm}$ in the $\mu\mu$ channel a lower limit of 113 GeV could be set. All mass limits are set at 95% confidencel level.

CDF has also searched for doubly charged Higgs bosons which do not decay inside the tracker $h_{ij} < 10^{-5}$ [16]. A lower mass limit of 134 GeV could be set on quasi-stable doubly charged Higgs boson production.

3.7 Summary of the Chosen Parameters

The doubly charged Higgs boson studied in this diploma thesis:

- is a member of the Higgs triplet Δ_L. Therefore it does not couple to right handed particles and to quarks.
- is pair produced by the Drell-Yan process.
- is assumed to couple to muons with a branching ratio of 100%.
- is assumed to have the following coupling constant to muons: $h_{\mu\mu} = 0.1$.

Chapter 4

LHC and the CMS Detector

This diploma thesis studies the possibility of finding or excluding doubly charged Higgs bosons with the CMS detector. The future Compact Muon Solenoid (CMS) detector is one of the four detectors at the Large Hadron Collider (LHC). LHC is situated at todays largest particle physics laboratory, Conseil Europeen pour la Reserche Nucleaire (CERN) on the border between France and Switzerland.

CERN was founded in 1954 as the European counterpart to the dominating American particle physic research centers. In 1954, 12 European states initially signed the CERN convention, today 20 states are members of CERN. Several important inventions and discoveries, which are now regarded as milestones towards the understanding of particle physics, have taken place at CERN. The invention of multiwire proportional chambers and drift chambers by Georges Charpark in 1968, the discovery of neutral currents in 1973 and the discovery of W and Z bosons in 1983 are just some examples.

CERN has hosted several large particle accelerators over the time, first the 28 GeV Proton Synchrotron (PS), then the Super Proton Synchrotron (SPS), then the e^+e^- collider LEP (Large Electron-Positron collider), and currently the LHC which is nearly finished. From 2007 onwards LHC will be the most powerful particle accelerator in the world. It will collide protons and heavy ions with energies unreached till now.

4.1 Physics at Proton - Proton Colliders

The task of particle colliders, like the LHC, is to collide as many particles as possible with energies high enough to create new particles. The cross section σ of a physics process gives a measure for the probability of this process. The event rate $\frac{dN}{dt}$ of a certain process is proportional to its cross section, the factor of proportionality is the luminosity $\mathcal{L}$.

$$\frac{dN}{dt} = \mathcal{L} \cdot \sigma \tag{4.1}$$

To provide particles with enough energy for the collisions, they get accelerated in the electrical fields of several cavities. One advantage of ring accelerators, like the LHC, is that particles can get accelerated many times by the same cavity.

The luminosity for the collision of two bunches containing n_1 and n_2 particles, depends on the frequency f with which these particles circulate inside the ring:

$$\mathcal{L} = f\frac{n_1 n_2}{4\pi\sigma_x\sigma_y}, \tag{4.2}$$

where a gaussian beam distribution has been assumed. σ_x and σ_y are the gaussian transverse beam profiles in horizontal (x) and vertical (y) direction.

One advantage of the proton-proton collider LHC is the negligible energy loss ΔE by synchtrotron radiation. This is due to the large radius r of the ring and the relativly high proton mass m. The relation between the energy loss of a particle per orbit, the radius of the collider and the particle mass is:

$$\Delta E = 6.0 \cdot 10^{-21}\,\mathrm{GeV} \cdot \left(\frac{E}{m}\right)^4 /r/km \tag{4.3}$$

The disadvantage of proton-proton colliders is, that they collide non-elementary particles and only direct inelastic collisions of the partons lead to "interesting" processes, where heavy particles are generated. Elastic collisions lead to a pollution of the detector.
The parton energy E_{parton} is only a fraction x of the proton energy E_{proton}:

$$x = \frac{E_{parton}}{E_{proton}} \tag{4.4}$$

In an inelastic collision the centre of mass energy of colliding partons s' can be calculated as:

$$\sqrt{s'} = \sqrt{x_a\, x_b s}, \tag{4.5}$$

where x_a and x_b are the energy fractions carried by the interacting partons. The cross section σ for a special ("interesting") process at proton-proton colliders depends on the density f_i of the partons inside the proton.

$$\sigma = \int dx_1 \int dx_2\, f_1(x_1, Q^2)\, f_2(x_2, Q^2)\, \hat{\sigma} \tag{4.6}$$

$\hat{\sigma}$ can be calculated for the different processes and is the so called partonic cross section. The function $f_i(x_i, Q^2)$ is called parton density function (pdf). The parton density function can be regarded as the probability that parton i takes part in a hard scattering process with the total momentum transfer Q^2 and carries the momentum fraction x_i. The parton density functions used at the LHC are determined amongst others by experiments at the hadron-electron collider HERA [17]. The knowledge of this functions is crucial for the understanding of physics at the LHC. The partonic density functions for each of the partons of the proton are shown in Figure 4.1. The protons consists of three valence quarks u, u and d, gluons and several pairs of light quarks and corresponding anti-quarks.

Due to the high luminosity and centre of mass energy which are expected at the LHC, a wide range of processes with different cross sections become observable. Figure 4.2 shows

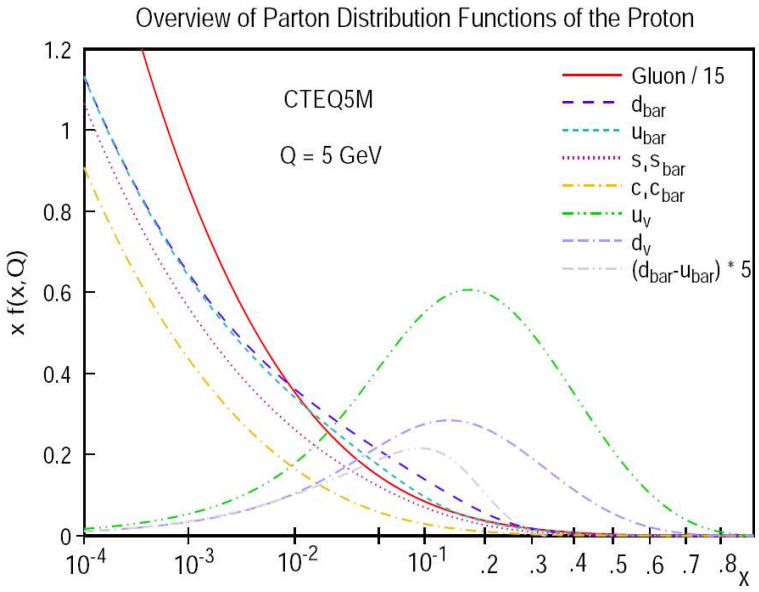

Figure 4.1: Parametrization of parton distribution functions inside the proton [18].

the cross sections and the event rates, at a luminosity of $\mathcal{L} = 10^{34}$ cm^{-2} s^{-1}, of various processes in dependency of the centre of mass energy[1]. The centre of mass energy at the LHC $\sqrt{s} = 14$ TeV is marked in this figure. The total cross section is dominated by the cross section of b quark pair production (Chapter 9). Special selection requirements have to be used to filter rare events, like the one studied in this diploma thesis, out of the total number of produced events.

4.2 The LHC Design

The LHC will be a ring accelerator, buried 50 m to 175 m below surface, with a circumference of 27 km. Two beams of protons or heavy ions counter rotate in continuous vacuum inside the LHC. The two beams circle in different ring-systems which have separate magnet dipole and quadrupole fields to bend and shape the beams. 1 232 dipole magnets with an operating magnetic field of 8.4 T are used in the LHC. To reach this magnetic field, the magnets are cooled with superfluid helium to a temperature of 1.9 K. Proton-proton collisions will take place at certain interaction points with a collision energy of 14 TeV. To accelerate the protons or heavy ions up to this energy, several acceleration steps are needed [20]:

4.2.1 Acceleration Chain

Figure 4.3 shows the whole acceleration chain and the different velocities reached at certain points of the chain.

[1] LHC is expected to reach the luminosity $\mathcal{L} = 10^{34}$ cm^{-2} s^{-1} after the year 2008.

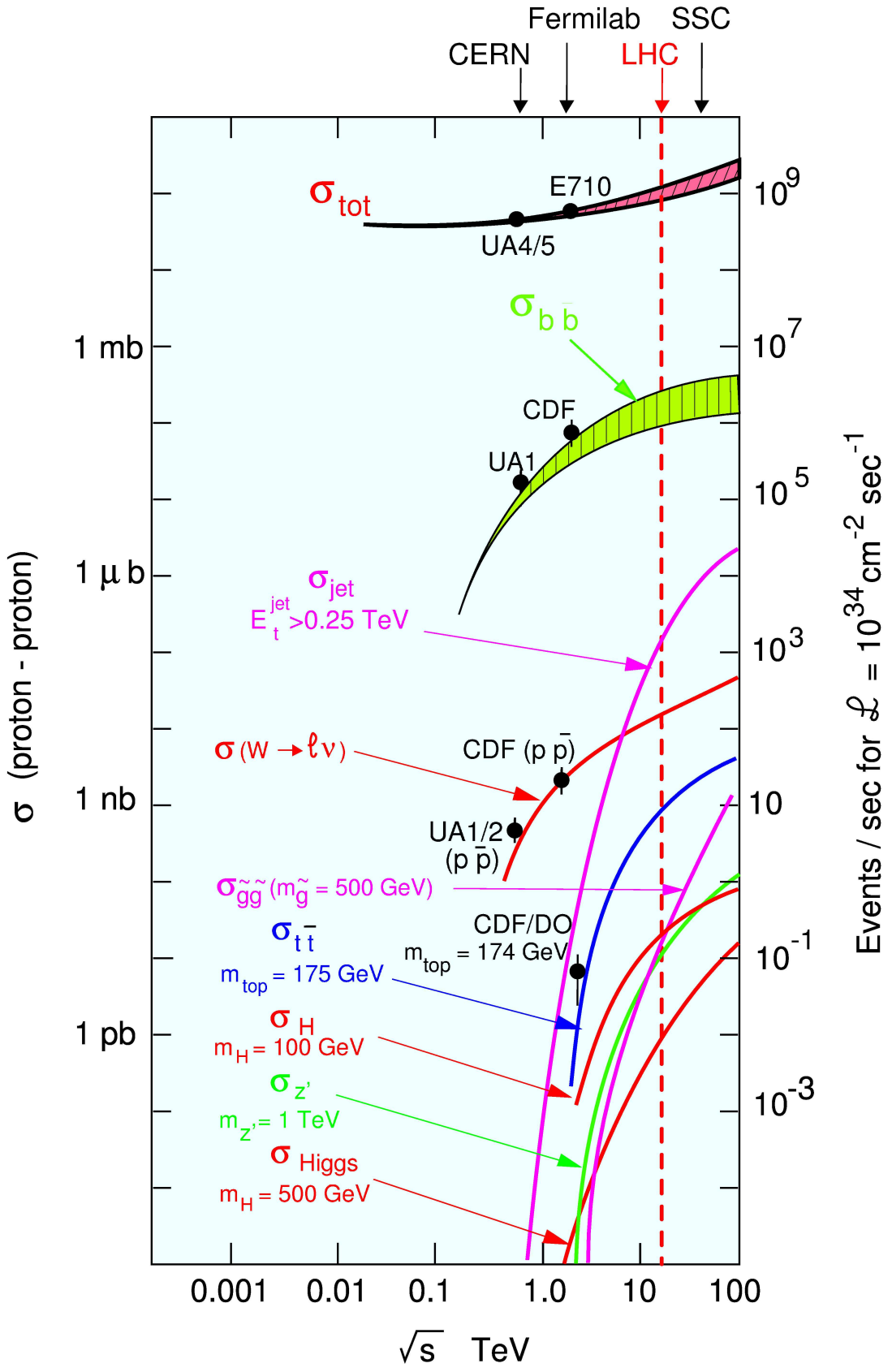

Figure 4.2: The cross sections and event rates of different processes in dependency of the centre of mass energy at proton-proton colliders [19].

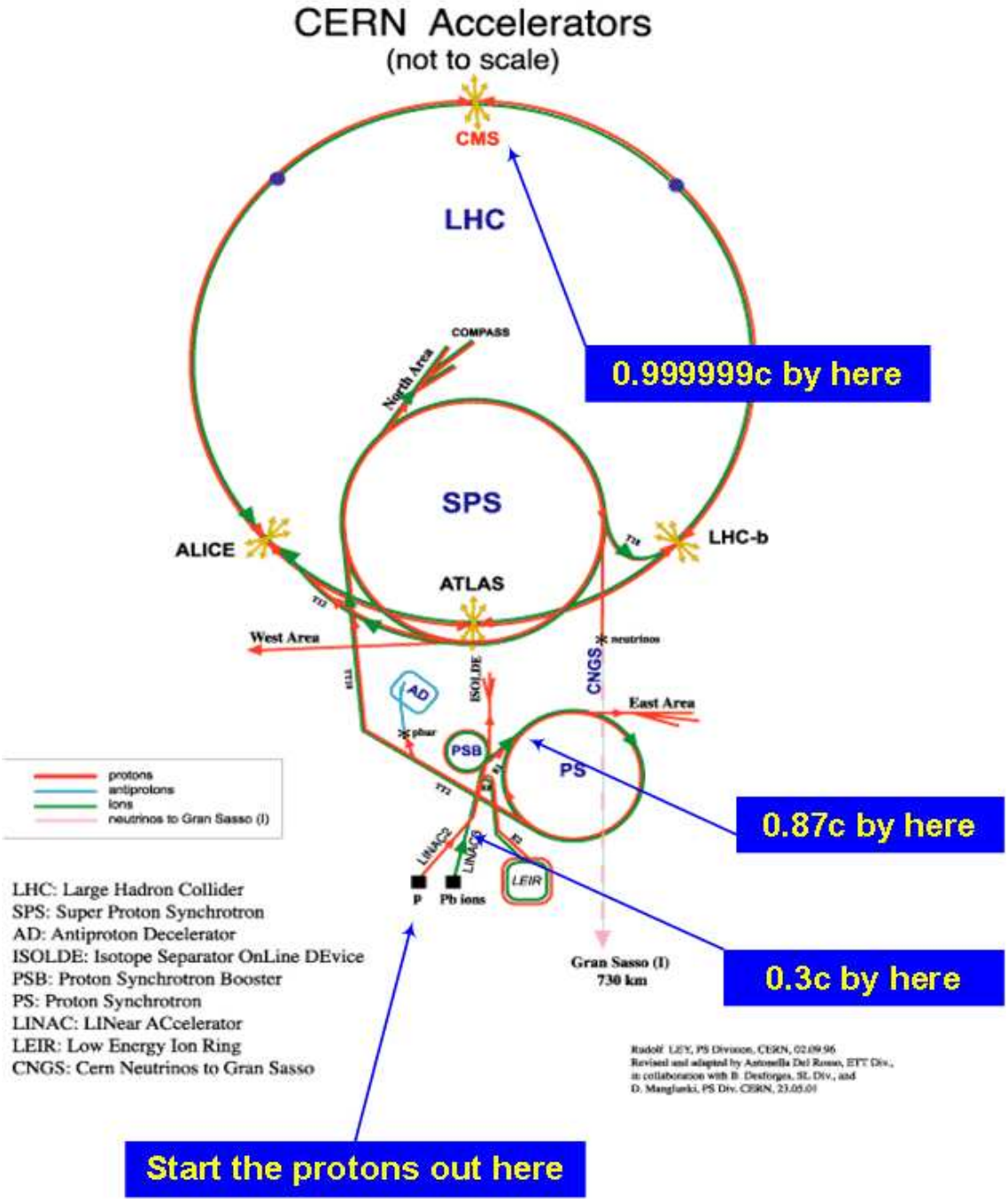

Figure 4.3: The whole CERN acceleration chain [20].

- Linac 2
  The upgraded linear accelerator Linac 2 provides protons with an energy of 50 MeV and an intensity of 180 mA. These protons are pulsed in 20 μs and led to the Proton Synchrotron (PS)

- PS
  PS is a synchotron accelerator which accelerates the protons to an energy of 26 GeV. The protons are grouped into bunches of the final spacing of 25 ns. These bunches are filled into the Super Proton Synchotron (SPS). One fill of the SPS requires three or four cycles of the PS, where one cycle takes 3.6 s.

- SPS
  In the SPS the proton bunches are accelerated to an energy of 450 GeV and extracted to one of the two rings of the LHC, this takes about 21.6 s. This operation has to be repeated 24 times for a full injection of both rings of the LHC.

- LHC
  The LHC is filled in one injection with 2 808 proton bunches. Each bunch contains $1.1 \cdot 10^{11}$ particles. The bunches are accelerated within 20 minutes from 450 GeV to 7 TeV. They meet at the four interaction points. Each 25 ns proton bunches will collide at these points.

4.2.2 Time Schedule for the Start of the LHC [1]

- 2007
  The LHC will operate only for a few weeks to test the collider and the experiments, 43 bunches should collide in this time scale. The luminosity for this start up is $\mathcal{L} = 10^{32}\text{cm}^{-2}\text{s}^{-1}$. This would give an average of 3 inelastic collisions per bunch crossing. If data will be taken, an integrated luminosity of 10 pb^{-1} could be collected.

- 2008
  The LHC should operate at a luminosity of $\mathcal{L} \simeq 2 \cdot 10^{33}\text{cm}^{-2}\text{s}^{-1}$. The bunch spacing should be 75 ns at the beginning and 25 ns later on.

- after 2008
  The design parameters $\mathcal{L} = 10^{34}\text{cm}^{-2}\text{s}^{-1}$ and a bunch spacing 25 ns should be reached.

The integrated luminosities should be 1 fb^{-1} during the intial operation, 10 - 30 fb^{-1} in the so called low luminosity phase with $\mathcal{L} \simeq 2 \cdot 10^{33}\text{cm}^{-2}\text{s}^{-1}$ and 100 - 300 fb^{-1} over several years of operation at the so called high luminosity phase $\mathcal{L} = 10^{34}\text{cm}^{-2}\text{s}^{-1}$.

4.3 The CMS Detector

The CMS detector (Fig. 4.4) is a so called multi-purpose detector. It should basically be able to identify all particles generated in the collisions, and to determine their main proper-

ties. The name of the detector, Compact Muon Solenoid, phrases its basic properties: the compact design, the emphasis placed on a highly efficient muon detection and measurement and the fact that the detector is based around a single superconducting solenoid.

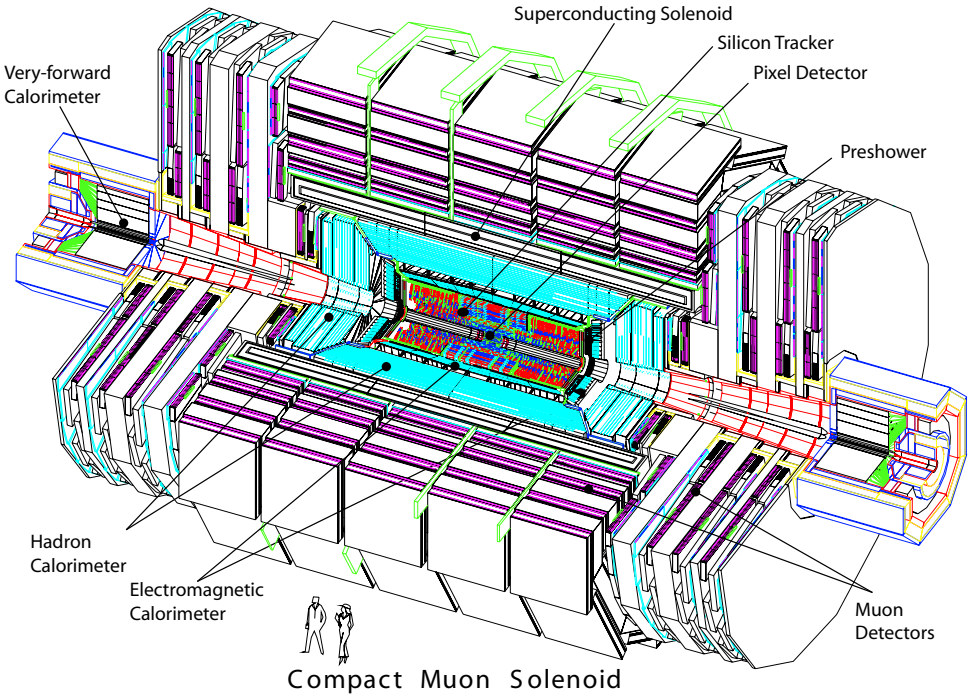

Figure 4.4: The CMS detector [1].

The compactness of the CMS design can be estimated by comparing it to the other multi-purpose detector at the LHC, ATLAS. The CMS detector weights 12 500 tonnes, which is double the weigth of ATLAS, but with its length of 21 m and its diameter of 15 m it is eight times smaller than ATLAS.
The highly efficient muon system of CMS is crucial for detecting new physics, as muons provide clean signatures for a wide range of physics. The muon system should identify muons, measure their momentum precisely and provide fast information to decide if an event is "interesting" or not. The muon system is described in detail in chapter 4.3.4.
To measure the charge and the momentum of charged particles, particle detectors need a magnetic field, which bends the tracks of charged particles according to their momen-

tum. The magnet used in the CMS detector is a superconducting solenoid magnet with a magnetic field of 4 Tesla. Its length is 13 m and its inner diameter is 5.9 m. To keep the magnet superconducting it is cooled with liquid helium. The magnet will store an energy of 2.7 GJ. A map of the expected magnetic field of the detector is shown in figure 4.5. It can be seen, that the magnetic field in the barrel is quite homogenous, in contrast to the inhomogenous field in the endcaps. The magnetic induction should be about 4 Tesla in the coil and in the innermost section of the endcap yoke, and about 1.7 Tesla in the barrel part of the return yoke and in the outermost disk of the endcap yoke. See [1] for further information about the superconduction solenoid and the magnetic field expected at CMS.

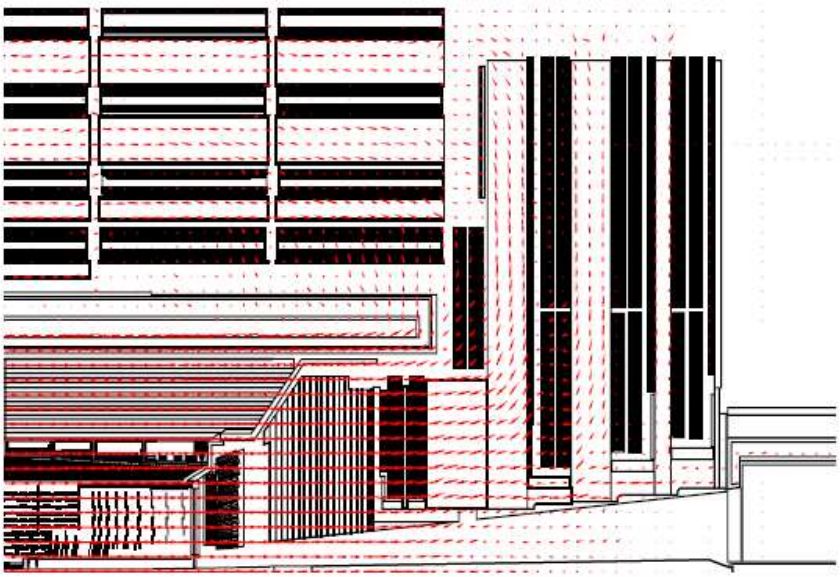

Figure 4.5: CMS magnetic field map [19].

Figure 4.6 shows a vertical slice through the detector, where all important parts of the detector can be seen: Central Inner Tracker, Electromagnetic Calorimeter, Hadronic Calorimeter, Solenoid, the iron return yoke plates of the maget and the Muon System.

The detector is built in an onion-like structure surrounding the interaction point (Fig. 4.4). One of the reasons for this design is the intention to discriminate between particles with different energy losses and different reach in material. Electrons and photons shower mainly in the Electromagnetic Calorimeter, where their energy can be measured precisely. Hadrons which interact via the strong interaction deposit most of their energy in the Hadronic Calorimeter. Muons should be the only charged particles which travel through all iron return yoke plates and reach the Muon System. The different detector parts are described in the following sections. For more detailed information about the detector see [1].

4.3.1 The Inner Tracking System

The Inner Tracker System is the innermost part of the detector and is built close to the beam pipe. The Inner Tracker should measure the multiplicity of particles generated at the

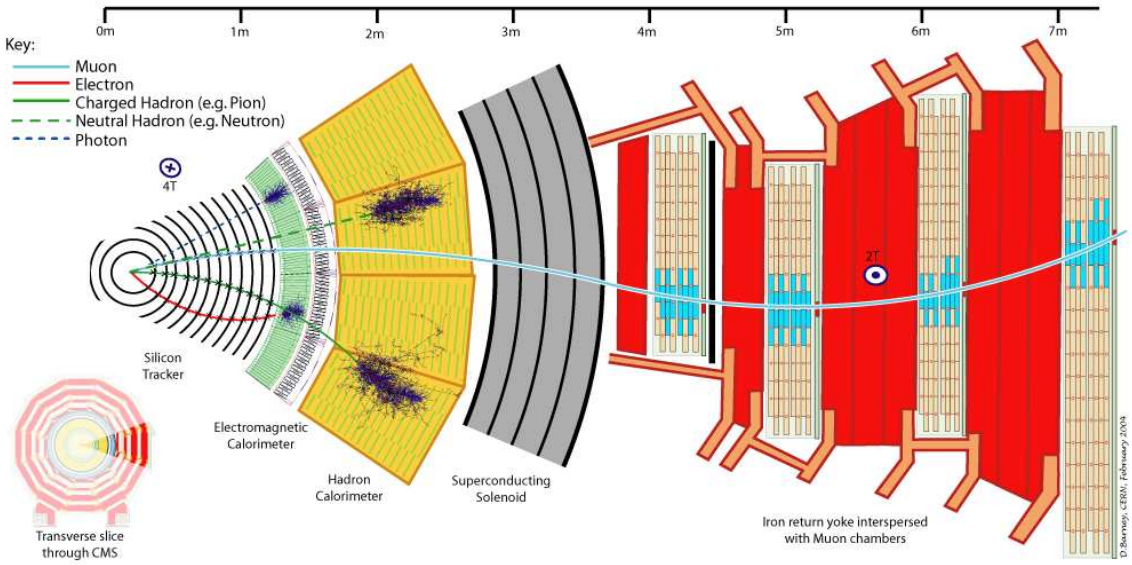

Figure 4.6: Slice through the CMS detector showing particles incident on the different detector parts [21].

interaction point with high momentum resolution. It should be able to reconstruct muons, isolated electrons and hadrons tracks with an efficiency of better than 98%. It should also have a high spatial resolution to identify tracks coming from detached vertices and be robust enough to survive in this region of strong radiation. Furthermore it should be built as transparent (small number of radiation lengths) as possible to prevent e.g. electrons from radiating before they reach the electromagnetic calorimeter.

To fulfill all these tasks the inner tracking system is divided into two parts:

- The pixel detectors, closest to the interaction vertex (at a radius $r > 4$ cm). This is the region of high particle fluxes, i.e. $\approx 10^7/s$ at $r \approx 10$ cm.
- The silicon microstrip detectors at the region of intermediate particle fluxes ($r > 20$ cm).

Both detectors are semi-conductor detectors. The readout of all Tracker sub-detectors is analog using the information of the charge deposited on each strip or pixel. The charge-sharing among neighbouring pixels is due to the 4 T magnetic field. Analog readout improves the resolution compared to a digital readout, where the resolution of the detector is determined by the pixel or strip size.

The momentum resolution of the tracking system together with the momentum resolution of the muon system is shown in Figure 4.13.

Further information about the CMS tracker can be found in [22].

The Silicon Pixel Detector

The Pixel Detector consists of three barrel layers (length = 53 cm) and two forward and two endcap disks (inner radius 6 cm outer radius 15 cm) on each side. The disks are placed at $|z| = 34.5$ cm and 46.5 cm. The total area of the pixel detector is $\approx 1\text{m}^2$ and comprises 66 million pixels. The pixel size is 100×150 μm.

The Silicon Strip Detector

Figure 4.7 shows the design of the Silicon Strip detector. It can be divided into four parts:

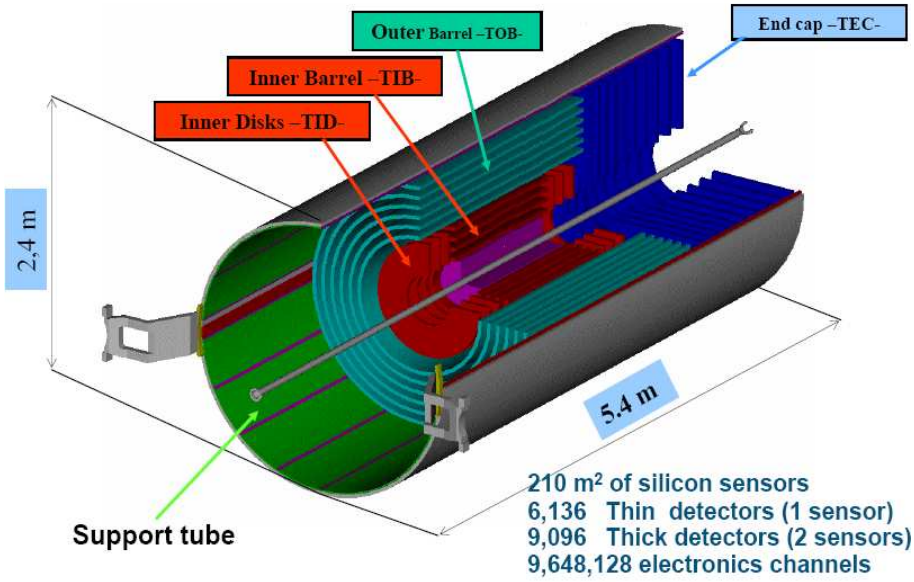

Figure 4.7: The CMS Silicon Strip detector, consisting of TID, TIB, TOB, TEC. The Silicon Pixel detector is indicated as pink tube in the center of the Silicon Strip detector [22].

Inner Barrel (TIB), Outer Barrel (TOB), Inner Disks (TID) and End Cap (TEC). Together cover these parts a cylindrical volume with a length of 5.4 m, an inner radius of 0.2 m and an outer radius of 1.2 m.

The division between inner barrel and outer barrel is due to the particle flux environments depending on the distance to the beam pipe. The Inner Barrel is close to the beam, its granularity has to be high to separate between neighbouring tracks. The single point resolution of the Inner Barrel is $23 - 34$ μm in the $r - \phi$ directions and 230 μm in z. To achieve this resolution the distances between the single strips are very small (strip pitch 80 μm to 120 μm) and the thickness of the sensors is 320 μm. For the larger pitches, the analog readout does not significantly improve the resolution, as most of the charge is deposited on a single strip. The occupancy in the inner barrel is $\approx 2 - 3\%$/LHC crossing.

The Outer Barrel works in an environment with lower particle fluxes where the single point resolution can be reduced to keep under controll the overall cost of the tracker. Wider pitches between the strips (120 μm to 180 μm), longer strips and thicker silicon

sensors (500 μm) are used in the outer barrel. The single point resolution of the Outer Barrel is 35 μm in the $r-\phi$ directions and 530 μm in z. The occupancy in the outer barrel is $\approx 1\%$/LHC crossing.

The full silicon strip detector covers the region $|\eta| < 2.5$. The operating temperature will be around $-20°$ C to ensure that the silicon survives the high radiation environment.

4.3.2 The Electromagnetic Calorimeter

In the Electromagnetic Calorimeter (ECAL) scintillating crystals absorb the radiation deposited by electromagnetically interacting particles, photons or parts of the electromagnetic fraction of jets. Shortly after this absorption the crystals emit light of a characteristic spectrum. To measure the energy of electromagnetically charged particles as precisely as possible the particles have to be stopped inside the Electromagnetic Calorimeter. To keep the Electromagnetic Calorimeter small the scintillating crystals in the CMS detector consist of lead tungstate $PbWO_4$, which has a short radiation length of ($X_0 = 0.89$ cm). The scintillating crystals are fast (80% of the light is emitted within 25 ns) and radiation hard (up to 10 Mrad) which is important in the high radiation environment inside the CMS detector.

The photodetectors which detect the light emitted by the crystals are silicon avalanche photodiodes (ADPs) in the barrel and vacuum phototriodes (VPTs) in the endcap. These photodiodes and phototriodes have a high intrinsic gain which amplifies the low light yield (30γ/MeV) of the scintillators.

Both the crystal light yield and the photodetector gains have a strong temperature dependence. Therefore the temperature should be kept stable within 0.1°C.

The electromagnetic calorimter is divided into a barrel section (EB) and endcaps (EE) (Fig. 4.8). The barrel has a length of $\sim$ 6 m, an inner radius of 1.3 m and an outer radius of 1.8 m. It covers $0 < |\eta| < 1.479$. The crystals in the barrel have a size of $22 \times 22 \times 230$ mm^3. The front face of the crystals points towards the interaction region. The endcaps are placed at $|z| = 314$ cm.

A preshower device is placed in front of each endcap. It consists of a lead absorber, which covers a range from $1.65 < |\eta| < 2.61$, and 2 planes of silicon strip detectors for readout with a pitch of 1.9 mm. This device should improve neutral pion and photon separation. The lead absorber initiates photon showers.

Electromagnetic Calorimeter Performance

The energy resolution of the Electromagnetic Calorimeter has been tested in a test beam. The resolution is parametrized as a function of energy [1]:

$$\left(\frac{\sigma(E)}{E}\right)^2 = \left(\frac{S}{\sqrt{E}}\right)^2 + \left(\frac{N}{E}\right)^2 + C^2, \tag{4.7}$$

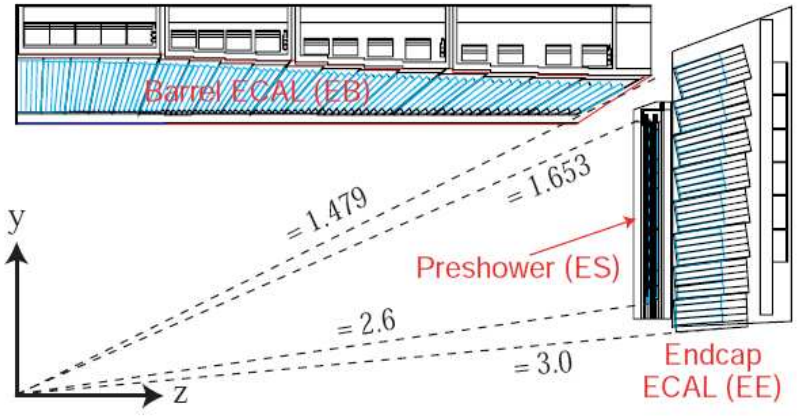

Figure 4.8: Transverse section through the ECAL, showing the geometrical configuration [1].

where S is the stochastic term, N the noise and C a constant term. The measured values are: $S = (3.63 \pm 0.1\%)\ \sqrt{\text{MeV}}$, $N = 124$ MeV and $C = 0.26 \pm 0.04\%$.

4.3.3 The Hadron Calorimeter

The main task of the hadron calorimeter is to stop strongly interacting particles and to measure their energy precisely. If the transverse component of the energy carried away by particles in one event can be measured precisely, the so called missing transverse energy (E_T^{miss}) can be calculated. In this way non-interacting particles like neutrinos can be seen indirectly.
Therefore the hadronic calorimeter is built of absorber material with short interaction lengths and provides an almost full angular coverage of $|\eta| < 5$.

The Calorimeter is divided into four parts. Three parts are inside the magnet coil, the barrel hadronic calorimter (HB), which covers the region $|\eta| < 1.3$, two endcap hadron calorimeters (HE),which cover $|\eta| < 3$ and for even more forward regions the forward calorimeter (HF). The outer calorimeter (HO) is positioned outside the magnet to improve the shower containment. The hadronic calorimeter provides a full angular coverage of $|\eta| < 5$.

Barrel Hadronic Calorimeter and Endcap Hadronic Calorimeter

The absorber material used inside the barrel and the endcap is brass, which has a reasonably short interaction length. Plastic scintillator tiles are the active medium which detects energy deposited inside the barrel and the endcap. The readout is done by wave-length shifting plastic fibres.

The Barrel Calorimeter is diveded into two half barrels, which are structured into eighteen 20° wedges in ϕ [23]. Each wedge consists of alternating 17 layers of 50 mm thick brass plates and 4 mm thick readout scintillators.

The endcap hadronic calorimeters consists of eighteen 20° modules. These modules are made of 19 layers of brass and scintillator.

Forward Hadronic Calorimeters

The forward hadronic calorimeter should improve the measurment of E_T^{miss} and enable the identification and reconstruction of very forward jets. The forward calorimeters are located 11.2 m from the interaction point and have a length of 1.65 m and a radius of 1.4 m. Each forward calorimeter is constructed of 18 wedges. They wedges are made of steel absorbers and embedded radiation hard quartz fibers running parallel to the beam axis. This fibers provide a fast collection of so called Cherenkov light.

Outer Hadronic Calorimeter

The outer calorimeter should absorb the strong interacting particles which reaches the region beyond the magnet. This calorimeter increases the effective thickness of the hadron calorimeter to over 10 interaction lengths. The outer calorimeter consists of two layers of scintillators on either side of an iron absorber. The outer calorimeter is located outside the solenoid but inside the barrel muon system. It is divided into five rings.

Hadronic Calorimeter Performance

The resolution of the missing transverse energy $\sigma(E_T^{miss})$ in QCD dijet events with pile-up is given by [1]:

$$\sigma(E_T^{miss}) \approx 1.0\sqrt{\sum E_T}, \tag{4.8}$$

as a function of the transverse energy E_T. Energy clustering corrections are not made. The average missing transverse energy is:

$$\langle E_T^{miss} \rangle \approx 1.25\sqrt{\sum E_T}. \tag{4.9}$$

4.3.4 The Muon System

Three types of gaseous detectors are used in the muon system (Fig. 4.9), Drift Tubes (DT), Cathode Strip Chambers (CSC) and Resistive Plate Chambers (RPC). These gaseous detectors are chosen accordingly for the different environments in barrel and endcap. Drift Tubes (DT) are the detectors of choice for the large area of the barrel ($|\eta| < 1.2$) with its relatively low expected rate and low residual magenetic field (less than 1 T). They are designed for providing a very good spatial resolution in this environment. CSCs provide a relativly precise spatial and time resolution even in the high magnetic field and high particle rate environment of the endcap region ($|\eta| < 2.4$). DTs and CSCs are supplemented in barrel and endcap by Resistive Plate Chambers (RPC), which have a less good spatial resolution, but a much better time resolution and are very fast. See [24] for further information about the muon system.

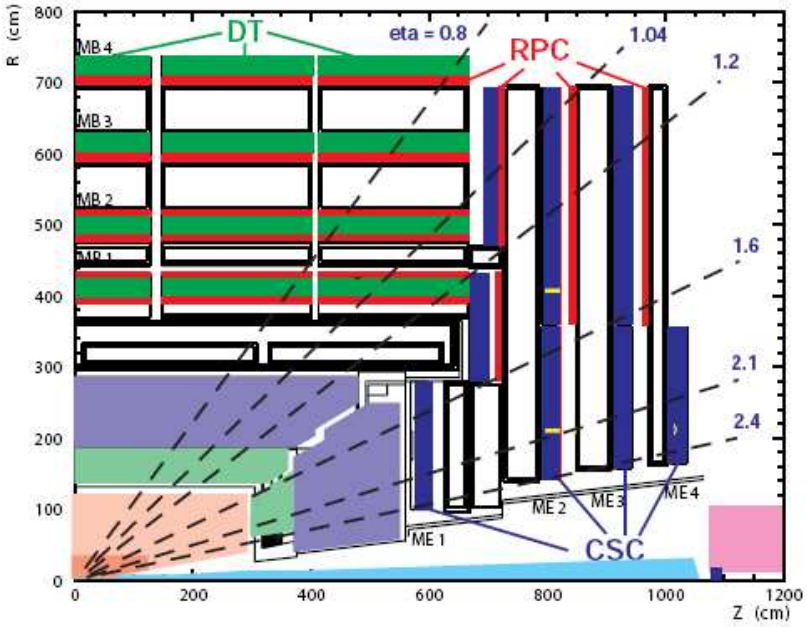

Figure 4.9: Longitudinal cut of the CMS Muon System [1].

Drift Tube Chambers

The Barrel Detector (Fig. 4.10) is divided into 5 wheels which are themselves divided into four concentric cylinders with growing diameter around the beam pipe and 12 wedges with each covering a 30° azimuthal angle.
The naming conventions of the four cylinders, called stations, can be seen in figure 4.9. The chambers in station MB 1 - 3 consist out of three so called superlayers, chambers in MB4 out of two. Between two superlayers which measure the ϕ coordinate is one superlayer which measures the z coordinate, called θ superlayer, and is therefore rotated by 90°. The bending of the muon track in the $r - \phi$ plane is directly related to the muon momentum. To improve the precision with which the track direction in the $r - \phi$ bending plane can be measured, a honeycomb structure has been inserted between one ϕ superlayer and the other two superlayers. This gives a lever arm of about 28 cm. Each superlayer is divided into four layers of Drift Tube cells.
One drift tube cell can be seen in figure 4.11. Drift Tubes are a type of gaseous detectors called drift chambers. Drift chambers provide a high spatial resolution by measuring the time span between the transition of the chamber by a charged particle and the detection of the signal by the drift chamber. This time span is called drift time. The cell layers are shifted by half a cell width in respect to each other, in order to resolve if a track has passed left or right of the anode wire.
A hit can be measured by a Drift Tube cell with an efficiency larger than 99%. The resolution of each chamber in ϕ should be better than 100 μm in position and 1 mrad in direction.

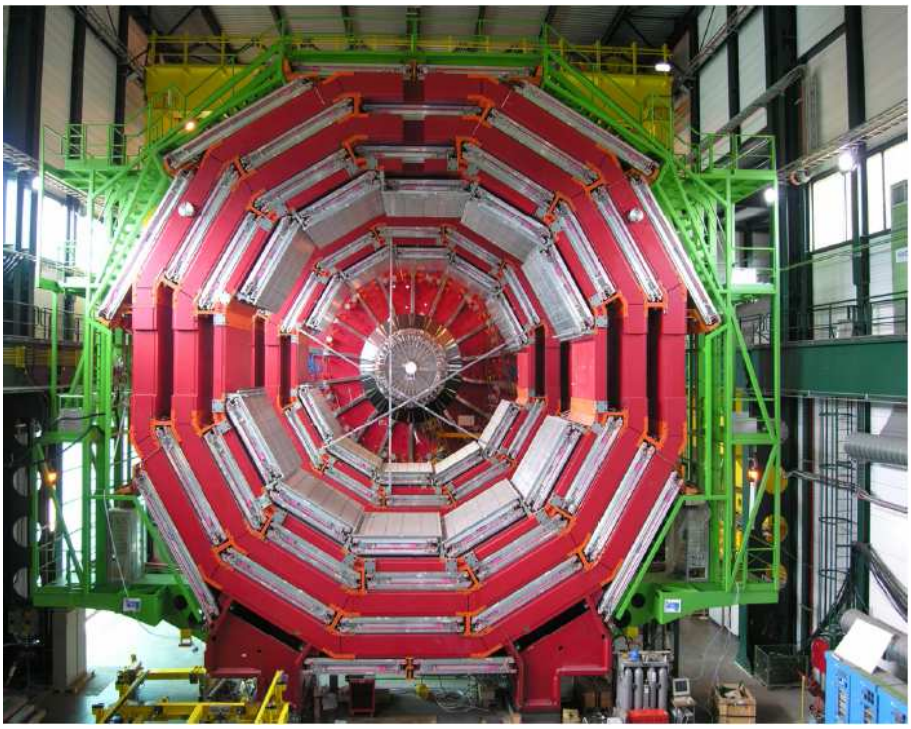

Figure 4.10: Installation of DT chambers into the Barrel Detector [1].

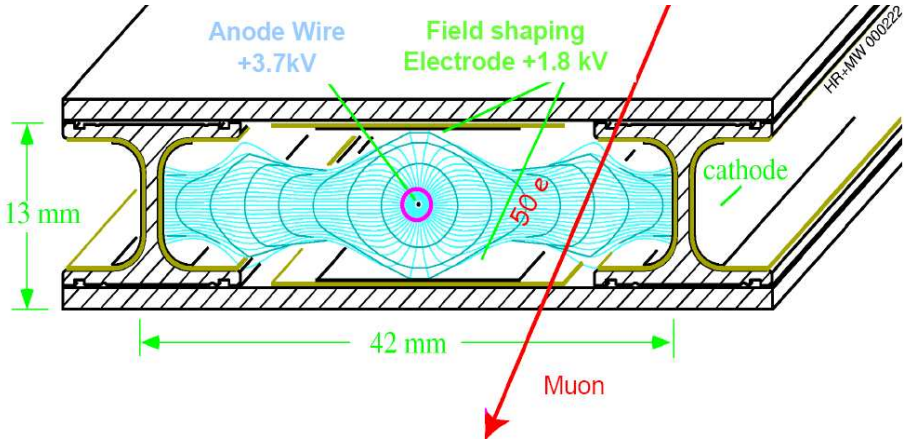

Figure 4.11: Cross section of a CMS drift cell with isochrones and drift lines of electrones [25].

Cathode Strip chamber

The CSC system is fixed onto the endcap iron return yokes and consists of four discs per endcap (ME1 to ME4 from inside out). The innermost disc ME1 is divided into two concentric rings, ME2 - ME3 are divided into three rings. The rings themselves are segmented into trapezoidal chambers.
A single chamber is composed out of six layers of Cathode Strip Chambers. Cathode Strip Chambers are multi-wire proportional chambers with segmented cathode readout. Each anode wire of a multi-wire proportional chamber acts as single independent detector. The cathodes are segmented into strips, which are aligned perpendicular to the wires. Cathode Strip chambers provide a precise space and time information in the high magnetic field and high particle rate in the endcaps.
The spatial resolution provided by the strips is $\sim$ 200 μm. The angular resolution is $\sim$ 10 mrad.

Resistive Plate Chambers

In the barrel region the first two DT stations are sandwiched by RPCs and to each of the two outer stations one RPC is attached (Fig. 4.9). For the initial low-luminosity run, the RPC system is limited to $|\eta| < 1.6$. RPCs are fast triggers which can identify candidate muon tracks and assign the right bunch crossing with high efficiency.

One RPC chamber consists of a pair of parallel bakelite plates separated by a 2 mm small gap with a voltage of 9.5 kV between the first two neighbouring plates and the last two neighbouring plates.

The readout is done by strips in the endcap (aligned perpendicular to the beam) and in the barrel (aligned parallel to the beam), where the ϕ coordinate is measured with higher spatial resolution using the signal interpolation of adjacent strips than the r coordinate, which is only constrained by the strip length.

Muon System Performance

The transverse muon momentum is determined by measuring the track bending. The bending is defined by the sagitta s (Figure 4.12), which is inversly proportional to the transverse muon momentum

$$s = 0.3 \cdot L^2 \cdot \frac{B}{8\, p_T} \propto \frac{1}{p_T}, \tag{4.10}$$

where B is the magnetic field strength. The resolution obtained for the sagitta is therefore proportional to the transverse momentum resolution

$$\frac{\Delta s}{s} \propto \frac{\Delta p_T}{p_T}. \tag{4.11}$$

The uncertainty of the sagitta measurement is assumed to be independent of p_T, this leads to a linear increase of Δp_T with p_T. Together with a constant uncertainty, which is

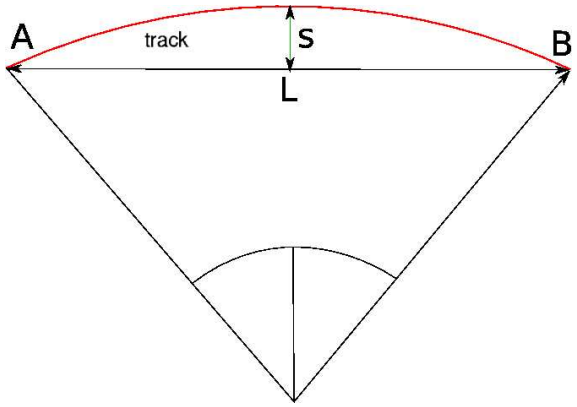

Figure 4.12: The muon track describes a circular path with the radius R via the points A and B. L is the distance between the two points.

due to multiple scattering of muons in the detector material, the total uncertainty of the transverse momentum is a function of p_T:

$$\frac{\Delta p_T}{p_T} = \sqrt{(m \cdot p_T)^2 + b^2}, \tag{4.12}$$

with the parameters m and b. These parameters have to be determined separately for the tracker and for the muon system. Due to the fact that the magnetic field lines are mostly parallel to the z-axis, the muon tracks are dominantly bended in the $r - \phi$ plane. In this case there is no difference between the uncertainty of the momentum measurement and the uncertainty of the transverse momentum measurement. To first approximation the transverse momentum resolution equals the momentum resolution.

The momentum resolution $\Delta p/p$ in dependency of the momentum is shown in figure 4.13. The muon momentum resolution of the muon system alone is compared to the resolution

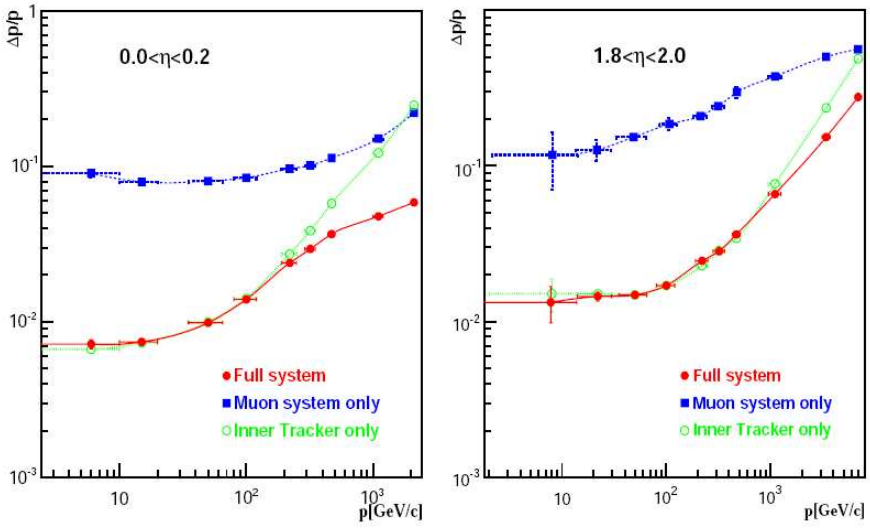

Figure 4.13: The momentum resolution versus p using the muon system only, the inner tracker only, or both ("full system") [1].

of the inner tracker system and the full system. The left plot shows the resolution for the barrel region $|\eta| < 0.2$, the right plot shows the slightly worse resolution for the endcap region, $1.8 < |\eta| < 2.0$. For low p muons the momentum resolution of the muon system is limited by multiple scattering and the best momentum resolution of the "full system" is given by the tracker. For muons with momenta greater than 100 GeV, the extrapolation of the muon track from the muon system back to the beam line can be used to improve the full momentum resolution. The spatial resolution of the muon chambers starts to dominate the momentum resolution. $4.5\%\sqrt{p/\mathrm{TeV}}$ provides a good phenomenologically description of the muon momentum resolution in this p_T region for barrel and endcap [24].

4.3.5 Luminosity and Luminosity Monitor

In order to determine the cross section σ of a certain process by measuring its event rate R, one needs to know the so called instantaneous luminosity $\mathcal{L}$.

$$R = \mathcal{L}\,\sigma \tag{4.13}$$

The luminosity decreases during the runtime of the LHC due to beam losses, and has therefore to be monitored.

At the LHC several possibilities to determine the luminosity are studied, see [1] for detailed information. One can distinguish between online techniques, which determine the average luminosity during the run at real time, and offline techniques which detemine the integrated luminosity.
One possible offline technique, at least at low luminosity is the usage of the TOTEM experiment [26]. TOTEM measures the number of elastic interactions N_{el} and N_{el}/dt, for small momentum transfer t, and the number of inelastic interactions N_{inel}. The so called Roman Pots of the TOTEM experiment are used for the measurment of N_{el} and N_{el}/dt and the forward inelastic detector of TOTEM and the hadronic forward calorimeter of CMS are used to measure N_{inel}.

Using the optical theorem, which relates the total cross section to the imaginary part of the forward scattering amplitude, the following relation between the total cross section and N_{el}, N_{inel} and dN_{el}/dt is obtained:

$$\sigma_{tot} = \left(\frac{dN_{el}}{dt}\right)_{t=0} \frac{16\pi}{N_{el}+N_{inel}} \frac{1}{1+\rho^2}, \tag{4.14}$$

where ρ is the ratio of the real to the imaginary part of the forward scattering amplitude. The error on the total cross section obtained by this method is expected to be smaller than 5% [55]. The total event rate is the sum of the event rates of elastic and inelastic processes. Because of this, the integrated luminosity L_{int} can be calculated by:

$$L_{int} = \frac{N_{inel}+N_{el}}{\sigma_{tot}} \tag{4.15}$$

TOTEM will operate at low luminosity with different machine optics, this will introduce additional uncertainties.

One could also use a special benchmark processes, like the production of W and Z bosons with precisely measured event rate and with well known cross section to calculate the luminosity by equation 4.1. The precision of this method is limited by the precision with which the event rate can be determined and by the theoretical uncertainties on the cross section and the inelastic parton density functions.

4.3.6 Trigger and Data Aquisition

The bunch crossing rate at the LHC is about 40 MHz. On average 20 interactions take place at one bunch crossing. The corresponding data rate in the CMS detector will be of the order of 1 MHz. Today's storage devices are restricted to a storage capability of about 100 Hz at data rates of ∼100 MB/s.

However, only the interactions where partons collide inelastically are of interest at the CMS detector.
The task of the trigger system is to reduce the amount of data, by identifying and storing only "interesting" events. To fulfill this task, the trigger system rejects or accepts events by certain criteria. The trigger system provides different triggers which vary in the used criteria. The user can choose the trigger which fits best for his analysis in terms of signal efficiency and background rejection. Criteria might be for example the lepton momentum or the amount of energy stored inside the calorimeters.

The CMS triggersystem works basically in two steps to surpress the storage of "uninteresting" events. The two steps are the Level 1 trigger and the High-Level trigger. The High-Level Trigger System can be roughly divided into Level-2 and Level-3 triggers. At each level the sorting criteria get stricter and the sorting more time consuming.

1. Level-1 trigger [19]:
   The Level-1 trigger uses coarsely segmented detector data from muon detectors and calorimeters. The information of different subsystems is not combined. The high-resolution data is held in pipeline memories. The Level-1 trigger is based on custom electronics. The decision has to be available only 3.2 μs after the corresponding bunch crossing, to limit the amount of data stored in the pipeline memories. The Level-1 trigger lowers the passed rate of events to 100 kHz. Different thresholds are used for low and high luminosity scenarios, due to the different amount of data. Once the Level 1 trigger accepts an event, the high-resolution data is readout of the front-end electronics and then piped to the High-Level trigger.

2. High-Level Trigger (HLT) [27]
   The decision of this trigger system is based on PC farms and not on hardware processors. A Level-2 trigger uses typically only the information from the calorimeter and the muon system. For the Level-3 triggers the information from distinct detector parts are combined and full tracks are reconstructed. The HLT system reduces the event rate to 100 Hz.

The special set of trigger choosen in this analysis will be described in chapter 7.1 .

Chapter 5

CMS Software

To study the possiblity of finding or excluding a certain process with a detector, this specific process, backgrounds which can fake the signature of the process and corresponding detector signals have to be simulated. Once the detector is delivering data the detected signals can be compared to the expected signal of the simulation.

The simulation of signal and background processes is done by so called event generators:

5.1 Event Generators

LHC Monte Carlo event generators like PYTHIA [28], HERWIG [29] and TopRex [30] can be used to simulate the generation of events, i.e. sets of outgoing particles produced in the interaction between two incoming particles. The event properties should be described as accuratly as possible. To simulate the generation of an event, event generators need certain parameters as input:

- The parton density functions (Section 4.1), determined by experiments.
- The cross section of elementary particle interactions, calculated to a certain level of accuracy using the underlying theory of physics.
- The decay products and branching ratio of unstable hadrons.
- Models which describe the hadronization of quarks.
- The model parameters for the generation of Beyond Standard Model processes, like the one studied in this diploma thesis (Section 3.7). This parameters are for example the mass of the generated particle and its coupling constants.

These parameters can be set in CMKIN [31] datacards. The CMKIN package offers a way to inerface event generators with the CMS detector simulation. CMKIN is based on the programming language Fortran [32].
CMKIN datacards can also be used for initiating so called pre-selection cuts. These pre-selection cuts limit the amount of generated and stored events. Only the events get stored

which fulfill the pre-selection criteria. This reduces the computing time used to generate and reconstruct all events. CMKIN can convert the generator internal event structure to a common block HEPEVT, a standard to store the kinematic information of particles, and from HEPEVT to HBOOK n-tuples. The n-tuples can be used as an input to the detector simulation packages. The n-tuples contain the decay chain for a process. The decay chain consists of the following information about each particle in a process: type, mother particle, momentum, energy, mass and the point of creation.

The event generator used for the generation of the signal events in this diploma thesis is PYTHIA. In addition to the full event simulation provided by PYTHIA, the hard process kinematics of some of the background processes have been generated using CompHEP [33]. The Event Generator CompHEP calculates the kinematics of multiparticle final states in collision and decay processes.

5.2 Detector Simulation

- OSCAR
  OSCAR (Object-Oriented Simulation for CMS Analysis and Reconstruction) [34] takes the CMKIN output and simulates the interaction of the generated particles with the detector. In combination with GEANT4 (Geometry and Tracking) [35], the whole (planned) detector, magnetic fields, material distribution and properties are simulated. The energy loss and scattering of particles and their decay products along with their path through the detector is calculated. Due to the high complexity of this process it takes about 5 hours for 1000 events. This is large in comparison to the 6 minutes CMKIN needs for generating the same amount of events.

- ORCA digitisation
  ORCA (Object-Oriented Reconstruction for CMS Analysis) [36] takes the OSCAR output and simulates the response of the readout electronics. Before the detector signals get digitized by OSCAR, pile-up signals and minimum bias events get mixed with the signal event. Pile-up signals are generated by particles from previous bunch crossings which still linger inside the detector. Minimum bias events are events from other collisions, elastic and inelastic, at the same bunch crossing. The amount of this pile-up and minimum bias events enlargens with higher luminosity. Therefore two scenarios with different amount of pile-up and minimum bias events can be chosen with OSCAR, the low luminosity scenario $\mathcal{L} = 2 \cdot 10^{33}\mathrm{cm}^{-1}\mathrm{s}^{-1}$ and the high luminosity scenario $\mathcal{L} = 10^{34}\mathrm{cm}^{-1}\mathrm{s}^{-1}$. In this diploma thesis the pair production of doubly charged Higgs bosons has been studies for the low luminosity scenario. See [1] for further information about minimum bias events and pile-up at the LHC.

- ORCA reconstruction
  High-level objects, like particle tracks, vertices and their parameters get reconstructed by ORCA. This part of the reconstruction is the same for real and simulated events. Different reconstruction mechanisms optimized for special tasks, for example the reconstruction of muon tracks using the whole detector information, can be

choosen at this stage. The information about several trigger levels is also accessible at this level, and can be used to select events which are interesting for a special analysis. The output of this part of the analysis is stored in so called DST-files (Data Summary Tape files) and can be analysed with different program packages. The package used for this diploma thesis is called PAX.

- PAX
  PAX (Physics Analysis eXpert) [37] is a toolkit based on the programming language C++. It provides ready made containers for physical objects like fourvectors, vertices and collisions. The objects stored in these containers can easily be accessed and linked with each other, to describe a full decay chain. Objects like four vectors can also be combined to test several hypotheses about the decay chains. PAX can keep different event interpretations simultaneously and add new event interpretations. Figure 5.1 shows the container structure in PAX.

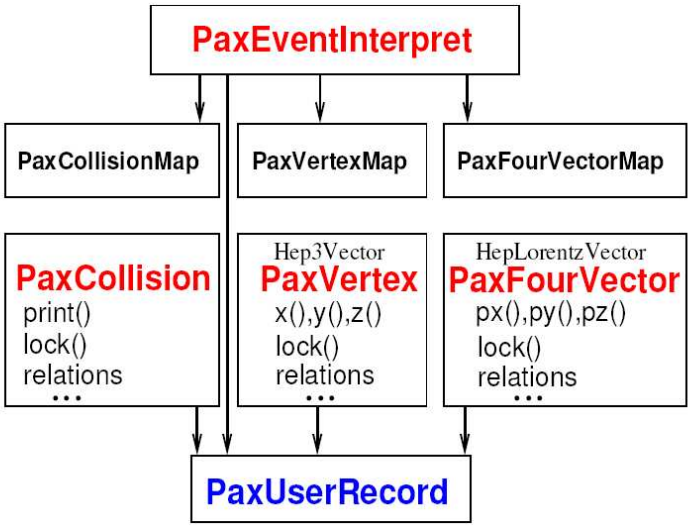

Figure 5.1: The basic unit in PAX: the event interpretation together with the classes for collisions, vertices, fourvectors and user records [38].

5.3 Computing with GRID

The simulation, reconstruction and analysis of the huge amount of data for the CMS detector requires storage, networking and processing power, which exceeds by far the capabilities of CERN′s central computing systems. The idea of the CMS computing system is therefore, to distribute the computational power over a worldwide network of computer clusters, called the LHC Computing Grid. The main center of this network are the computing systems at CERN. Different sub-centers, are located all over the world. The challenge of the LHC Computing Grid is the seamless exploitation of these different centers. Users, data-samples and software have to be linked with each other, by keeping the time span needed for this linking process as small as possible. For further information about the CMS computing system see [39] and [40].

Chapter 6

$H^{\pm\pm}$ at Generator Level

As mentioned in chapter 3, this analysis will deal with the doubly charged Higgs boson of Δ_L triplet representations, which does not couple to right handed fermions. This doubly charged Higgs boson is predicted by Higgs triplet models. In the following it will be called $H^{\pm\pm}$, for simplicity. The studied production process is pair production. A branching ratio of 100% into muons is assumed. The coupling constant $h_{\mu\mu}$ of $H^{\pm\pm}$ to muons has been chosen as $h_{\mu\mu} = 0.1$ which is consistent with experimental constraints (see chapter 3.6.1) and forces the doubly charged Higgs boson to decay before it reaches the tracker.

6.1 Event Generation

6.1.1 Signal

The Monte Carlo event samples for the signal have been generated at leading order (LO) using the event generator PYTHIA 6.227 in combination with CMKIN_4_3_ 1 (Section 5.1). A collection of signal datasets has been produced for $m_{H^{\pm\pm}}$ ranging from 100 GeV to 900 GeV. The number of signal events has been scaled to next-to-leading order (NLO) expectations using the NLO cross sections calculated by Spira and Mühlleitner [13]. These corrections increase the cross section by about 20 - 30%. The NLO corrections are the standard QCD corrections for the Drell-Yan process, with virtual gluon exchange, gluon emission and quark emission in the initial state. The uncertainties on these cross sections are 10 - 15%, this includes systematic uncertainties of the parton density functions. Figure 6.1 shows the cross section in LO and NLO. In Table 6.1 the number of generated events can be compared to the number of expected events calculated with the NLO cross section for an integrated luminosity of 10 fb^{-1}.

It can be seen that the number of generated signal events exceeds by far the number of expected events, this minimizes the statistical error of the studies done with the generated data samples.

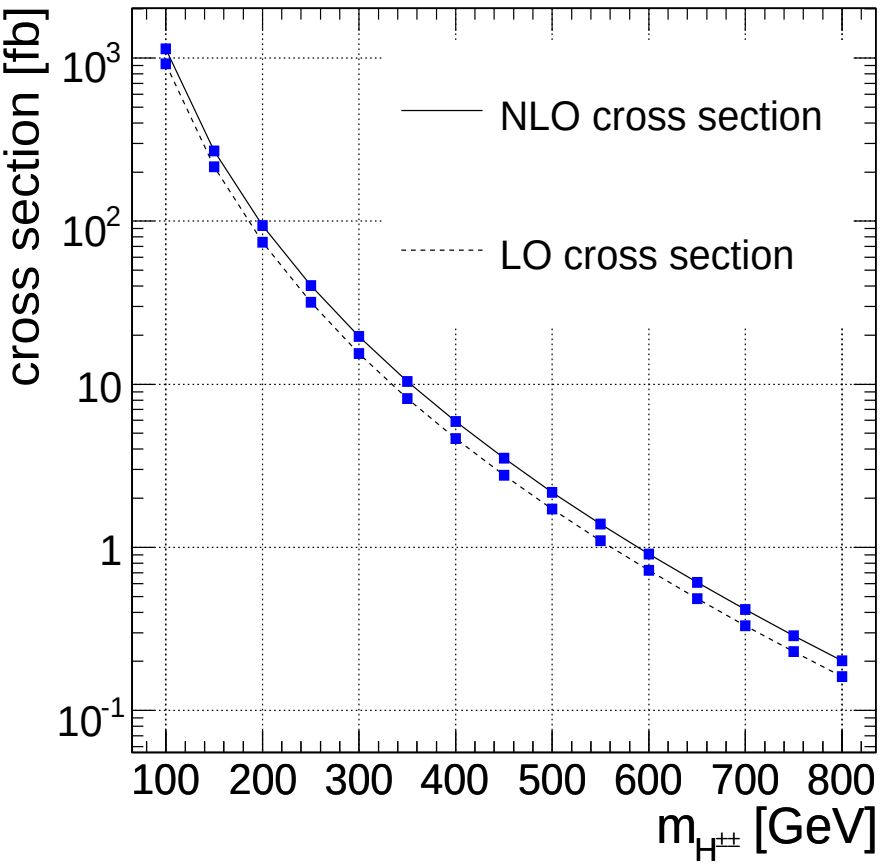

Figure 6.1: Cross section for pair production of $H^{\pm\pm}$.

$m_{H^{\pm\pm}}$ in GeV	Number of generated events	Number of expected events for 10 fb^{-1}
200	8837	939
300	9000	196
400	1350	59
450	5000	35
550	5000	14
600	2500	9
650	5000	6
700	4840	4
750	4860	3
800	5000	2
900	5000	1

Table 6.1: Number of events generated with PYTHIA for different Signal Data samples (before any preselection) and the number of expected events calculated with the NLO cross section [13] for an integrated luminosity of 10 fb^{-1}.

6.1.2 Background Processes

Important background processes with a possible four muon final state are:

- $pp \to t\bar{t} \to W^+W^-b\bar{b} \to 2\mu + 2\mu + X$ (called $t\bar{t}$ background)
- $pp \to \left(Z^{(*)}/\gamma^*\right) b\bar{b} \to 2\mu + 2\mu + X$ (called $Z\bar{b}b$ background)
- $pp \to \left(Z^{(*)}/\gamma\right) \left(Z^{(*)})/\gamma\right) \to 2\mu + 2\mu$ (called $ZZ \to 4\mu$ background)
- $pp \to \left(Z^{(*)}/\gamma\right) \left(Z^{(*)}/\gamma\right) \to 2\tau + 2\mu$ (called $ZZ \to 2\mu 2\tau$ background)

The background contribution from $b\bar{b}$ production has also been investigated. $b\bar{b}$ background is the QCD background which yields the highest probabilty to fake events with multiple muons. This background will be discussed separately in chapter 9, as it has been found to be negligible after trigger selection and by requiring four reconstructed muons.

The $t\bar{t}$ event sample is generated using PYTHIA with CMKIN_1_1_0 including LO processes $gg \to t\bar{t}$ and $q\bar{q} \to t\bar{t}$. The W bosons in the $t\bar{t}$ data sample are forced to decay into electrons, muons and taus. The tau leptons are forced to decay into electrons and muons.

The $Z\bar{b}b$ and the ZZ backgrounds originate either from gluons or quarks in the initial state. The $Z\bar{b}b$ sample is generated using CompHEP 4.2 and PYTHIA with CMKIN_3_1_0. The Z boson in the $Z\bar{b}b$ sample is generated with $m_{Z/\gamma*} > 5$ GeV and is forced to decay into muons. The b and $\bar{b}$ quarks decay without constraints.

For the ZZ background samples only the production from $q\bar{q}$ collisions is simulated, as neither PYTHIA nor compHEP include the process $gg \to \left(Z^{(*)}/\gamma^*\right) \left(Z^{(*)}/\gamma^*\right)$. The $gg \to ZZ^{(*)}$ cross section was estimated to be 20% [41] of the $q\bar{q} \to ZZ^{(*)}$ cross section at leading order. The next-to-leading-order corrections are still unknown. The LO generation of the process $q\bar{q} \to ZZ^{(*)}$ is done using CompHEP as it includes both t- and s-channel diagrams (Figure 6.2 and Figure 6.3). In the $ZZ \to 4\mu$ sample both Z bosons are forced to decay into muons. In the $ZZ \to 2\tau + 2\mu$ sample one Z boson is forced to decay muonically, the second one is forced to decay into taus. The muons generated in Z decays are forced to be generated with $p_T > 3$ GeV and $|\eta| < 2.5$. The taus decay without constraints.

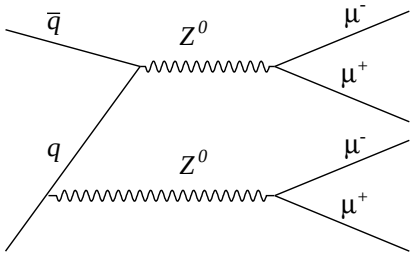

Figure 6.2: t-channel Feynman diagram for the process $q\bar{q} \to ZZ^{(*)}$.

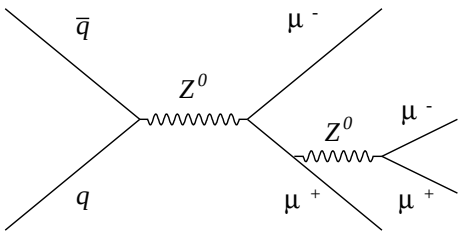

Figure 6.3: s-channel Feynman diagram for the process $q\bar{q} \to ZZ^{(*)}$.

All processes are generated at LO. The cross sections obtained at LO are scaled to NLO. For the $t\bar{t}$ sample the NLO total cross section is 840 pb [42]. Thus using the branching

ratios $Br(W \to l\nu)$, $Br(\tau \to \mu\nu\nu)$ and $Br(\tau \to e\nu\nu)$ taken from the Particle Physics Booklet [43] the NLO cross section for the produced sample is calculated to be 53 pb. For the $Z\bar{b}b$ sample the NLO order cross section, 278.4 pb, is obtained by scaling the LO value of 116 pb, provided by CompHEP, with a K-factor $K_{NLO} = 2.4 \pm 0.3$, calculated with MCFM [44]. The LO cross sections for $ZZ \to 4\mu$ and $ZZ \to 2\mu 2\tau$ are respectively 113 fb and 157 fb. The NLO cross section for the ZZ backgrounds is scaled by means of the K factor $K_{NLO} = 1.35$ [45]. It is evaluated for the t-channel contribution with MCFM and MadGraph [46].

The NLO cross sections for the four most important backgrounds can be seen in Table 6.2.

backgrounds	$ZZ \to 4\mu$	$ZZ \to 2\mu + 2\tau$	$Z\bar{b}b$	$t\bar{t}$
NLO cross section σ [fb]	153	212	$278 \cdot 10^3$	$53 \cdot 10^3$

Table 6.2: NLO cross sections for background datasamples. In the $ZZ \to 4\mu$ datasample the Z bosons are forced to decay into four muons with $p_T > 3$ GeV and $|\eta| < 2.5$. In the $ZZ \to 2\mu 2\tau$ datasample one Z boson is forced to decay into muons with $p_T > 3$ GeV and $|\eta| < 2.5$ and one is forced to decay into taus with $p_T > 3$ GeV. The NLO cross section for the Zbb background includes the branching ratio $Z \to 2\mu$ the b quarks decay without constraints. In the $t\bar{t}$ sample the W bosons are forced to decay leptonically. If taus are produced in this decay, these taus are forced to decay into electrons and muons.

6.2 $H^{\pm\pm}$ properties at Generator Level

6.2.1 $H^{\pm\pm}$ mass distribution

One basic property of the doubly charged Higgs boson is its decay width, which is given by:

$$\Gamma(H^{\pm\pm} \to \mu^{\pm}\mu^{\pm}) = \frac{m_{H^{\pm\pm}}}{8\pi} |h_{\mu\mu}|^2 , \tag{6.1}$$

For the chosen coupling constant of $h_{\mu\mu} = 0.1$ the decay width becomes very narrow. It increases only linearly with the mass. The width of the mass distribution corresponds to the decay width of the doubly charged Higgs bosons, which have been produced in a Breit-Wigner resonance. Figure 6.4 shows the mass distributions of doubly charged Higgs bosons with masses of 200 and 900 GeV, and the fitted Breit-Wigner curves. The width of the fitted curves are 0.08 ± 0.02 GeV and 0.4 ± 0.2 GeV, they are compatible with the calculated decay widths of ~ 0.08 GeV and ~ 0.36 GeV, respectively.

6.2.2 p_T and Energy distribution of $H^{\pm\pm}$

Two other characteristic quantities of the doubly charged Higgs boson are its transverse momentum and its energy. As doubly charged Higgs bosons are pair produced and energy

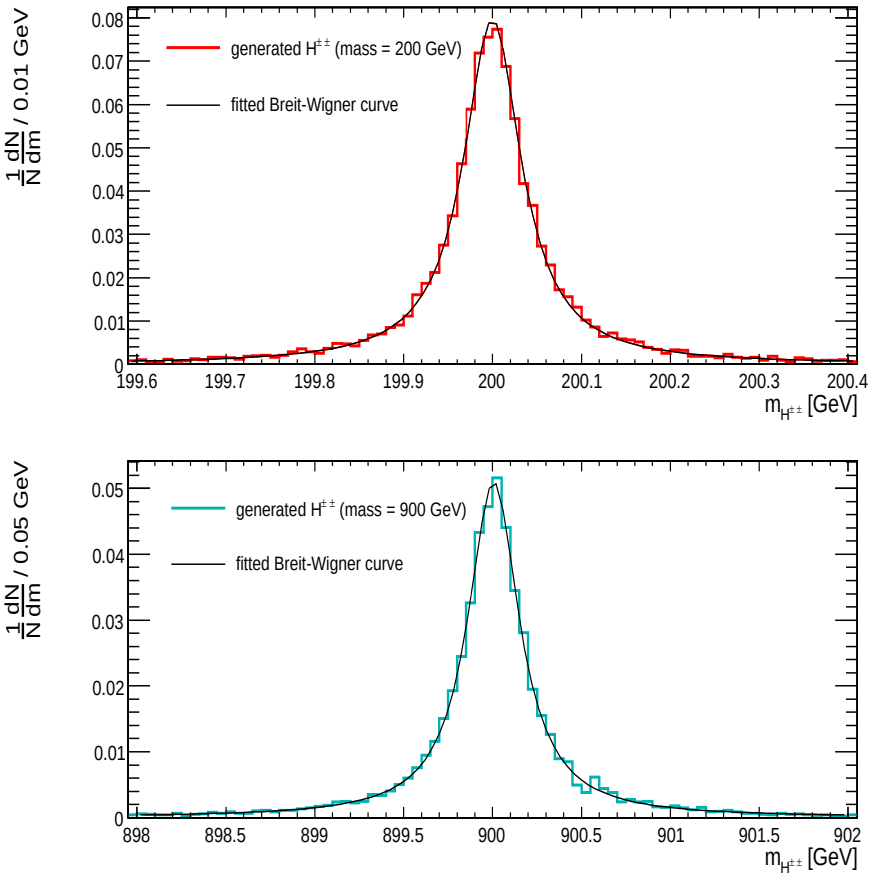

Figure 6.4: Mass distribution of the generated $H^{\pm\pm}$ for a mass of 200 GeV (upper plot) and a mass of 900 GeV (lower plot). Breit-Wigner curves have been fitted to both distributions.

is conserved, the energy E_1 and E_2 of the two Higgs bosons is related to the centre of mass energy E_{cm} of the two interacting partons by:

$$E_{cm} = E_1 + E_2, \tag{6.2}$$

assuming that no other particles have been generated i.e. initial and final state radiation are neglected. The probability for two partons to collide with a centre of mass energy E_{cm}, decreases with E_{cm}. This leads to a decreasing energy distribution of the pair produced doubly charged Higgs boson. Figure 6.5 shows the energy distribution for three different doubly charged Higgs boson masses. Due to the relation between total energy, momentum and rest-mass of a particle:

$$E^2 = p^2 + m^2, \tag{6.3}$$

it is necessary that $E \geq m$, this can also be seen in Figure 6.5. Figure 6.6 shows the transverse momentum distribution which is independent of longitudinal boosts. The distributions get more shallow and peak at higher momenta for larger doubly charged Higgs boson masses. This is in principle due to the relation 6.3. As already mentioned, the energy needed to generate a particle increases with its mass. If the provided energy is greater than the mass of the particle, it is not generated at rest but with a certain momentum

$p = \sqrt{E^2 - m^2}$. The same difference between provided energy and mass leads for heavier particles to higher resulting momenta than for lighter particles. Using this relation and the energy distributions of Figure 6.5 the momentum distributions of Figure 6.6 become understandable.

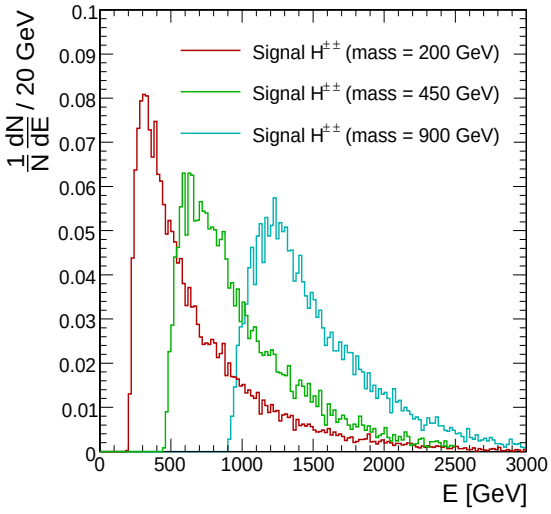

Figure 6.5: Total energy distribution of the generated $H^{\pm\pm}$.

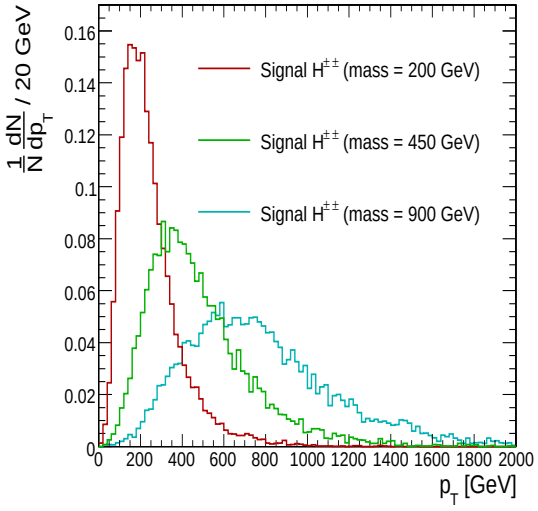

Figure 6.6: Distribution of p_T values of the generated $H^{\pm\pm}$.

6.2.3 $H^{\pm\pm}$ Angular Distributions

Figure 6.8 and Figure 6.7 show the angular distribution of the generated doubly charged Higgs bosons.

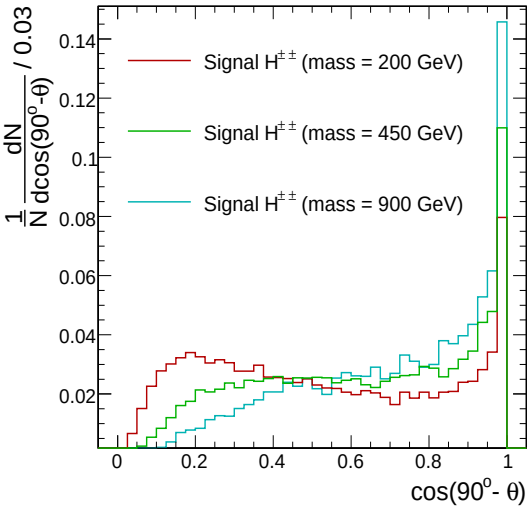

Figure 6.7: Distribution of $\cos(90^o - \theta)$ values of the generated $H^{\pm\pm}$.

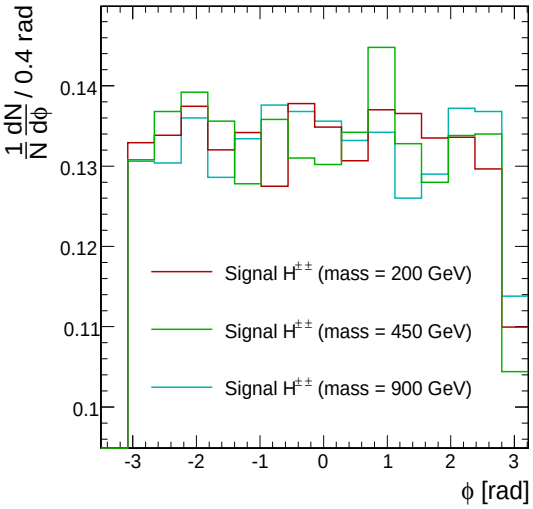

Figure 6.8: Distribution of ϕ values of the generated $H^{\pm\pm}$.

Figure 6.7 shows the $\cos(90^o - \theta)$ distribution of doubly charged Higgs bosons for three different masses. If doubly charged Higgs bosons would fly homogenously in all directions, the $\cos(90^o - \theta)$ distribution would be flat. Instead the distributions peak at $\cos(90^o - \theta) = 1$, thus doubly charged Higgs bosons fly mainly transverse to the beam line. With decreasing doubly charged Higgs boson masses, and therefore decreasing p_T, the distributions get more shallow. Low p_T doubly charged Higgs bosons fly more often along the beam line.

The two pairproduced doubly charged Higgs bosons are uniformly distributed in ϕ as can be seen in Figure 6.8. The distance in ϕ between the two Higgs bosons is shown in Figure 6.9. This distance peaks strongly at $\Delta\phi \sim 3.1$ rad. The two Higgs bosons are emitted mostly in opposite directions in ϕ, as expected if γ/Z decay almost in rest.

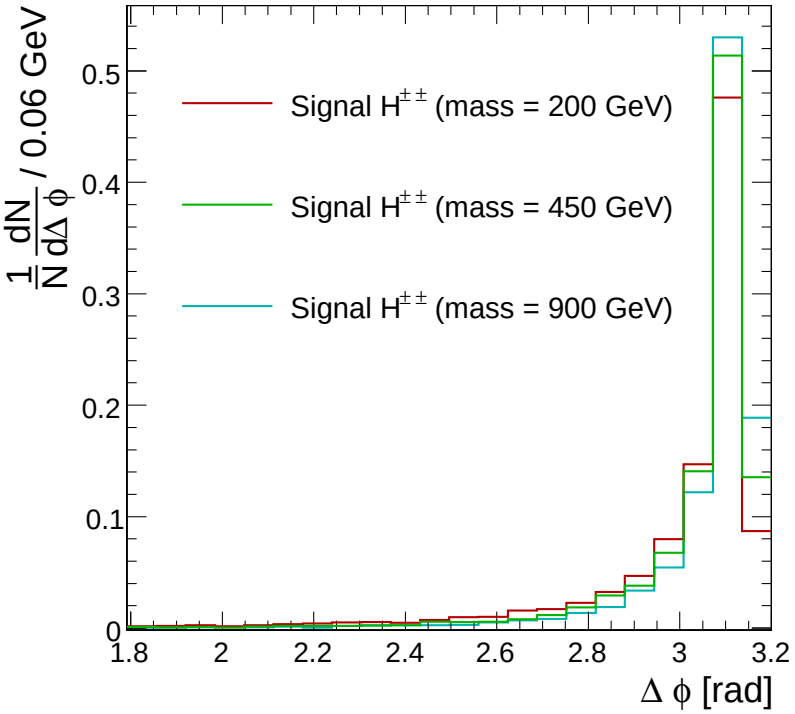

Figure 6.9: Distribution of the distance in ϕ between H^{++} and H^{--}.

6.2.4 $H^{\pm\pm}$ Decay Products

Each of the two generated doubly charged Higgs bosons decays into two equally charged muons. These muons may be detected with the CMS muon system. Figure 6.10 shows the momentum distribution of the generated muons. In Section 6.2.2 the increase of the transverse momentum of $H^{\pm\pm}$ with its mass has been described. Due to momentum conservation the muons generated in $H^{\pm\pm}$ decays show the same dependency of the transverse momentum on the $H^{\pm\pm}$ mass. Figure 6.11 shows the pseudo-rapidity distribution of the muons. Due to the lower transverse momentum, muons generated in the decay of light doubly charged Higgs bosons show a more shallow distribution than muons generated in the decay of heavier doubly charged Higgs bosons.

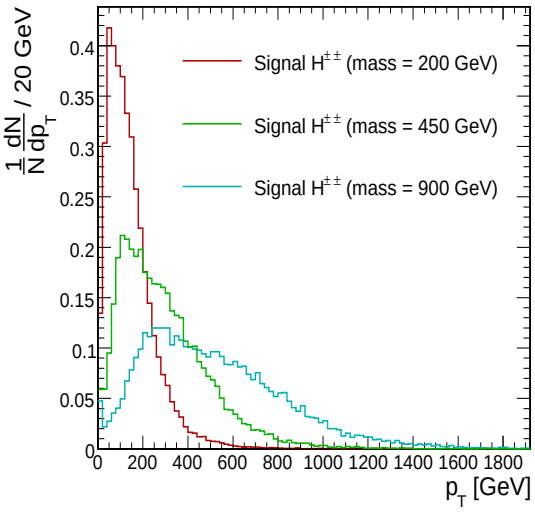

Figure 6.10: Transverse momentum distribution of the muons generated in $H^{\pm\pm}$ decays.

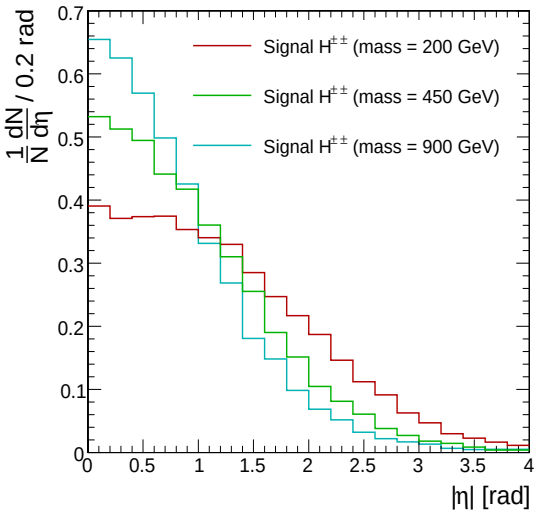

Figure 6.11: Distribution of the $|\eta|$ values of the muons generated in $H^{\pm\pm}$ decays.

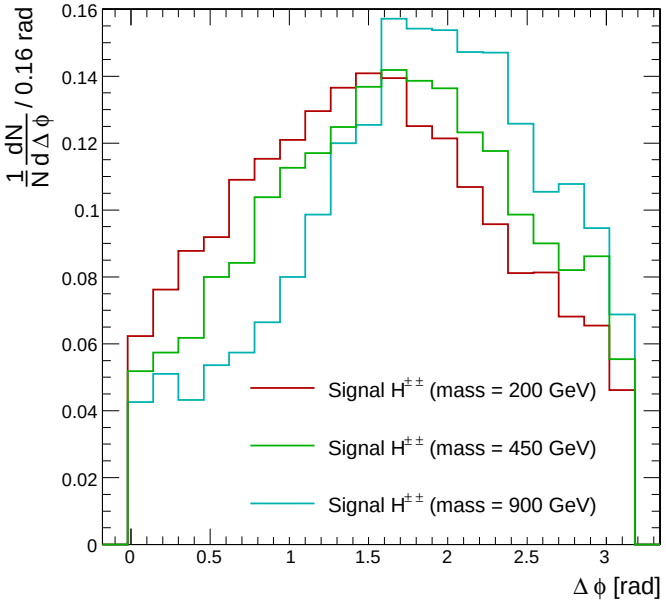

Figure 6.12: Distribution of the distance in ϕ between two same sign muons, generated in $H^{\pm\pm}$ decays.

The distance in ϕ between two same sign muons is shown in Figure 6.12. This distribution peaks at a distance of 90° between the muons. The distribution is shifted to larger $\Delta\phi$ values for larger doubly charged Higgs boson masses.

6.3 Reconstructed Invariant $H^{\pm\pm}$ mass

In order to reconstruct the doubly charged Higgs bosons, the generated muons are divided into positive and negative charged muons and sorted with increasing p_T. The invariant masses of the two highest p_T muons with positive charge and of the two highest p_T muons with negative charge are calculated. It is assumed that these calculated invariant masses correspond to the invariant masses of the doubly charged Higgs Bosons (Figure 6.13). In this analysis it has been checked that at generator level the four highest p_T muons correspond to the four muons of the Higgs decays.

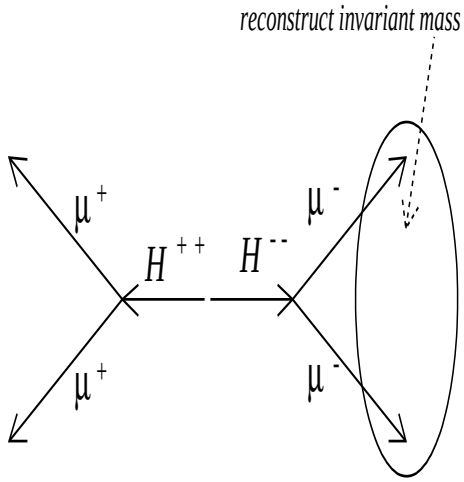

Figure 6.13: To reconstruct the mass of $H^{\pm\pm}$, the invariant mass of two muons with the same charge is calculated.

In Figure 6.14 the mass distribution of the reconstructed doubly charged Higgs bosons is compared to the mass distribution of the generated doubly charged Higgs bosons for the signal samples with $m_{H^{\pm\pm}} = 200$ GeV and 900 GeV. The number of events is normalized to 10 fb^{-1}. Whereas the distributions of the generated doubly charged Higgs boson masses are symmetric about the mean values of 200 GeV and 900 GeV, respectively, the distributions of the reconstructed doubly charged Higgs boson masses show an asymmetry. Due to the final state radiation reconstructed doubly charged Higgs boson masses are in general smaller than generated masses. Thus the number of reconstructed masses smaller than the mean value exceeds the number of reconstructed masses larger than the mean value.

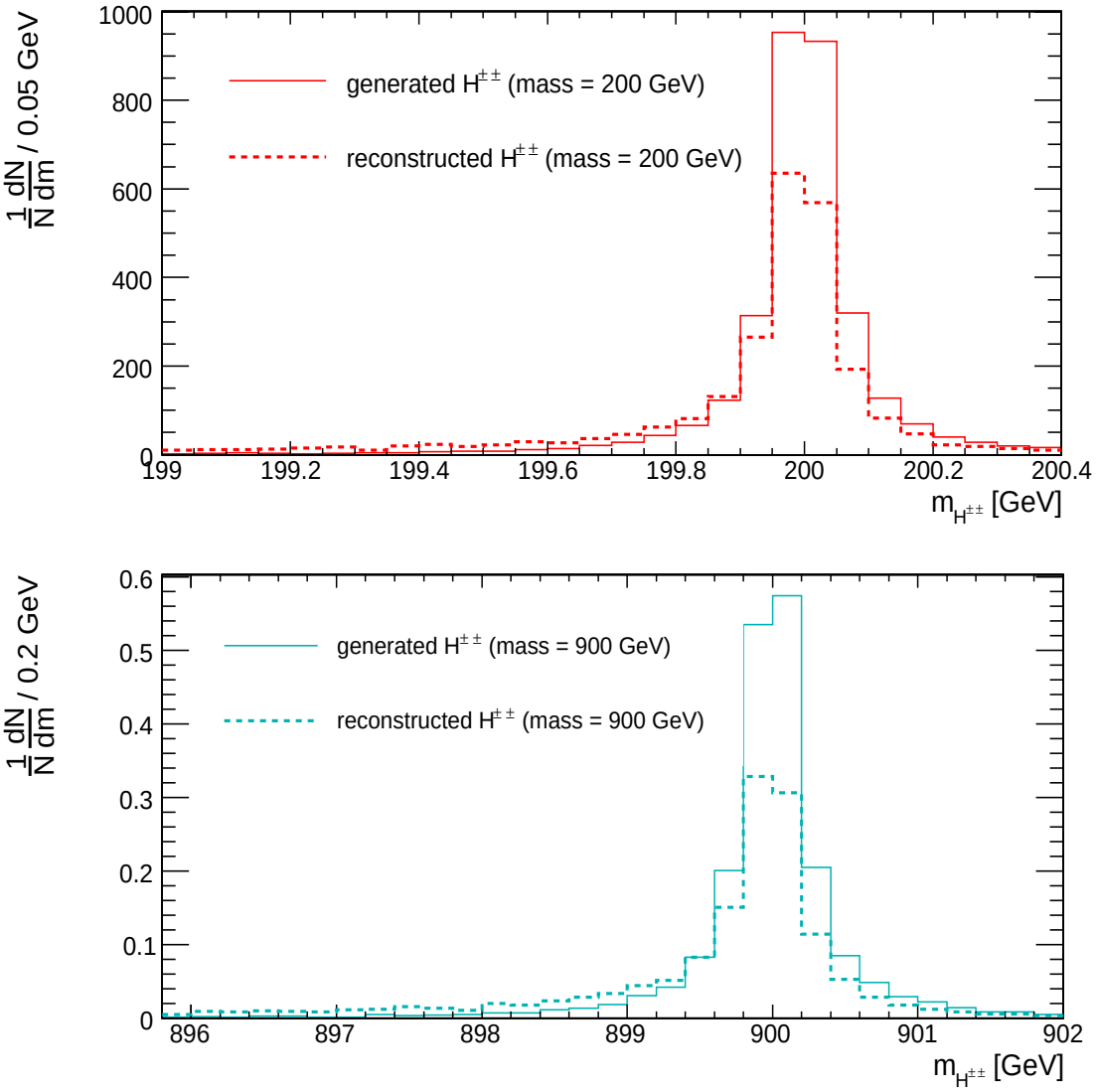

Figure 6.14: The mass distribution of the generated doubly charged Higgs bosons compared to the mass distribtution of the reconstructed doubly charged Higgs bosons (the procedure is described in section 6.3). The upper plot shows the mass distributions for the signal sample $m_{H^{\pm\pm}} = 200$ GeV, the lower plot shows the mass distributions for the signal sample $m_{H^{\pm\pm}} = 900$ GeV. The event numbers have been normalized to an integrated luminosity of 10 fb^{-1}.

6.4 Generator Level Pre-selection

To reduce the amount of time needed to reconstruct signal and background events, cuts have been applied on generator level. These cuts are called pre-selection cuts. Pre-selection cuts have to be chosen much softer than the final cuts in the analysis, in order to ensure that the final number of selected events is not affected by the pre-selection cuts.

On each sample the following preselection cuts have been applied:

- The final state of an event should contain at least two positively and two negatively charged muons;
- All these muons should have a transverse momentum of $p_T(\mu)$ >3 GeV and a pseudorapidity $|\eta(\mu)| < 2.4$.

6.4.1 Signal

The signal samples can be studied before and after the pre-selection. The distributions of characteristic quantities before the pre-selection can be used to estimate the pre-selection efficiency of each single cut.

The requirement on the number of generated positively and negatively charged muons is fulfilled all the time, as the doubly charged Higgs bosons are forced to decay into two equally charged particles.
If more than four muons have been generated, then the muon with the fourth highest transverse momentum determines if an event is selected or not. If this muon has a momentum smaller than 3 GeV this event will not be selected. The plots in Figure 6.15 show the momentum distribution of the fourth highest p_T muon. The plot on the left shows the full distribution up to a momentum of 500 GeV. The plot on the right shows the distribution up to a momentum of 100 GeV. The transverse momentum increases with the doubly charged Higgs boson mass. Therefore the cut on $p_T > 3$ GeV reduces a higher percentage of the events which are generated at small doubly charged Higgs boson masses.

With respect to the events with at least four muons, which have $p_T > 3$ GeV, only the events are chosen, where at least four of these muons have also an absolute pseudo-rapidity of $|\eta| < 2.4$.
Figure 6.16 shows the $|\eta|$ distribution of the fourth lowest $|\eta|$ value of the muons with $p_T > 3$ GeV. The distribution gets more shallow and peaks at higher $|\eta|$ for decreasing doubly charged Higgs boson masses. The cut on $|\eta| < 2.4$ reduces a higher amount of events corresponding to small doubly charged Higgs boson masses.

The total pre-selection efficiency for the signal data samples with $m_{H^{\pm\pm}} = 200$ GeV, 450 GeV and 900 GeV is shown in Table 6.3. As expected, the efficiency increases with the mass of the doubly charged Higgs boson.

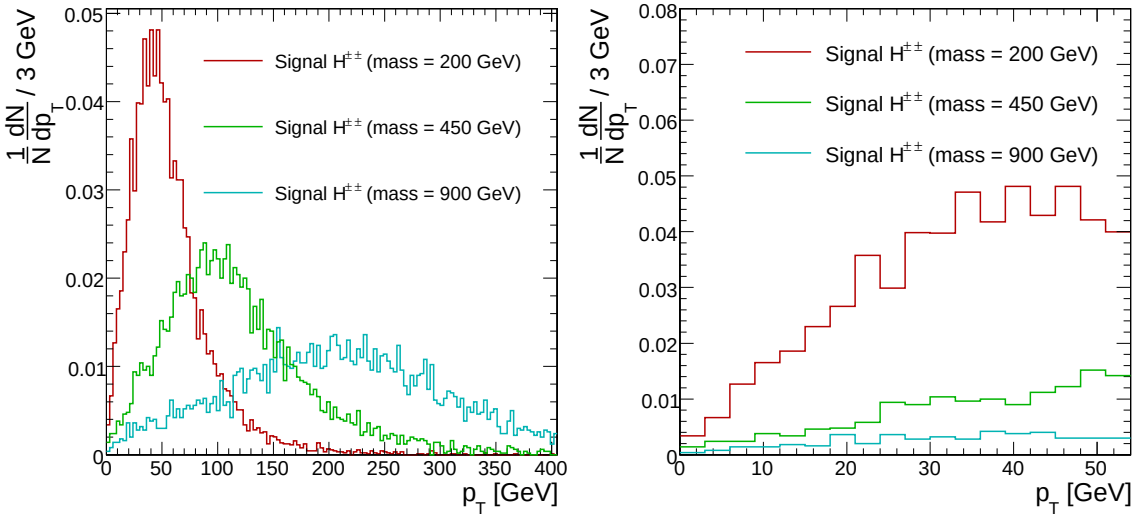

Figure 6.15: On generator level four muons with $p_T > 3$ GeV are selected. This plot shows the distribution of the fourth highest muon momentum of all muons in one event. The distribution is shown for the signal samples $m_{H^{\pm\pm}} = 200$ GeV, 450 GeV and 900 GeV for two different ranges of the momentum.

m($H^{\pm\pm}$) in GeV	200	450	900
pre-selection efficiency in %	70 ± 1	84 ± 2	90 ± 2

Table 6.3: Pre-selection efficiency ϵ for signal datasamples with m($H^{\pm\pm}$) = 200, 450 and 900 GeV, the errors are statistical only

6.4.2 Background

The background samples are officially generated samples and can only be studied after the pre-selection cuts have been applied.
Special care has to be taken of the forced tau decay in the $t\bar{t}$ sample. The forced decay of taus into electrons and muons leads to wrong pre-selection efficiencies, since PYTHIA uses wrong branching ratios for forced subsequent multiple decays. Each selected event has to be reweighed in order to get the correct pre-selection efficiency. The event weigth depends on the number of taus forced to decay into muons. The applied corrections are described in [47].
Table 6.4 shows the reweighted number of generated background events after pre-selection and the corrected pre-selection efficiencies [47], i.e. the number of reweighted events after the pre-selection divided by the number of events before the pre-selection.

Background	$ZZ \to 4\mu$	$ZZ \to 2\mu + 2\tau$	$Z\bar{b}b \to 4\mu$	$t\bar{t} \to 4\mu$
Number of selected events	118000	10000	112500	55717
Pre-Selection efficiency in %	57.3	0.8	0.1	0.3

Table 6.4: Number of generated events in the background Monte Carlo data samples, after pre-selection

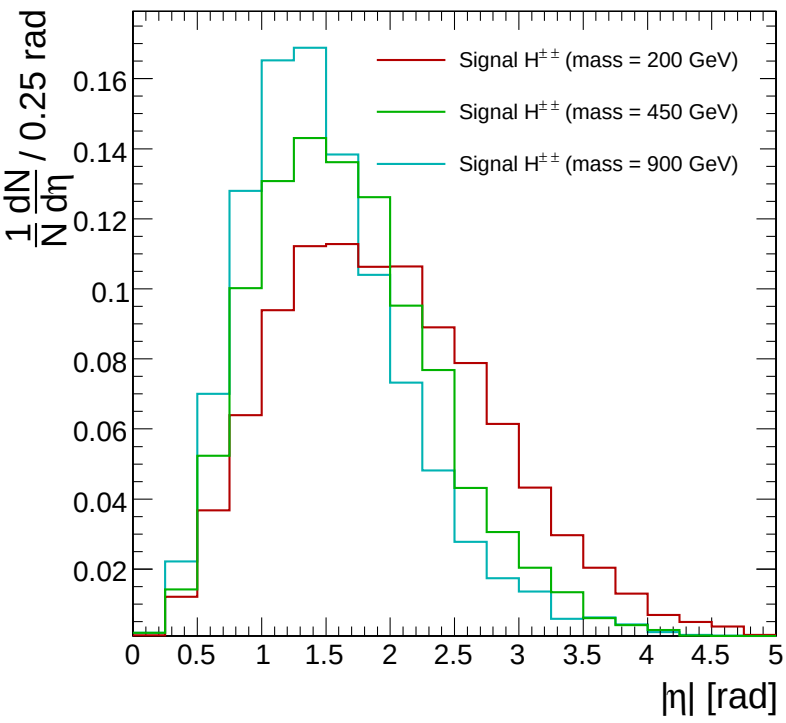

Figure 6.16: The distribution of the fourth lowest $|\eta|$ value of the muons with $p_T > 3$ GeV.

The relatively low pre-selection efficiencies can be understood by looking at each pre-selection cut.

The cut on the number of generated muons will reduce the number of events in all background samples, except the $ZZ \to 4\mu$ sample, where the generation of four muons is forced. In all other background samples only the generation of two muons is forced, other muons can be generated in inclusive b decays ($Zb\bar{b}$ and $t\bar{t}$ sample) or τ decays ($ZZ \to 2\mu 2\tau$ sample).

Figure 6.17 shows the distribution of the fourth highest muon momentum in one event. The cut on $p_T > 3$ GeV is clearly visible. In contrast to the same distribution for signal events (Figure 6.15) this distribution peaks at very low p_T. Especially the $Zb\bar{b}$ background contains very low p_T muons generated in b decays. The $ZZ \to 4\mu$ background will not be reduced by this cut, as the muons are generated with $p_T > 3$ GeV.

Figure 6.18 shows the distribution of the fourth lowest $|\eta|$ value of muons with $p_T > 3$ GeV. The cut on $|\eta| < 2.4$ is clearly visible. Compared to the signal samples in Figure 6.16, the distributions of the muons in the background samples peak at relatively high $|\eta|$ values. The sample which peaks at the highest $|\eta|$ values is the $ZZ \to 2\mu 2\tau$ sample, therefore this sample is reduced the most by this cut.

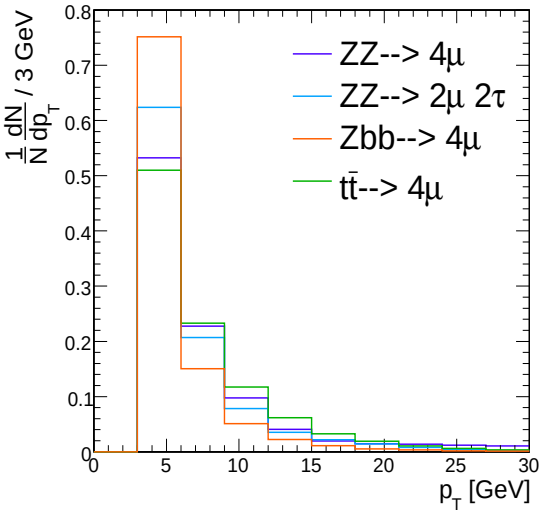

Figure 6.17: Distribution of the fourth highest transverse muon momentum in one event.

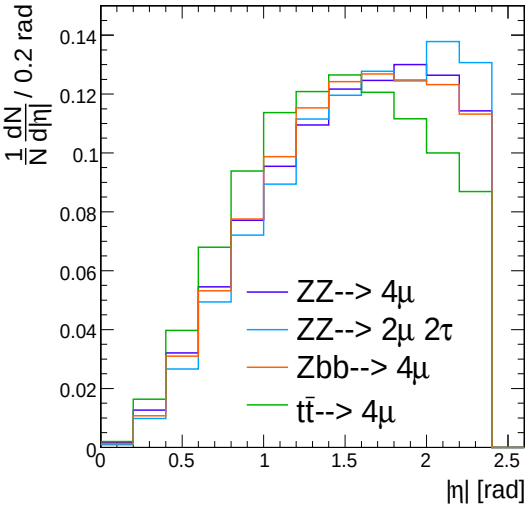

Figure 6.18: Distribution of the fourth lowest $|\eta|$ value of the muons with $p_T > 3$ GeV.

Chapter 7

Online Selection and Reconstruction

The signal of this study is characterized by four muons in the final state. A good muon reconstruction is therefore crucial.

The muon reconstruction at CMS can be divided into two parts: The online selection and the offline reconstruction. For both parts the concept of "regional reconstruction" is used. Regional reconstruction reduces the amount of information needed for the reconstruction of a physical object, i.e. the reconstruction is done for only a part of the detector.

Common of the two parts of the muon reconstruction are the standalone muon reconstructor (named Level-2 for online selection) and the global muon reconstructor (named Level-3 for online selection).

7.1 Online Selection

As described in chapter 4.3.6, the online selections can be divided into three levels, where Level-1 is based on custom electronics and Level-2 and Level-3 (both belong to the HLT) are so called software triggers. The Level 1 muon trigger uses all three types of muon detectors in the CMS muon system, Drift Tubes (DT), Cathode Strip Chambers (CSC) and Resistive Plate Chambers (RPC) (a more detailed description of the muon system is given in Section 4.3.4 and in [1]). The Level-1 muon trigger identifies muons, determines their transverse momenta and locations, and assigns the trigger data to the correct bunch crossing.

The muon candidates identified by the Level-1 muon trigger are used as seeds for the Level 2 muon reconstruction. The Level-2 candidates are used as input for Level-3.

The requirements which an event must fulfill to be triggered as di-muon event by the different trigger levels are, with respect to the low luminosity scenario:

- Level-1 [19]
  Two identified muons are required which have a well measured $|p_T| > 3$ GeV and

$|\eta| < 2.1$ (the start-up scenario has been implemented in ORCA for the Level-1 trigger).

- HLT [27]
  - Level-2
    The reconstructed tracks in the muon system need to have a valid extrapolation to the collision vertex. Required are also at least one reconstructed DT track segment in the barrel region and the sum of the numbers of DT track segments and RPC hits must exceed three. At least one muon should be isolated by calorimeter isolation (the isolation algorithms are described in Section 7.1.1).
  - Level-3
    Required are more than five silicon hits in total from the pixels and silicon strips in the inner tracking system. At least one muon should be isolated by tracker and pixel isolation (definition in Section 7.1.1). Two muons should be reconstructed which originate from the same vertex in z (± 5 mm), and are separated by $\Delta\phi > 0.05$, $|\Delta\eta| > 0.01$ and $\Delta p_T > 0.1$ GeV.

  The two muons should also have $|p_T| > 7$ GeV and $|\eta| < 2.4$.

This analysis uses the information if an event is accepted or not by the Level-1 Di-Muon trigger and by the High-Level Di-Muon trigger.

7.1.1 Muon Isolation

Three different isolation techniques are used in the HLT: Calorimeter Isolation, Pixel Isolation and Tracker Isolation. All three techniques are based on the measurement of the momentum or energy deposited in two cones around the reconstructed muon track, see Figure 7.1. The deposited energy is the transverse energy measured inside the calorimeter, for the Calorimeter Isolation, or the sum of the transverse momenta measured by the pixel detector, for the Pixel Isolation, or the sum of the transverse momenta of a Level-3 muon, for the Tracker Isolation.
The cones are defined by the maximum value of $\Delta R = \sqrt{(\Delta\eta)^2 + (\Delta\phi)^2}$. $\Delta\eta$ and $\Delta\phi$ are the distances from the muon direction in η and ϕ. The radius of the inner cone is ΔR_i, the radius of the outer cone is ΔR_a. The cone axes are defined by the muon direction at the vertex.
The inner cone, also called veto cone, should contain most of the energy deposited by the muon itself. The definition of the veto cone is an inherent process of the different isolation techniques. The energy deposited in the veto cone, called veto value, is subtracted from the energy deposited in the outer cone. The remaining energy should be close to zero if the muon is isolated. In order to decide if a muon is isolated, a threshold for the remaining energy and a cone size is defined. The used combination of these values is obtained by maximising the rejection of $b\bar{b} \to \mu X$ events ("reference background") and keeping the efficiency for $W \to \mu\nu$ events ("reference signal") at $\geq 97\%$. Further information on the isolation algorithm can be found in [1].

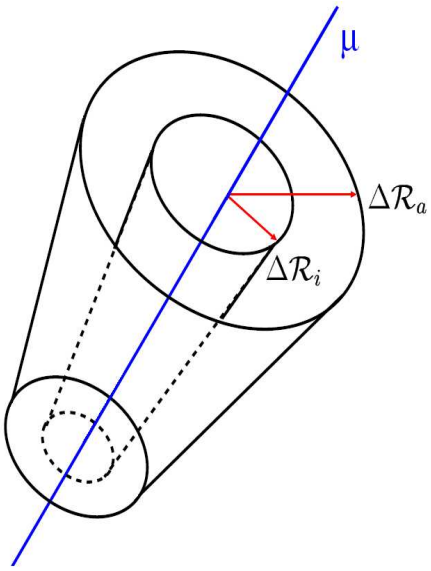

Figure 7.1: Schematic illustration of the isolation cones. The muon direction at the vertex defines the cone axes. The energy deposit $(\sum p_T, \sum E_T)$ in the outer cone, with the radius ΔR_a, is computed, and the contribution of the muon itself is removed by excluding the veto cone, with the radius ΔR_i [48].

7.1.2 Performance

Due to the pre-selection requirements (4 muons with $p_T > 3$ GeV and $|\eta| < 2.4$) the Level-1 Trigger efficiency is $> 99\%$ for signal and background. As the signal events contain four isolated high p_T muons good trigger efficiencies are expected. If more than two muons have a momentum higher than 7 GeV, the momentum requirement of the HLT will be fulfilled. Figure 7.2 shows the distribution of the second highest transverse muon momentum in one event before the trigger selection has been applied. The distribution is shown for all background samples and for the signal sample $m_{H^{\pm\pm}} = 200$ GeV which provides the lowest transverse muon momenta of all studied signal samples (see chapter 6). It can be seen easily that a cut which requires two muons with a transverse momenta > 7 GeV reduces a much higher amount of background events than of signal events.

The efficiency for a reconstructed event to be triggered by the Level-1 Di-Muon Trigger and by the High-Level Di-Muon Trigger after preselection is within uncertainties $> 99\%$ for the signal. The corresponding efficiencies for the background samples are shown in Table 7.1, it is 80% for the $ZZ \to 4\mu$ sample, with its isolated relatively high p_T muons, and $\sim 70\%$ for the other background samples.

	$Z\bar{Z} \to 4\mu$	$Z\bar{Z} \to 2\mu 2\tau$	$Z\bar{b}b \to 4\mu$	$t\bar{t} \to 4\mu$
L1+HLT efficiency [%]	79.8 ± 0.3	68 ± 1	67.3 ± 0.3	64.6 ± 0.4

Table 7.1: Level-1 (L1) plus High-Level Trigger (HLT) efficiency for all background processes, errors are statistical only.

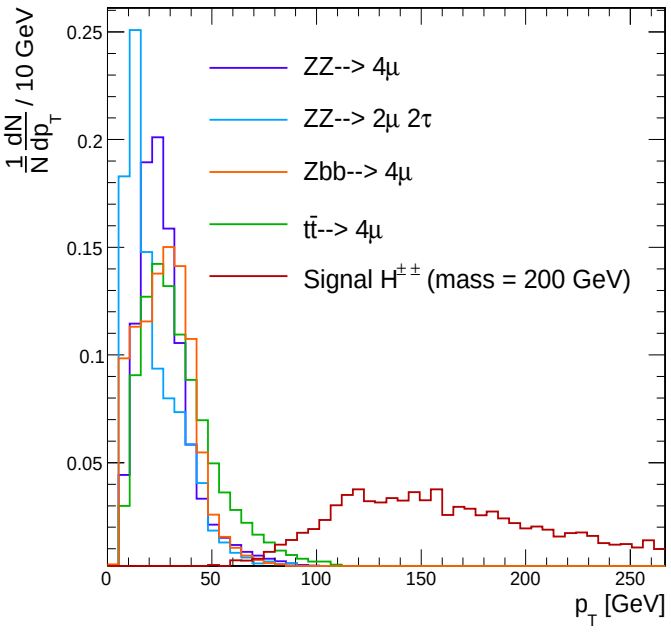

Figure 7.2: Distribution of the reconstructed second highest transverse muon momentum for all background samples and for the signal sample $m_{H^{\pm\pm}} = 200$ GeV, without online selection applied. The number of entries is normalized to one.

7.2 Offline Reconstruction

The reconstruction algorithm used in this analysis is the so called global muon reconstructor. The global muon reconstuctor is based on the standalone muon reconstructor, which uses information from the local muon reconstructor as seed.

Local Muon Reconstructor

The local muon reconstructor reconstructs muon track segments inside the muon system, using hits measured with the different gaseous detectors in the muon system.

Standalone Muon Reconstructor

These track segments are taken as seeds for the standalone muon reconstructor. The seeds define a region of interest used for further reconstruction. The standalone muon reconstructor combines the reconstructed track segments of the local muon reconstructor with information from the resistive plate chambers to form a complete track through the muon system, using the Kalman filter technique [1]. This track is extrapolated towards the beamline.

Global Muon Reconstructor

The global muon reconstructor combines the reconstructed tracks of the standalone muon reconstructor with hits measured by the silicon tracker and the pixel detector. Muon energy loss in the material and effects of multiple scattering are taken into account. A refit is done to find the best track by matching the information from muon system and tracker system [1].

7.2.1 Reconstruction Performance

Figure 7.3 shows the distance in $\Delta R = \sqrt{(\Delta\eta)^2 + (\Delta\phi)^2}$ between reconstructed and generated muons, for the signal sample with doubly charged Higgs boson mass of $m_{H^{\pm\pm}} = 200$ GeV.
The distance between generated muons and the corresponding reconstructed muons peaks very narrow at zero. For the signal sample with $m_{H^{\pm\pm}} = 200$ GeV the distance is $\Delta R < 0.9$ $m$rad for 99% of the muons. In the following studies about the reconstruction performance it is assumed that, if the distance between a reconstructed and a generated muon is smaller than 0.9 $m$rad, these muons are the same.
If two reconstructed muons have a distance smaller than 0.9 $m$rad to one generated muon, the reconstructed muon with the smallest distance is assumed to be the same muon as the generated muon.

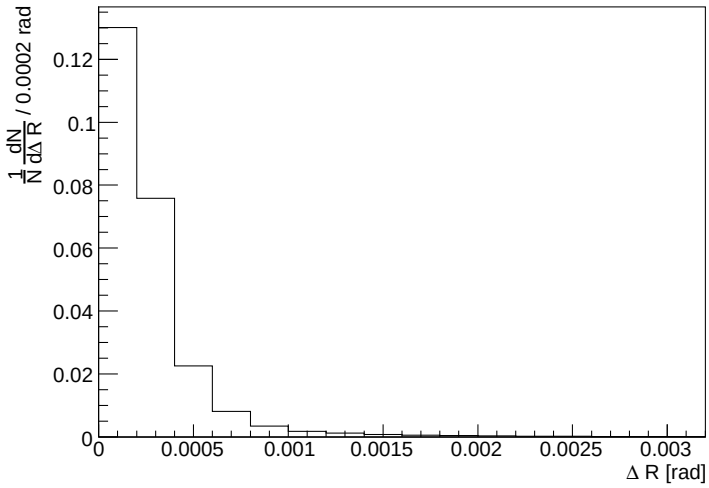

Figure 7.3: $\Delta R = \sqrt{(\Delta\eta)^2 + (\Delta\phi)^2}$ between generated and reconstructed muons of the signal sample $m_{H^{\pm\pm}} = 200$ GeV.

Figure 7.4 shows the reconstruction efficiency for muons as a function of η for the signal data sample $m_{H^{\pm\pm}} = 300$ GeV. The efficiency drops at the borders of the detector wheels, nevertheless it is always $\geq 87\%$ in the region $|\eta| < 1.8$.

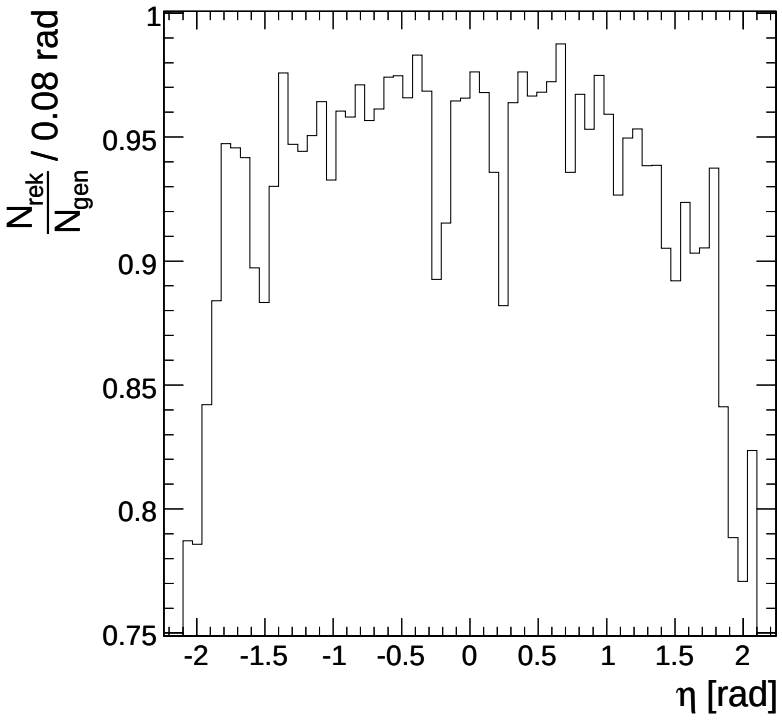

Figure 7.4: Reconstruction efficiency for muons as a function of η.

Muon Momentum Resolution

The transverse muon momentum resolution $\frac{\Delta p_T}{p_T}$ (Section 4.3.4) can be transformed into $\frac{\Delta(1/p_T)}{1/p_T}$. $1/p_T$ is proportional to the sagitta s. The statistical fluctuations of sagitta measurements, and therefore also of $1/p_T$ measurements, follow approximately a gaussian distribution. The uncertainty $\Delta(1/p_T)$ equals the width $\sigma(1/p_T)$ of the corresponding gaussian distribution. Thus the transverse momentum resolution can be expressed by the quantity $\sigma\left(\frac{1}{p_T^{rec}} - \frac{1}{p_T^{gen}}\right) \times p_T^{gen}$. Where p_T^{rec} and p_T^{gen} are respectively the generated transverse momenta and the reconstructed transverse momenta of the muons. $\sigma\left(\frac{1}{p_T^{rec}} - \frac{1}{p_T^{gen}}\right)$ denotes the gaussian width of the distribution $\left(\frac{1}{p_T^{rec}} - \frac{1}{p_T^{gen}}\right)$. Figure 7.5 and Figure 7.6 show the transverse momentum resolution as a function of p_T^{gen} for muons reconstructed in the barrel region $|\eta| < 0.2$ and muons reconstructed in the endcap region $0.8 < |\eta| < 1.2$, respectively. The generated and reconstructed muons of all signal samples have been used, to minimize statistical fluctuations. Figures 7.5 and Figure 7.6 can be compared to the plots in Figure 4.13 in Section 4.3.4 which show the same distributions for an official muon sample. All plots show the same almost flat part of the distribution for p_T^{gen} smaller than ~ 100 GeV. The momentum resolution of the muon system for low p_T muons is limited by multiple scattering and the best momentum resolution is given by the tracker. For muons with $p_T > 100$ GeV, the spatial resolution of the muon chambers starts to dominate the distribution.

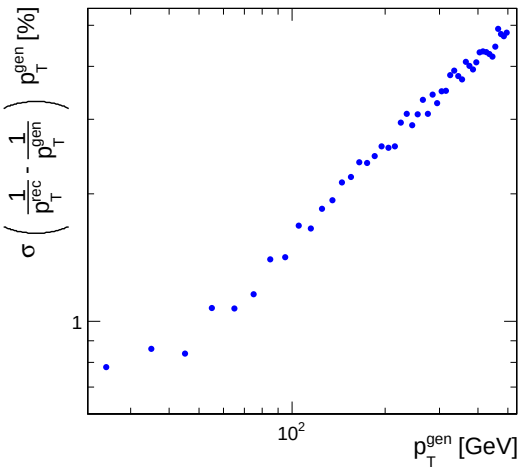

Figure 7.5: Transverse momentum resolution for all reconstructed muons in the signal samples with $|\eta| < 0.2$.

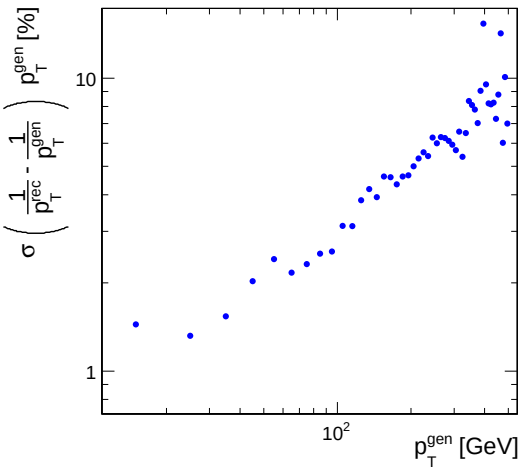

Figure 7.6: Transverse momentum resolution for all reconstructed muons in the signal samples with $0.8 < |\eta| < 1.2$.

Reconstructed $H^{\pm\pm}$

Figure 7.7 shows the invariant reconstructed Higgs boson mass $m(\mu^{\pm}\mu^{\pm})$ (the invariant mass of the Higgs boson is reconstructed by calculating the invariant mass of the two equally charged muons with the largest transverse momentum, as descibed in Section 6.3) for two example signal masses and for the four background data samples. For the two signal samples the invariant mass distribution is shown before and after the full detector simulation. The invariant mass distributions of the backgound samples have been added up. All distributions are scaled to an integrated luminosity of 10 fb^{-1}. The integral of the distribution at generator level is larger than the integral after the detector level, as not all muons are reconstructed, see Figure 7.4. The smearing of the invariant mass distribution due to detector effects is much worse for the signal sample $m_{H^{\pm\pm}} = 600$ GeV than for the signal sample $m_{H^{\pm\pm}} = 200$ GeV. This can be attributed to the worsening of the detector resolution for high doubly charged Higgs boson masses. It can be explained by the worsening of the muon p_T resolution with increasing p_T, see Figures 7.5 and 7.6. Increasing doubly charged Higgs Boson mass is correlated to increasing muon p_T.

The detector resolution σ_{det} for the reconstructed doubly charged Higgs boson mass has been estimated by:

$$\sigma_{rec}^2 = \sigma_{gen}^2 + \sigma_{det}^2 \quad \Rightarrow \quad \sigma_{det} = \sqrt{\sigma_{rec}^2 - \sigma_{gen}^2}, \tag{7.1}$$

where σ_{rec} and σ_{gen} are the widths of the mass distributions, using once generated muons and once reconstructed muons. The reconstruction technique is explained in detail in Section 6.3. It has been assumed that the reconstructed Higgs boson mass distributions are gaussian. σ_{gen} is determined by the width of the Breit-Wigner distribution and radiative corrections. It ranges from ~ 4.5 GeV at $m_{H^{\pm\pm}} = 200$ GeV to ~ 5.5 GeV at $m_{H^{\pm\pm}} = 800$ GeV. Figure 7.8 shows σ_{det} as a function of the doubly charged Higgs boson mass. All

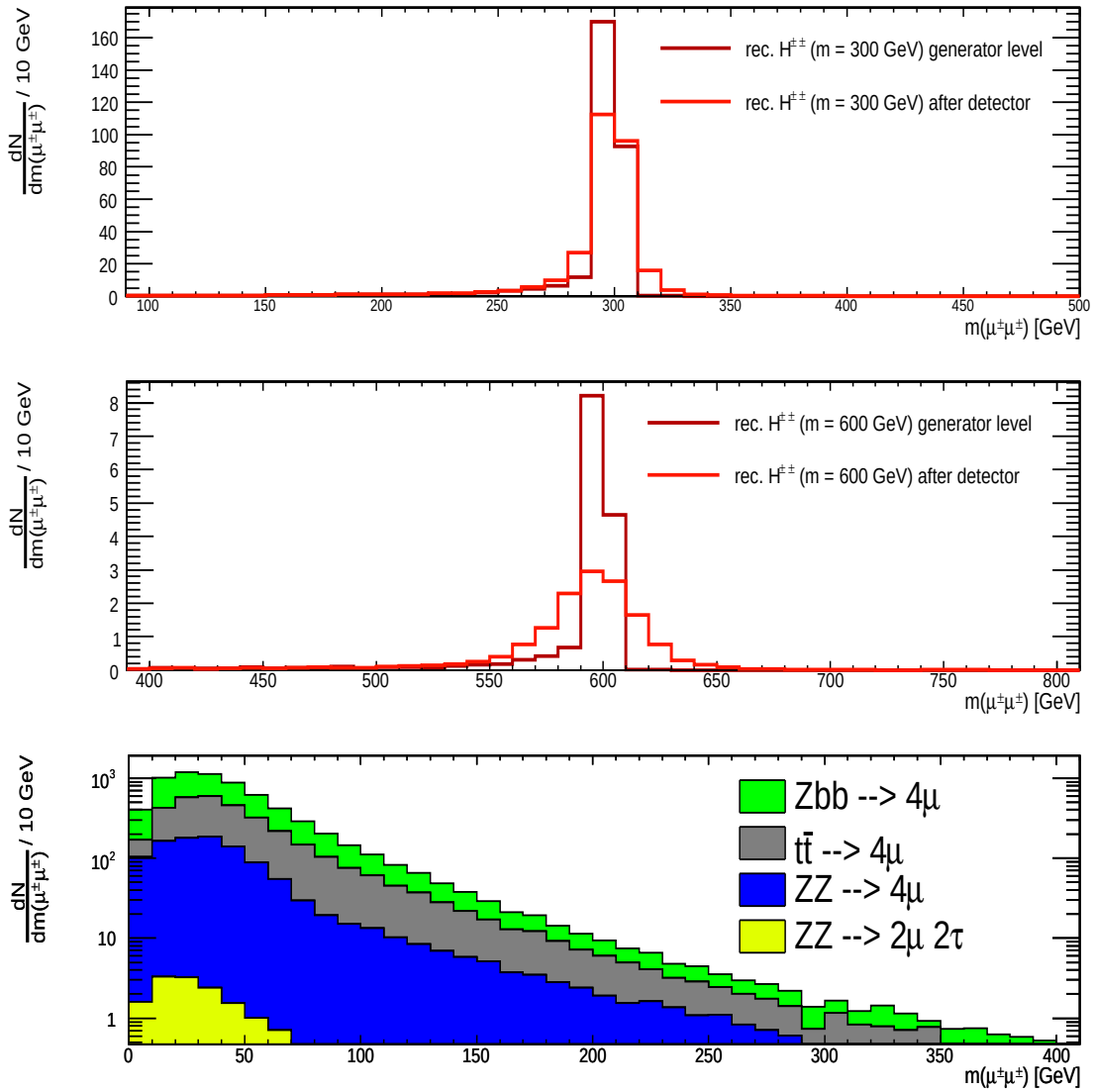

Figure 7.7: The invariant mass distribution of the signal sample $m_{H^{\pm\pm}} = 300$ GeV and of the signal sample $m_{H^{\pm\pm}} = 600$ GeV before and after the detector simulation and the invariant mass distribution of the four backgrounds after the detector simulation. The event numbers have been normalized to an integrated luminosity of 10 fb^{-1}.

signal samples have been used, in order to minimize statistical fluctuations. σ_{det} is almost proportional to the doubly charged Higgs boson mass. A straight line with the following parameters and errors:

$$\sigma_{det} = \left(-3.4(\pm 0.9) + 0.040(\pm 0.001) \cdot \frac{m_{H^{\pm\pm}}}{\text{GeV}}\right) \text{ GeV}, \tag{7.2}$$

can be fitted to the distribution. The measured detector resolution determines the accuracy which can be achieved for the reconstruction of doubly charged Higgs boson masses. It depends on the resolution of the muon energy and transverse momentum.

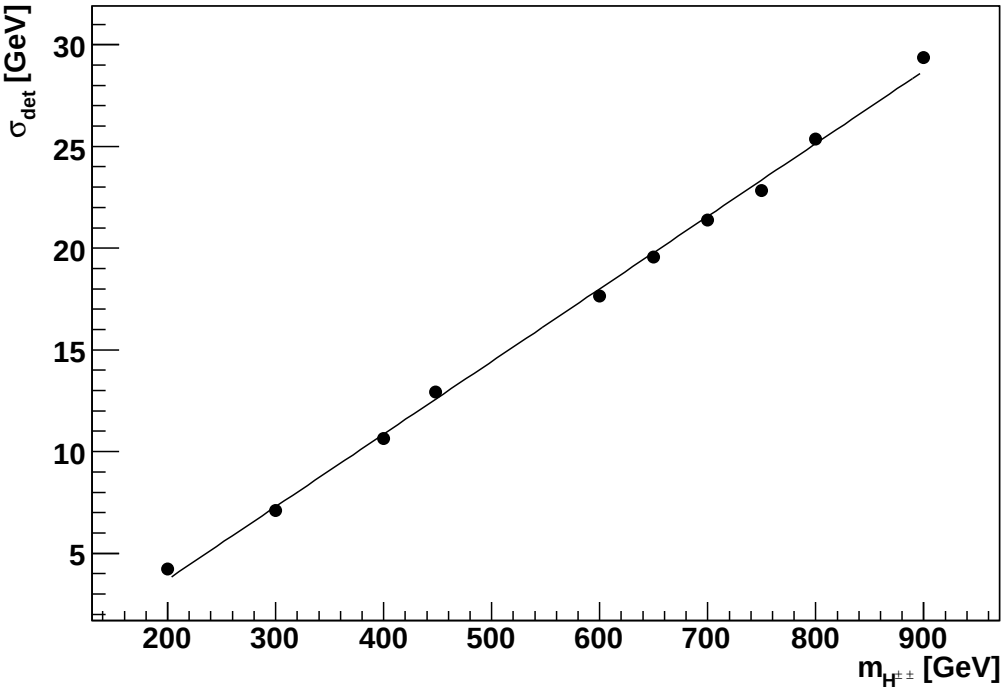

Figure 7.8: Mass resolution σ_{det} as a function of $m_{H^{\pm\pm}}$.

Chapter 8

Final Event Selection

Very few cuts have been used in this study in order to keep the signal efficiency as high as possible. Due to the decay in equally charged muons the reconstructed invariant mass peak of the signal can be clearly distinguished from the background distribution, even before the final selection. The following offline event selection cuts have been applied:

8.1 Cut on the Number of Reconstructed Muons

The first step in the offline event selection is to require four reconstructed muons with $p_T > 8$ GeV in $|\eta| < 2.1$. The requirements on η and p_T are direct consequences of the η and p_T thresholds of the Di-Muon trigger (see chapter 7.1).

Figure 8.1 shows the number of triggered and reconstructed muons per event, for all background samples and for the $m_{H^{\pm\pm}} = 200$ GeV signal. Since only events with more than four muons are chosen, especially the number of $Z\bar{b}b$ background events is reduced strongly.

The efficiency of the selection cut, for events which passed the HLT selection, is shown in Table 8.1 for the background data samples. It is much larger for signal events, e.g. the sample $m_{H^{\pm\pm}} = 300$ GeV has an efficiency of $76 \pm 1\%$. This cut diminishes significantly the amount of background.

	$ZZ \to 4\mu$	$ZZ \to 2\mu 2\tau$	$Z\bar{b}b \to 4\mu$	$t\bar{t} \to 4\mu$
4μ reconstruction efficiency [%]	26.5 ± 0.2	22.6 ± 0.6	12.9 ± 0.1	30.2 ± 0.3

Table 8.1: Efficiency of selecting an event with four reconstructed muons with $p_T > 8$ GeV in $|\eta| < 2.1$ for the background samples, errors are statistical only.

8.2 Impact Point Cut

Events with muons from different collisions, i.e. two or three muons from one collision and one or two from another, may become a significant source of background because of

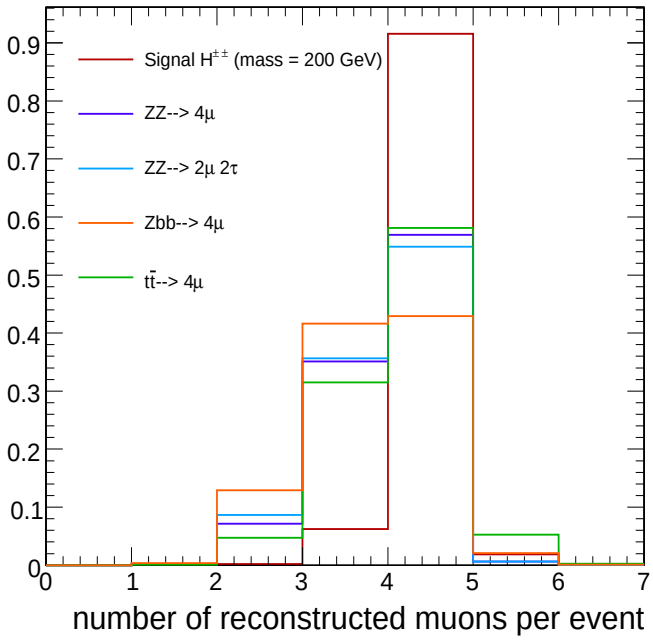

Figure 8.1: Number of reconstructed muons per event, the total number of entries is normalized to one.

the much higher rates compared to genuine 4μ processes. To suppress this background a vertex cut is applied.
For each muon in an event the Impact Point is determined. The Impact Point can be found by extrapolating the reconstructed muon trajectory towards the beamline. The point of closest approach to the origin of the detector coordinate system is defined as Impact Point [49].

The longitudinal distances $|\Delta z|$ between the Impact Points of all muons are calculated for each event. The largest $|\Delta z|$ is required to be smaller than 0.05 cm.
Figure 8.2 shows the distribution of the largest distance $|\Delta z|$ between muons generated in the decay of doubly charged Higgs bosons for the signal sample $m_{H^{\pm\pm}} = 200$ GeV. For $\leq 99.6\%$ of the events is $|\Delta z| < 0.05$ cm.
The width of this distribution is much smaller than the width of the z distribution for the Impact Points of all muons in the same sample. This distribution is plotted in Figure 8.3. The gaussian width of the z distribution is 5.3 ± 0.1 cm and it corresponds to the longitudinal size of the interaction region of the LHC beam of about 5 cm.
Assuming a flat distribution of z over a width of 5 cm the largest distance $|\Delta z|$ between different collision vertices is, with a probability $> 99\%$, larger than 0.05 cm. The efficiency of this cut, for signal data samples with included pile-up, is $\approx 96\%$ as can be seen in Table 8.3. This cut also reduces the $Z\bar{b}b$ and the $t\bar{t}$ background by roughly a factor two (see Table 8.2), due to the displaced vertices of the muons generated in b decays.

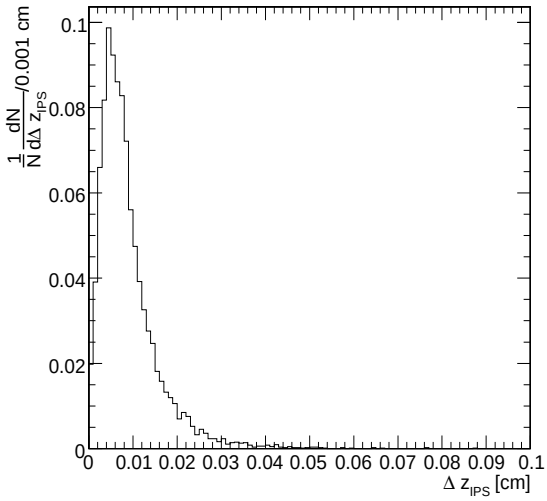

Figure 8.2: Distribution of the largest Δz between muons generated in the decay of doubly charged Higgs Bosons for $L = 10fb^{-1}$ and $m_{H^{\pm\pm}} = 200$ GeV.

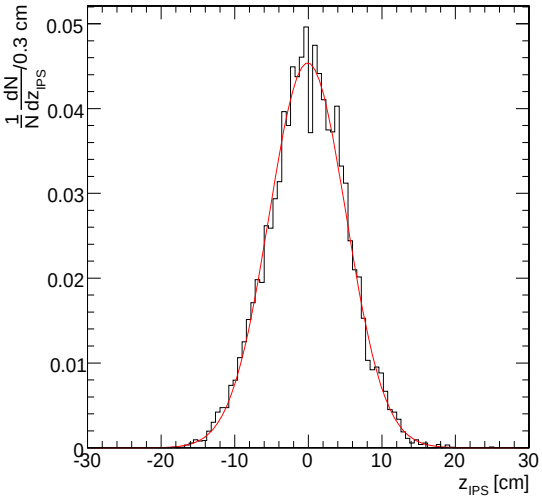

Figure 8.3: Distribution of z of all muons, generated for $L = 10fb^{-1}$ and $m_{H^{\pm\pm}} = 200$ GeV. A Gaussian curve is fitted to the distribution.

8.3 Results

Table 8.2 and Table 8.3 show the NLO cross sections times efficiency after each of the selection cuts described in the last sections. These values are shown for each background sample in Table 8.2 and for the signal samples with doubly charged Higgs masses of 300, 600 and 800 GeV in Table 8.3.

	$t\bar{t}$	$Z\bar{b}b$	$ZZ \to 4\mu$	$ZZ \to 2\mu 2\tau$
Production cross section(NLO) [fb]	$53 \cdot 10^3$	$278 \cdot 10^3$	153	212
Preselection [fb]	232 ± 1	290 ± 1	87.4 ± 0.3	1.63 ± 0.02
Level-1 Trigger [fb]	232 ± 1	289 ± 1	87.3 ± 0.3	1.63 ± 0.02
High Level Trigger [fb]	149 ± 1	195 ± 1	69.7 ± 0.3	1.10 ± 0.01
4 μ reconstructed ($p_T > 8$ GeV, $\|\eta\| < 2.1$) [fb]	45.1 ± 0.4	25.1 ± 0.3	18.5 ± 0.1	0.25 ± 0.01
Impact Point Cut [fb]	22.8 ± 0.3	13.1 ± 0.2	16.9 ± 0.1	0.22 ± 0.01

Table 8.2: The NLO cross sections for background events with forced decay modes after each stage of the event selection. Errors are statistical only.

Figure 8.4 shows the invariant mass of the reconstructed doubly charged Higgs bosons before and after the final selection for signal events ($m_{H^{\pm\pm}} = 300$ GeV and $m_{H^{\pm\pm}} = 600$ GeV).

The chosen bin size is 20 GeV, this bin size is comparable to the detector resolution of the doubly charged Higgs Boson mass σ_{det} for $m_{H^{\pm\pm}} = 600$ GeV (Section 7.2.1).

$H^{\pm\pm}$ mass	300 GeV	600 GeV	800 GeV
Production cross section(NLO) [fb]	19.6	0.909	0.201
Preselection [fb]	17.4± 0.3	0.85 ± 0.02	0.190 ± 0.004
Level-1 Trigger [fb]	17.3 ± 0.3	0.85 ± 0.02	0.190 ± 0.004
High Level Trigger [fb]	17.1 ± 0.3	0.83 ± 0.02	0.188 ± 0.004
4 μ reconstructed ($p_T > 8$ GeV, $\|\eta\| < 2.1$) [fb]	13.0 ± 0.2	0.70 ± 0.02	0.158 ± 0.003
Impact Point Cut [fb]	12.5 ± 0.2	0.67 ± 0.02	0.153 ± 0.003

Table 8.3: Production cross sections (NLO) for signal events with $m_{H^{++}} = 300$, 600, 800 GeV and forced decay into four muons after each stage of the event selection. Errors are statistical only.

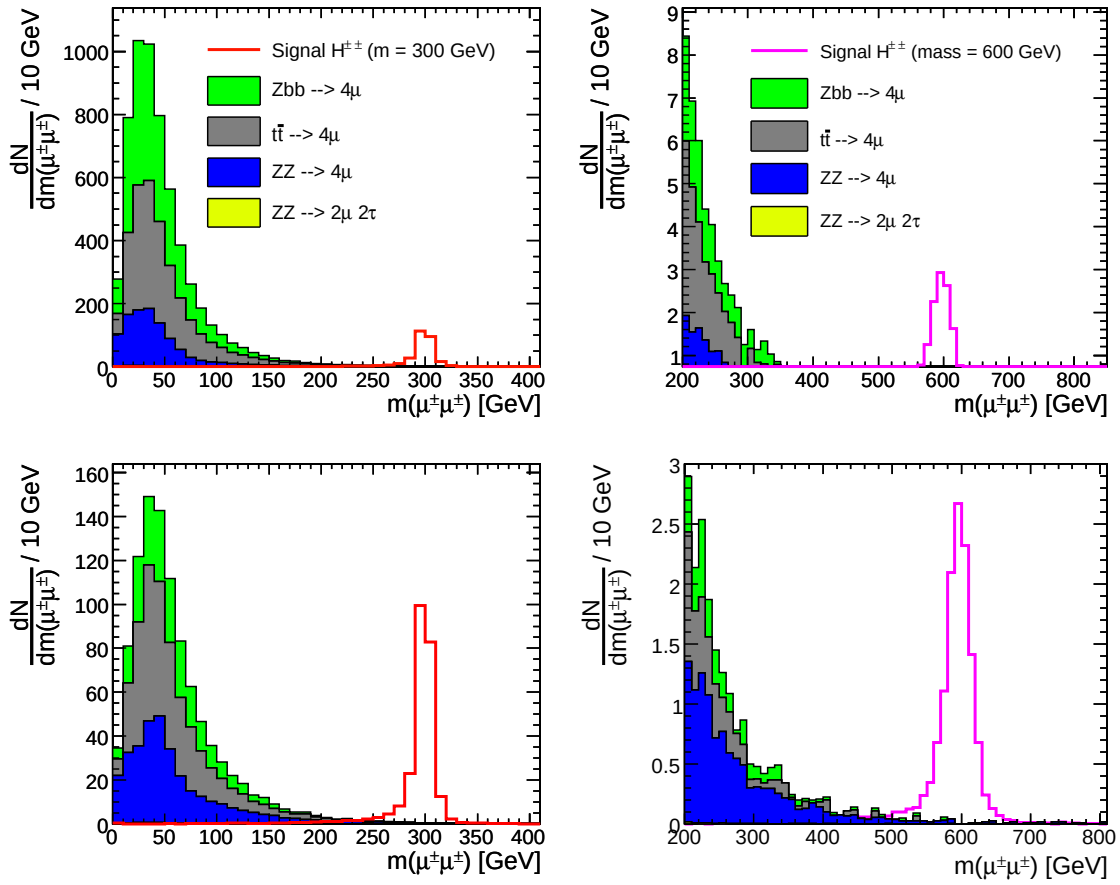

Figure 8.4: Reconstructed invariant mass of $H^{\pm\pm}$ candidates, (top) after trigger selection, (bottom) after final selection. The total number of events is normalized to 10 fb^{-1}.

Even before the final selection, the Higgs mass is clearly distinguishable from the background. Nevertheless, loosening the offline requirements of this selection, in order to improve the signal efficiency, would not make any sense. The signal efficiency is mostly effected by requiring the presence of four reconstructed muons. If only three or two muons were required instead, all processes in which only two or three muons are produced would become additional backgrounds. This would reduce the signal significance.

Chapter 9

$b\bar{b}$ Background

Events generated in strong interactions, so called QCD events, are a huge problem for many signal processes at the LHC, due to their relatively large cross section. The signal processes studied in this thesis have cross sections of a few fb at the LHC while the pair production of b quarks for example has a cross section of about a few μb.

9.1 Background at Generator level

The pair production of b quarks, in the following called $b\bar{b}$ background, provides the QCD events with the highest probability of faking signal events with multiple muons in the final state. Two important Feynman diagrams for the pair production of b are shown in Figure 9.1 and Figure 9.2. The $b\bar{b}$ background is generated in several sub-samples using PYTHIA

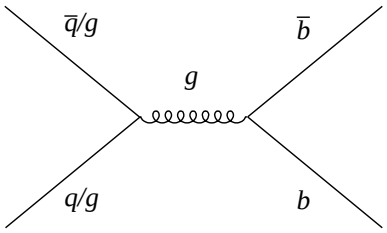

Figure 9.1: s-channel Feynman diagram for the production processes: $q\bar{q} \rightarrow b\bar{b}$ and $gg \rightarrow b\bar{b}$.

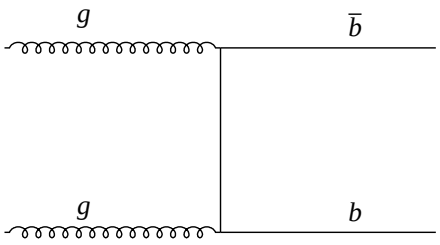

Figure 9.2: t-channel Feynman diagram for the production process: $gg \rightarrow b\bar{b}$.

with CMKIN_1_0_2. Each sub-sample requires two b jets in the region $|\eta| < 2.4$ within a certain $\hat{p}_T$ range. $\hat{p}_T$ is the transverse momentum of the final state partons in the total rest frame of the hard scattering process. The sub-samples are distinguished by their different $\hat{p}_T$ ranges, and have been reconstructed and analysed separately. Table 9.1 shows the different $b\bar{b}$ samples with their $\hat{p}_T$ ranges and the integrated luminosity corresponding to the number of simulated $b\bar{b}$ events for each sample [50]. It can be seen, that the integrated

luminosity corresponding to the number of generated events is much lower than 10 fb^{-1}, which is the integrated luminosity expected after the first year of data-taking at the CMS detector. This discrepancy illustrates the main problem of $b\bar{b}$ background studies, the amount of simulated events is not sufficient.

Official sample	$\hat{p}_T$ region [GeV]	integrated luminosity corresponding to the number of generated events [fb^{-1}]
bt03_b_pt30-50	$30 < \hat{p}_T < 50$	$39.4 \cdot 10^{-6}$
bt03_b_pt50-80	$50 < \hat{p}_T < 80$	$187.1 \cdot 10^{-6}$
bt03_b_pt80-120	$80 < \hat{p}_T < 120$	$1.4 \cdot 10^{-3}$
bt03_b_pt120-170	$120 < \hat{p}_T < 170$	$10.2 \cdot 10^{-3}$
bt03_b_pt170up	$\hat{p}_T > 170$	$49.6 \cdot 10^{-3}$

Table 9.1: The different $b\bar{b}$ samples

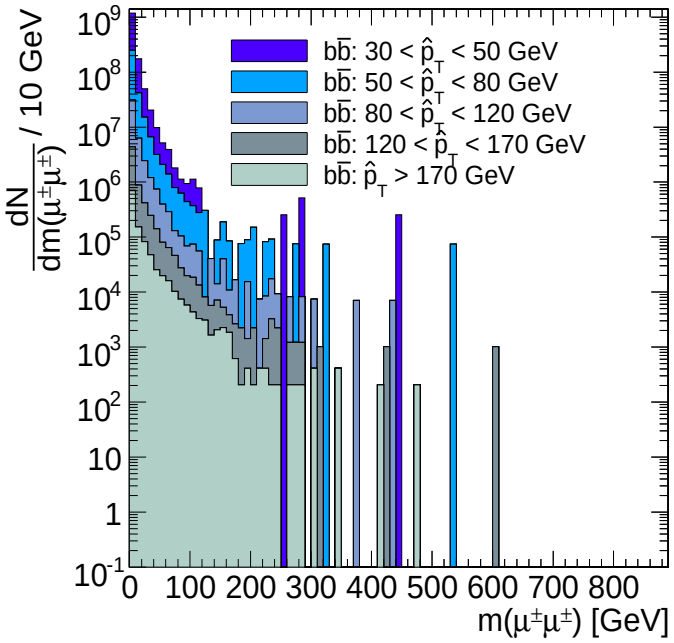

Figure 9.3: Distribution of the reconstructed invariant mass of $H^{\pm\pm}$ candidates for all $b\bar{b}$ samples, at generator level. The number of entries of the different samples have been stacked. The total number of events is scaled to an integrated luminosity of 10 fb^{-1}.

Figure 9.3 shows the reconstructed invariant mass of $H^{\pm\pm}$ candidates, at generator level. The different $b\bar{b}$ samples have been added up. Due to the lack of simulated $b\bar{b}$ background events, the number of generated events has to be multiplied by a factor much larger than one, to be scaled up to an integrated luminosity of 10 fb^{-1}.
Beyond an invariant mass of roughly 300 GeV, nearly no background events have been simulated. The amount of background in this region can be estimated by fitting an exponentially decreasing curve to the distribution. This method is based on the physical assumption, that a mass distribution reconstructed from decay products of a non-resonant state typically follows, at least locally, an exponentially decreasing curve.

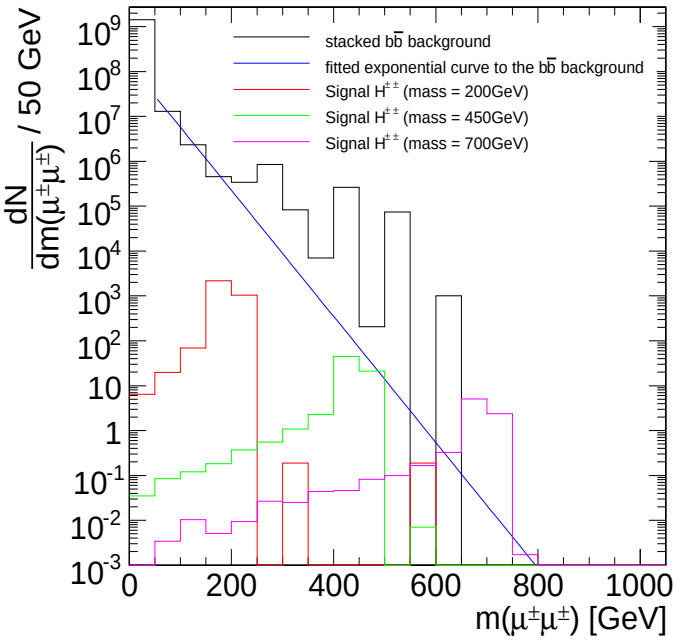

Figure 9.4: Distribution of the reconstructed invariant mass of $H^{\pm\pm}$ candidates for all $b\bar{b}$ samples, at generator level. An exponentially decreasing curve is fitted to the stacked background. The invariant mass distribution for three signal samples with $m(H^{\pm\pm}) = 200$ GeV, 450 GeV, 700 GeV, is also shown. The number of events is scaled to an integrated luminosity of 10 fb^{-1}.

Figure 9.4 shows a possible fit of an exponential curve to the background distribution, for invariant masses greater than 50 GeV. This method of estimating the $b\bar{b}$ background is very dependent on the mass region chosen for the fit. The resulting curve is therefore only used as a rough estimate. The parameters of the curve and the errors of the fit are:

$$\frac{dN}{d(m(\mu^{\pm}\mu^{\pm}))}/50\ \text{GeV} = \exp\left[18.8(\pm 1\cdot 10^{-3}) - 0.03(\pm 1\cdot 10^{-5})\cdot\frac{m(\mu^{\pm}\mu^{\pm})}{\text{GeV}}\right], \qquad (9.1)$$

where $m(\mu^{\pm}\mu^{\pm})$ is the reconstructed invariant mass of the $H^{\pm\pm}$ candidates, in GeV. Before any selection cut has been applied, the $b\bar{b}$ background is a major background to the studied signal processes.

9.2 Online Selection

The online selection removes nearly all simulated $b\bar{b}$ events. Due to the facts, that:

- all muons generated in the decay chain of b quarks are low p_T muons, see figure 9.5,
- in most events less than two muons are reconstructed, see figure 9.6,
- the isolation algorithm of the muon High-Level trigger is optimized on rejecting the non-isolated muons from $b\bar{b}$ decays, see section 7.1.1.

After the HLT selection only one out of all simulated events remains. This event belongs to the sample: 80 GeV $< \hat{p}_T <$ 120 GeV and corresponds to a number of 7018 remaining

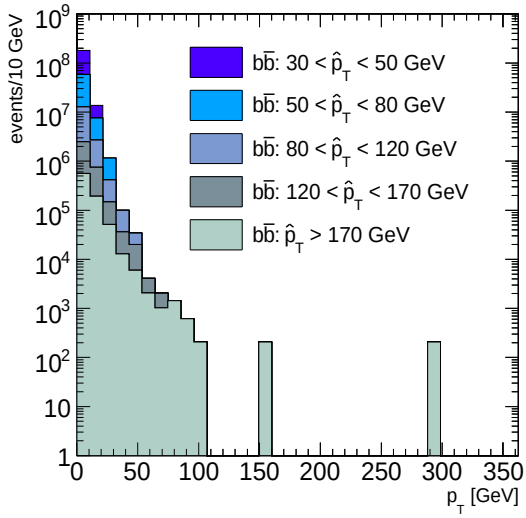

Figure 9.5: Distribution of the second highest reconstructed transverse muon momentum in one event, no trigger selection applied. The $b\bar{b}$ samples have been stacked, the number of events corresponds to an integrated luminosity of 10 fb^{-1}.

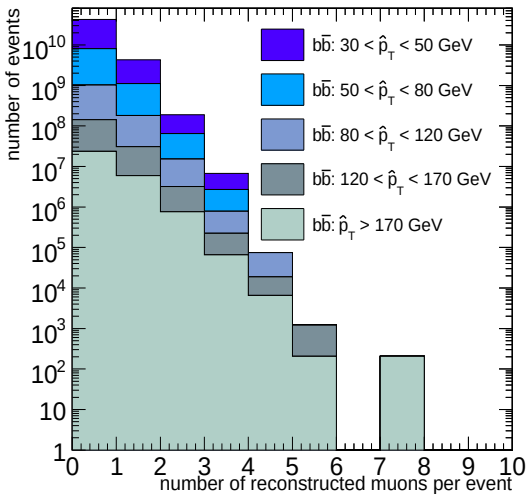

Figure 9.6: Distribution of the total number of reconstructed muons per event, no trigger selection applied. The $b\bar{b}$ samples have been stacked, the total number of events corresponds to an integrated luminosity of 10 fb^{-1}.

events at a luminosity of 10 fb^{-1}. With a total number of $\approx 4.7 \cdot 10^{10}$ expected events after reconstruction before the application of any selection cut, the trigger selection efficiency is $\leq 15 \cdot 10^{-10}\%$.

9.3 Final Selection

The cut on the number of reconstructed muons removes the last remaining simulated $b\bar{b}$ event. Due to the lack of simulated events, no sensible efficiency of this cut can be obtained. To estimate the rejection power of this cut, the cut is applied before the trigger selection. It is found that only $161 \cdot 10^{-6}\%$ of all events provide at least four reconstructed muons, see figure 9.6. Using this rejection factor on the remaining 7018 events (for 10 fb^{-1}) after the trigger selection, all but one event is rejected.
Thus the $b\bar{b}$ background can be savely neglected for this analysis.

Chapter 10

Statistical Interpretation

10.1 Statistical Interpretation

10.1.1 The CL_s Method

The final invariant mass spectrum, which is presented in chapter 8, has to be tested in a statistical manner to decide, up to which invariant $H^{\pm\pm}$ mass an existing signal can be discovered or a non-existing signal excluded. For this statistical investigation two hypothesises are tested using the CL_s-method [51–53]: the hypothesis that the generated invariant mass spectrum consists only of background events and the hypothesis that the generated invariant mass spectrum consists of signal plus background events. A statistical estimator is needed, which makes it possible to decide which of the two hypotheses fits best. The statistical estimator used in the CL_s-method is $Q = \prod_{i=1}^{N} Q_i$. Q_i is the likelihood ratio of the probability of finding n_i entries in a bin if the signal plus background hypothesis is true, to the probability of finding n_i entries if the background only hypothesis is true:

$$Q_i(m_{H^{\pm\pm}}) = \frac{P(\mu = s_i(m_{H^{\pm\pm}}) + b_i;\ n_i)}{P(\mu = b_i;\ n_i)}, \tag{10.1}$$

where s_i is the number of signal events in bin i and b_i is the number of background events in bin i. $P(\mu; n)$ is the probability of finding n events if μ are expected. Q_i is calculated for each bin i, of the generated invariant mass spectrum.

Assuming the number of entries in a certain bin to be Poisson distributed:

$$P(\mu; n) = \frac{\mu^n}{n!} \cdot e^{-\mu}, \tag{10.2}$$

the log-likelihood ratio $-2 \ln Q$ becomes:

$$-2 \ln Q(m_{H^{\pm\pm}}) = -2 \sum_{i=1}^{N} \left[n_i \ln \left(1 + \frac{s_i}{b_i} \right) - s_i \right] = 2 s_{tot} - 2 \sum_{i=1}^{N} n_i \ln \left(1 + \frac{s_i}{b_i} \right). \tag{10.3}$$

Figure 10.1 shows the distribution of $-2 \ln Q$ for various doubly charged Higgs boson masses for the background only hypothesis and for the signal plus background hypothesis.

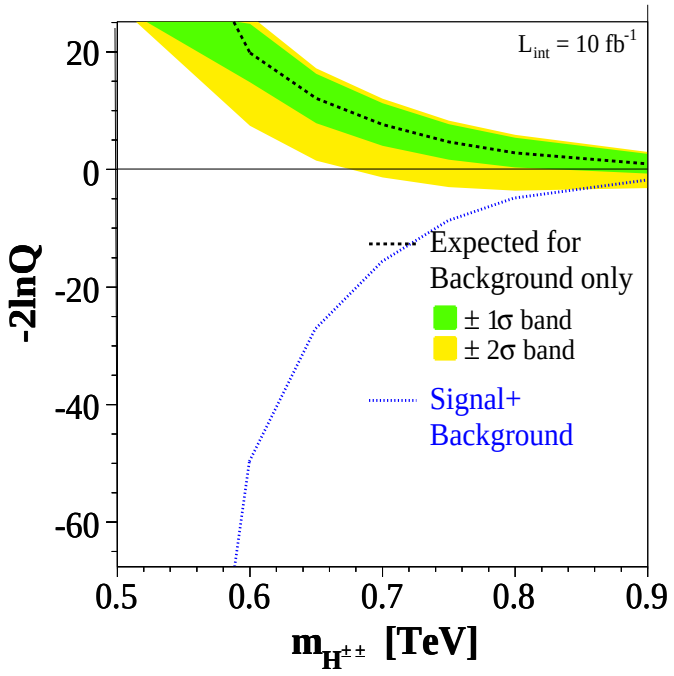

Figure 10.1: $-2\ln Q$ as a function of the doubly charged Higgs boson mass for the background only hypothesis and for the signal plus background hypothesis, errors are statistical only.

To determine the compatibility of a certain measured $-2\ln Q$ value with the signal plus background or with the background only hypothesis, $-2\ln Q$ is calculated for several "pseudo-experiments". For this "pseudo-experiments", the number of entries n_i in a certain bin are generated as Poisson distributed random numbers, once for the signal plus background hypothesis, with the mean value $\mu = s_i + b_i$, and once for the background only hypothesis with $\mu = b_i$.

As a result one obtains two almost Gaussian shaped distributions for each doubly charged Higgs boson mass. Figure 10.2 shows these two distributions, once for a low mass doubly charged Higgs boson and once for a high mass doubly charged Higgs boson. For a low doubly charged Higgs boson mass, the invariant mass spectrum of the signal can be clearly distinguished from the background. The $-2\ln Q$ distributions corresponding to the signal plus background and to the background only hypothesis are clearly separated and have nearly no overlap. With increasing doubly charged Higgs boson mass, the signal peak in the invariant mass spectrum gets smaller and becomes less distinguishable from the background. The two $-2\ln q$ distributions P_b and P_{s+b} show a significant overlap.

In the case of existing real data, the $-2\ln Q$ value of the measured data can be calculated and compared to the two integral-normalised distributions P_{s+b} and P_b. The confidence level for the compatibility of the measured data with the background only hypothesis (CL_b) and the confidence level for the compatibility of the measured data with the signal plus background hypothesis (CL_{s+b}) can be calculated by:

$$\mathrm{CL}_b = \int_{X_0}^{\infty} \mathcal{P}_b(x)dx \tag{10.4}$$

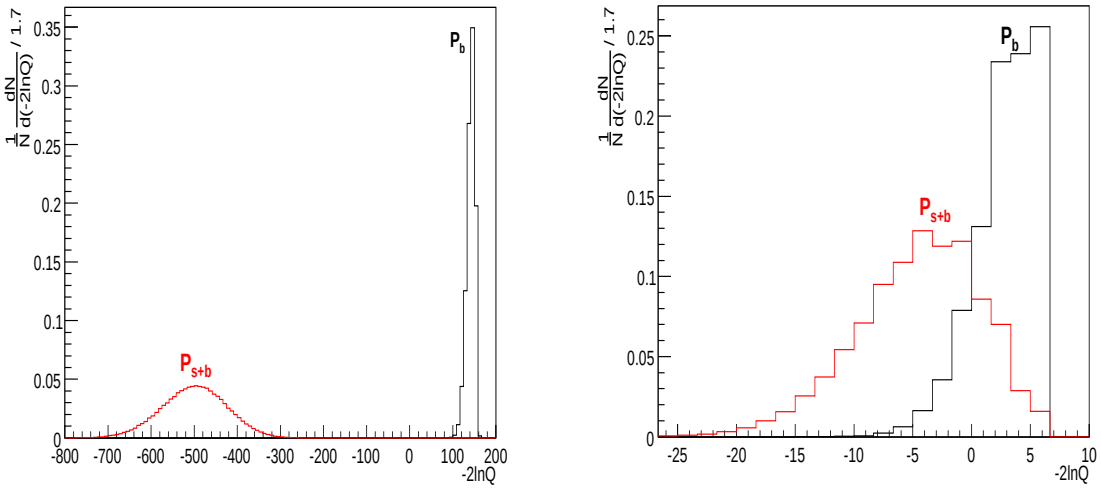

Figure 10.2: Distribution of the variable $-2\ln Q$ for the signal plus background hypothesis (P_{s+b}) and for the background only hypothesis (P_b). The distributions are normalized to one and shown for a signal mass of 400 GeV (left plot) and for a signal mass of 800 GeV (right plot).

$$\mathrm{CL}_{s+b} = \int_{X_0}^{\infty} \mathcal{P}_{s+b}(x)dx \tag{10.5}$$

The integration border X_0 is the $-2\ln Q$ value of the measured data.

For the analysis presented in this diploma thesis no real data exists. In this case, two probabilities can be determined:

- The probability, for the background only distribution to fake a signal. The confidence level corresponding to this probability is $1 - CL_b$, where the integration border X_0 is the mean value of the signal plus background distribution. If a signal will be detected, it can per convention only be claimed as discovery, if the probability for detecting a non-existing signal is smaller than 5σ.

$$1 - \mathrm{CL}_b \leq 2.85 \cdot 10^{-7}. \tag{10.6}$$

- The probability, for an existing signal to be undetected. The confidence level corresponding to this probability is CL_{s+b}, where the integration border X_0 is the mean value of the background only distribution. For low signal and background rates the use of the normalized $\mathrm{CL}_s := \frac{\mathrm{CL}_{s+b}}{\mathrm{CL}_b}$ instead of CL_{s+b} is more sensible, see [53]. If no signal will be detected, the existence of a signal can only be excluded with 95% confidence level if:

$$\mathrm{CL}_s := \frac{\mathrm{CL}_{s+b}}{\mathrm{CL}_b} < 0.05. \tag{10.7}$$

Both confidence levels CL_b and CL_{s+b} are marked in figure 10.3.

In order to calculate the statistical errors the distributions P_b and P_{s+b} are assumed to be Gaussian. The widths σ of P_b and P_{s+b} are determined. The integration borders X_0

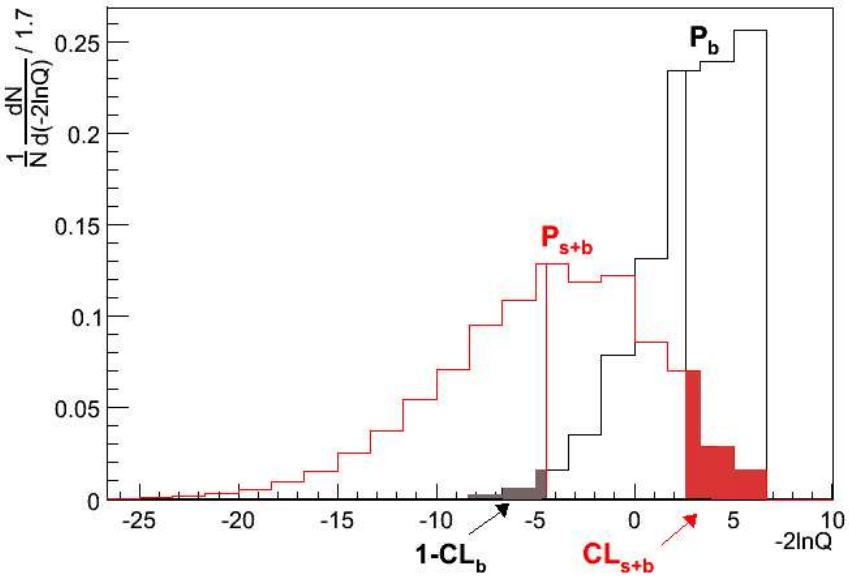

Figure 10.3: Distribution of the variable $-2\ln Q$ for signal plus background hypothesis P_{s+b} and for the background only hypothesis P_b. The distributions are shown for a signal mass of 800 GeV. The confidence levels $1 - \mathrm{CL}_b$ and CL_{s+b} are shown for the case that no real data exists. In this case the integration borders X_0 for CL_b and CL_{s+b} are the mean of the P_{s+b} distribution and the mean of the P_b distribution, respectively.

are changed by $\pm 1\sigma$ and $\pm 2\sigma$. The resulting changes in the confidence levels are taken as statistical errors.

10.1.2 Background Event Statistic

For invariant masses greater than $\sim$ 500 GeV, the unscaled number of simulated events which pass the final selection cuts is almost zero, as shown in Figure (10.4) and Figure (10.5). Nevertheless, zero simulated background events do not necessarily mean zero background events in reality. Two possibilities for estimating the background distribution in this region are:

1. The empty bins are filled, using Poisson statistics:
   The N bins in the invariant mass spectrum are assumed to be the result of N independent Poisson counting experiments. If a backgrounds has no entries in a certain bin, the mean of the corresponding Poisson distribution has, at 95% confidence level, to be ≤ 3 events. To stay conservative the bin is filled with 3 background events which are multiplied by the corresponding scale factor. The scale factor enlargens the total number of generated events to the number of events expected for the studied integrated luminosity. This procedure is repeated for each background. In this method it is therefore assumed, that independent of the actual amount of generated background events the real background distribution is not described accordingly by the simulated distribution. Especially for background samples like $ZZ \to 2\tau 2\mu$, where a large percentage of the generated events is reduced by selection cuts, zero events after

the selection cuts might really correspond to zero events in reality. The described method would therefore seriously overestimate the amount of expected events for this background sample.
This method of estimating the amount of background events is valid and compatible with Poisson statistics but rather conservative. Figure 10.4 shows the invariant mass spectrum before and after the bins have been filled.

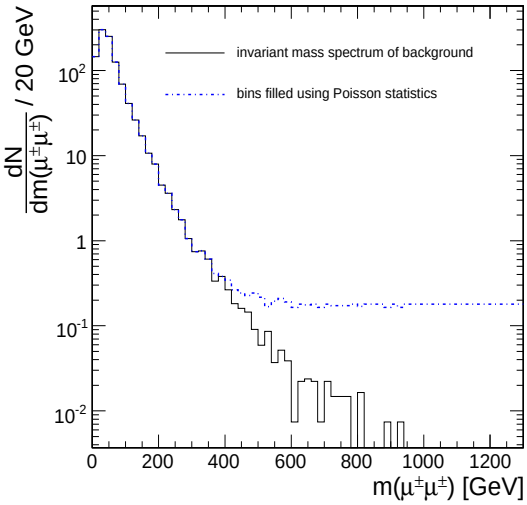

Figure 10.4: Distribution of the invariant reconstructed $H^{\pm\pm}$ mass for all background events, at an integrated luminosity of 10 fb^{-1}, before and after the empty bins have been filled with upper limits from Poisson statistics.

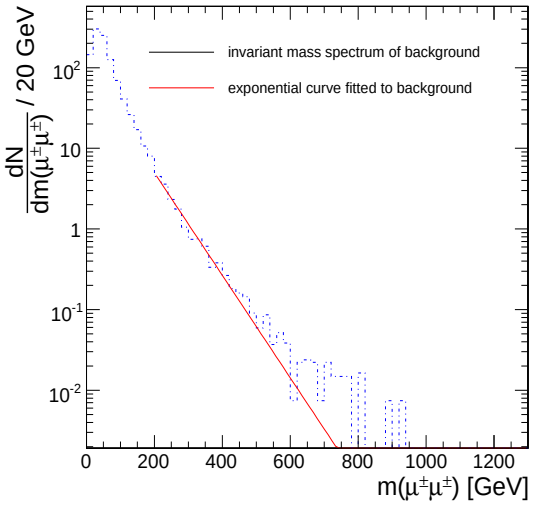

Figure 10.5: Distribution of the invariant reconstructed $H^{\pm\pm}$ mass for all background events at an integrated luminosity of 10 fb^{-1}, and the exponential curve fitted to the background.

2. An exponential decreasing curve is fitted to the reconstructed invariant mass spectrum of the background:
The mass distribution reconstructed from the decay products of a non-resonant state typically follows (at least locally) an exponentially decreasing curve. By fitting an exponential curve to the invariant mass spectrum the number of expected events in the different bins can be estimated. The curve is fitted to the invariant mass spectrum for masses larger than 200 GeV, because below this limit enough background events have been generated and above this limit the invariant mass distribution follows an exponential decreasing function. The fitted curve and the errors on this fit are:

$$\frac{dN}{d(m(\mu^{\pm}\mu^{\pm}))}/20\ \text{GeV} = \exp\left[4.5(\pm 1) - 1.5\cdot 10^{-2}(\pm 4\cdot 10^{-3})\cdot\frac{m(\mu^{\pm}\mu^{\pm})}{\text{GeV}}\right], \quad (10.8)$$

where $m(\mu^{\pm}\mu^{\pm})$ is the reconstructed invariant mass in GeV. Figure 10.5 shows the generated and reconstructed distribution of the invariant mass and the exponential curve fitted to this distribution. The parameters of the exponential curve depend strongly on the mass region chosen for fitting the curve.

Both methods have their advantages and disadvantages. The more conservative method 1 is chosen and applied in this work. The exclusion and discovery limits obtained with

method 2, are taken as an estimate of the systematical error on the number of background events.

10.1.3 Discovery Limit

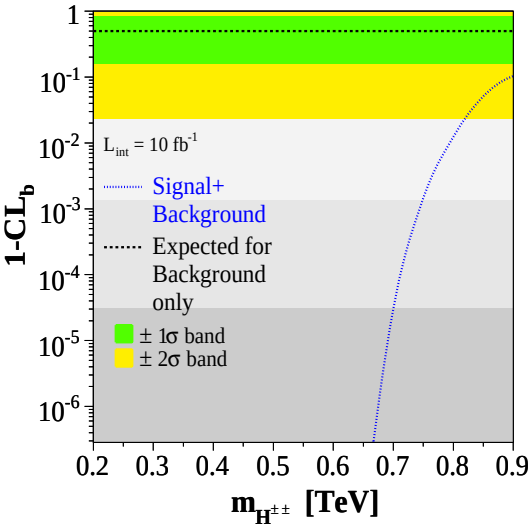

Figure 10.6: $1-\mathrm{CL}_b$ as a function of the reconstructed invariant doubly charged Higgs boson mass, the discovery limit is 650 GeV.

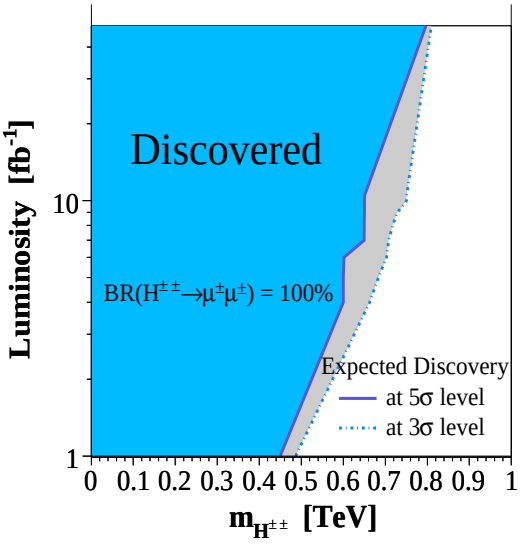

Figure 10.7: The discovery limit as a function of the integrated luminosity. The branching ratio BR($H^{\pm\pm} \to 4\mu$) = 100% is not varied.

Figure 10.6 shows the value of $1-\mathrm{CL}_b$ for different doubly charged Higgs boson masses at an integrated luminosity of 10 fb^{-1}. For masses smaller than 650 GeV the signal plus background expectation exceeds the background only expectation by more than 5σ, and more than four events remain after the final selection. The ± 1 and ± 2 -σ bands are obtained by varying the integration border X_0 of equation 10.4 by ± 1 and ± 2 -σ, where σ is the width of the P_{s+b} distribution (Section 10.1.1). They indicate statistical errors.

In order to investigate the dependency of the discovery limit on the luminosity, the discovery limits for integrated luminosities in the range of 1 - 50 fb^{-1} (Figure 10.7) are calculated. With an integrated luminosity of 1 fb^{-1} a 5σ discovery level can be obtained for a doubly charged Higgs boson mass of 450 GeV, with two detectable events after the final selection. With an integrated luminosity of 50 fb^{-1} the 5σ discovery limit increases up to 800 GeV. Approximatly eight events remain after the final cuts at this integrated luminosity and mass.

10.1.4 Exclusion Limit

Figure 10.8 shows the value of CL_s as a function of the doubly charged Higgs boson mass. If no signal can be detected for an integrated luminosity of 10 fb^{-1} the existence of a doubly charged Higgs boson in the four muon decay channel can be excluded at 95% confidence level up to a mass of 760 GeV. The ± 1 and ± 2 -σ bands indicate the statistical errors and

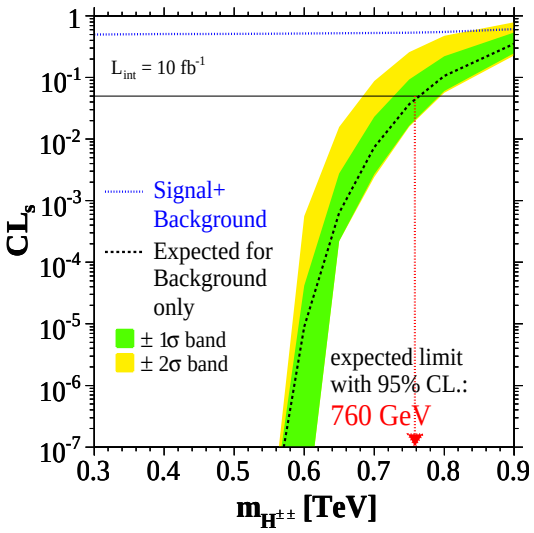

Figure 10.8: CL_s as a function of the reconstructed invariant doubly charged Higgs boson mass, the exclusion limit is 760 GeV.

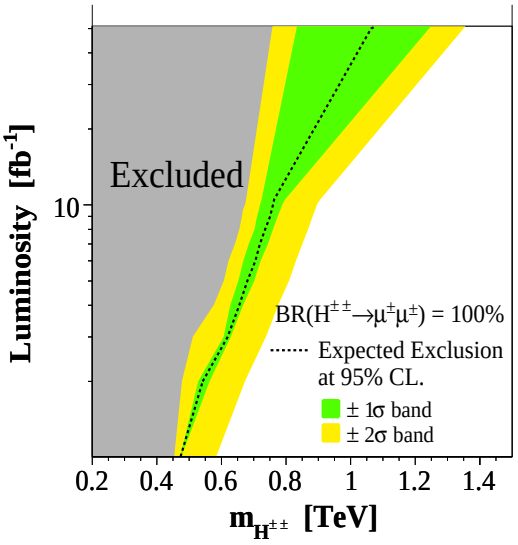

Figure 10.9: The exclusion limit as a function of the integrated luminosity. The branching ratio BR($H^{\pm\pm} \to 4\mu$) = 100% is not varied.

have been obtained by varying the integration border X_0 of equation 10.5 by ± 1 and ± 2 σ, where σ is the width of the distribution P_b. The σ bands are not totally smooth, due to the finite number of investigated doubly charged Higgs boson masses. For each investigated mass point the σ values are calculated, in the region between these mass points the σ bands are extrapolated. Nevertheless the exclusion mass limit is nearly unaffected by this, due to the small steps of only 50 GeV in which the doubly charged Higgs boson mass is varied in the interesting region between 550 and 800 GeV.

The dependency of the exclusion limit on the luminosity is shown in Figure 10.9. With an integrated luminosity of only 1 fb^{-1} an exclusion limit at 470 GeV can be set, in the case that no signal will be discovered.
With 50 fb^{-1} the 95% confidence limit increases up to 1 TeV.

Figure 10.10 shows the exclusion limit for different branching ratios of the doubly charged Higgs boson into two muons. For example, equal branching ratios into $\mu\mu$, $\mu\tau$ and $\tau\tau$ could be assumed. Using the resulting branching ratio of pair produced Higgs bosons into four muons BR($H^{++} + H^{--} \to 4\mu$) = 1/3, an exclusion limit of $\approx$ 410 GeV can be set, if after the appliciation of the presented selection cuts no signal can be detected. This decay mode is discussed in [54], with respect to "The Higgs Triplet Model" and recent results on neutrino mass parameters.

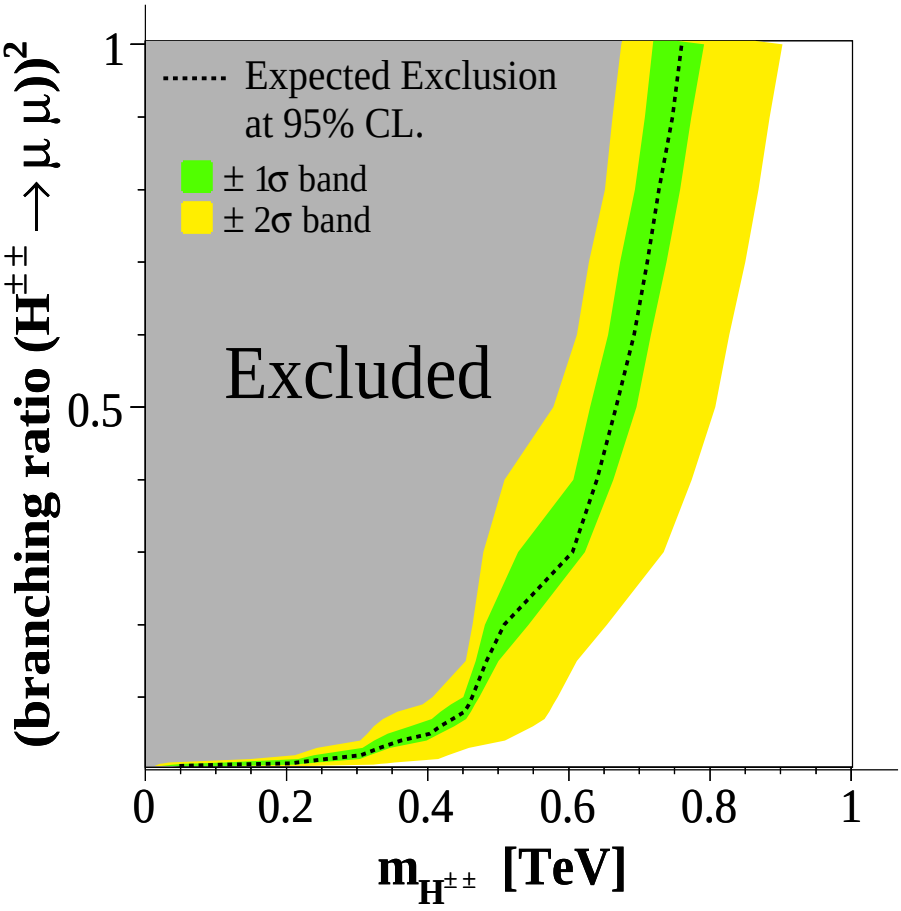

Figure 10.10: The exclusion limit as a function of the branching ratio squared.

Chapter 11

Systematic Uncertainties

The systematic errors which might affect this analysis have to be studied in detail once the detector is taking data. Here only rough estimations of the resulting uncertainties on exclusion and discovery limits are given. These estimations are useful to obtain a forecast on the relative importance of the different systematic errors for this analysis.

Associated with the production rates are:

- the uncertainties of the parton density functions and QCD scales at NLO,
- the uncertainty on the LHC luminosity,
- the uncertainty due to the lack of simulated background events (see section 10.1.2).

Associated with the CMS detector performance (hardware/software) and analysis-specific cuts are:

- the uncertainties of the trigger efficiencies,
- the uncertainty of the muon reconstruction efficiency,
- the uncertainty of the efficiency of the Impact Point cut,
- the uncertainty on the resolution of the reconstructed doubly charged Higgs Boson mass.

The uncertainty on the background cross section related to parton density functions and QCD scales have been taken from studies of the Standard Model $H \to ZZ \to 4\mu$ process. $H \to ZZ \to 4\mu$ and $H^{++}H^{--} \to 4\mu$ have the same background processes. $H \to ZZ \to 4\mu$ is one of the benchmark processes of the future CMS detector and is therefore studied in detail (see for example [55]). The uncertainty obtained on the background cross section is 1% to 6% [56].

The uncertainties on the signal production, which are related to the NLO corrections and to the parton density functions have been calculated by Spira and Mühlleitner to be 10% to 15% [13].

The uncertainty on the luminosity for the first few years of data taking is estimated to be 5% [55].

In [57] it is explained how the muon reconstruction efficiency should be obtained from data, using the Single-Muon HLT with $p_T > 19$ GeV. The uncertainty should be smaller than 1%.

The muon trigger efficiency, being very close to 100% due to the presence of four muons, should not have substantial systematic errors.

The efficiency of the Impact Point cut could possibly also be evaluated by data, using the inclusive Z sample and minimum bias events. This has yet to be studied in detail.

The resolution of the reconstructed doubly charged Higgs boson mass has been studied in section 7.2.1. The uncertainty of the resolution and the implication on the exclusion limit still need to be studied.

11.1 Approximated total uncertainties

Assuming a total systematic error on the background cross section $\sigma_{background}$ of 6%, using an uncertainty of 5% on the luminosity and an uncertainty on the signal cross section σ_{signal} of 10%, the systematic errors on exclusion and discovery limits can be approximated as:

$$\text{Exclusion Mass Limit} = (760\ ^{+0.5}_{-2}(\sigma_{background}) \pm 10(\sigma_{signal}) \pm 4(\mathcal{L}))\ \text{GeV} \quad (11.1)$$

$$\text{Discovery Mass Limit} = (650\ ^{+0.4}_{-0.3}(\sigma_{background})\ ^{+3}_{-0.4}(\sigma_{signal}) \pm 0.2(\mathcal{L}))\ \text{GeV} \quad (11.2)$$

If the less conservative method 2 of section 10.1.2 is used, the exclusion and discovery limit improve to 800 GeV and 900 GeV, respectively. At 900 GeV only one event remains after all cuts. To obtain at least three detectable events, at an integrated luminosity of 10 fb^{-1}, the doubly charged Higgs boson mass has to be smaller than 700 GeV. The variation in the exclusion and discovery mass limit, for the different methods used to estimate the background contribution, can be regarded as systematic uncertainty, due to the lack of simulated background events for higher doubly charged Higgs boson masses.

Chapter 12

Conclusions

A feasibility study for the discovery of pair produced doubly charged Higgs bosons with the full detector simulation has been presented. A branching ratio of 100% into muons has been assumed. The doubly charged Higgs boson mass, which is the only free parameter for pair produced doubly charged Higgs bosons, has been investigated in the range 100 to 900 GeV. All Standard Model background processes have been taken into account. According to the low luminosity phase of the LHC ($\mathcal{L} = 2 \cdot 10^{33}\text{cm}^{-2}\text{s}^{-1}$), on average 3.5 pileup events have been mixed with the signal and background samples. For signal and background NLO cross sections have been used. Due to the decay of each doubly charged Higgs boson into two equally charged muons this process provides a very characteristic signature and is almost background free.

It has been shown, that pairproduced doubly charged Higgs Bosons with a branching of 100% into muons, can be discovered (5σ) with an integrated luminosity of 10fb^{-1} in the mass range of 100 to 650 GeV. If no signal is visible at CMS, an exclusion limit at 95% CL of $m_{H^{\pm\pm}} = 760$ GeV can be set. This improves the current exclusion limit for this channel of $m_{H^{\pm\pm}} \leq 136$ GeV, set by CDF at Tevatron Run II, by 624 GeV.

Systematic uncertainties resulting from higher order cross sections, parton density functions and scale dependencies have been calculated for the signal [13]. The systematic uncertainties of the backgrounds have been taken from studies of the Standard Model process $H \to ZZ \to 4\mu$, which has the same backgrounds and is studied in detail as a benchmark process for the CMS detector.

Appendix A

A.1 Units

The variables used in this thesis are given in natural units. Natural units are defined by:

$$\hbar \equiv 1 \tag{A.1}$$

$$c \equiv 1 \tag{A.2}$$

Therefore energy, mass, momentum, 1/time and 1/length can be displayed with the same unit. The unit chosen by convention is eV, which is the energy gained by an electron moving through a potential difference of one volt. In the "International System of Units" an energy of one eV corresponds to:

$$1 \text{ eV} = 1.602176462(63) \cdot 10^{-19}\text{J} \tag{A.3}$$

The electrical charge is given in units of the "elementary electrical charge" e, which is the charge of the electron.

A.2 Conventions

Throughout the analysis the summation convention of Einstein has been used. Repeated indices one up one down, such as in equation A.4, are implicitly taken to be summed. Example:

$$u^i e_i \equiv \sum_{i=1}^{m} u^i e_i \tag{A.4}$$

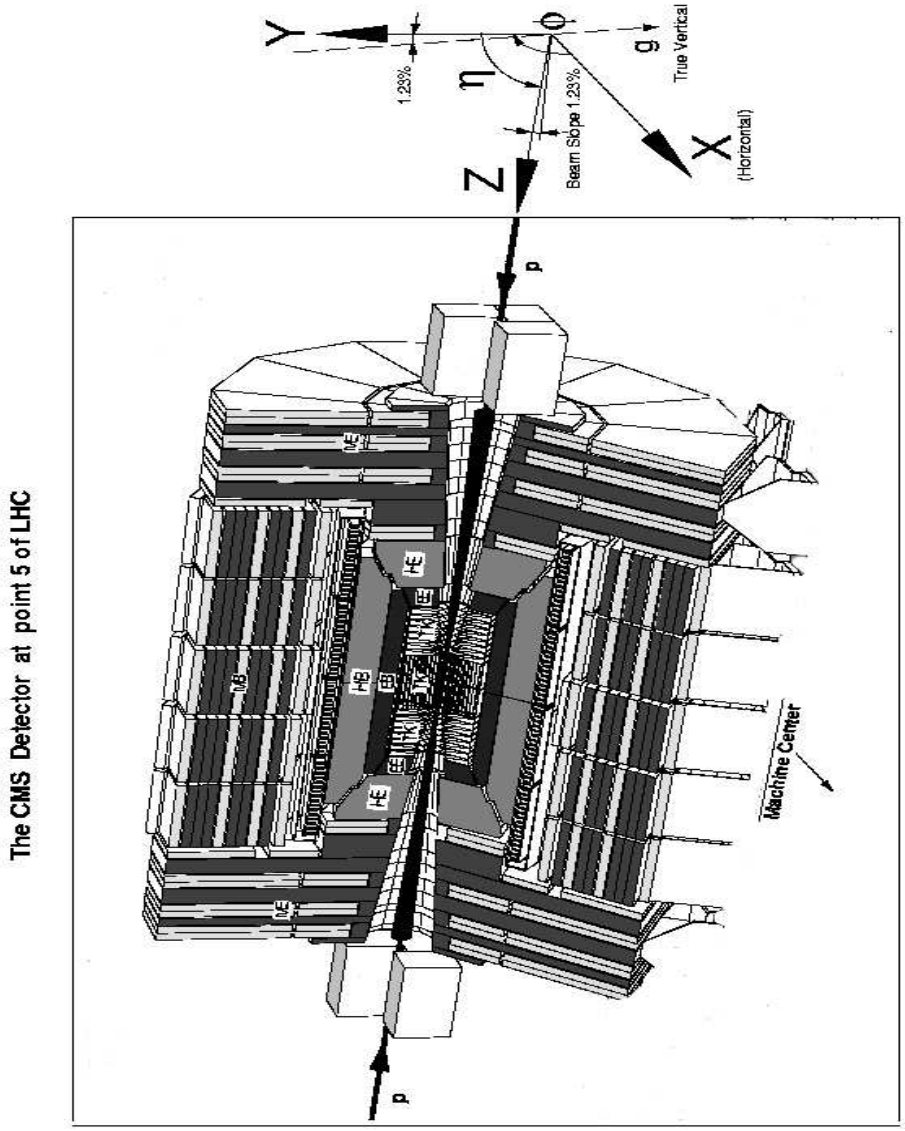

Figure A.1: The CMS coordinate system. Taken from [58] and modified.

A.3 Coordinate System

The CMS coordinate system is shown in figure A.1. The cartesian system (x,y,z) is right handed, with the nominal interaction point as origin and the x-axis pointing towards the center of the LHC ring. The polar coordinates are defined by:

$$\phi = \arctan\left(\frac{x}{y}\right) \tag{A.5}$$

$$\theta = \arccos\left(\frac{z}{\sqrt{x^2+y^2}}\right) \tag{A.6}$$

A.4 Kinematic Quantities

Definition of some often used kinematic quantities:

- Pseudorapidity η

$$\eta = -\ln\left(\tan\left(\frac{\theta}{2}\right)\right) \tag{A.7}$$

- Transverse Momentum p_T:

$$p_T = \sqrt{(p_x)^2 + (p_y)^2} \tag{A.8}$$

A.5 Background samples

Official sample	# generated and preselected events
mu03_tt_4mu	95 000
mu03e_zbb_4mu_compHEP	100 000
mu03e_zz_zmu_4mu_compHEP	118 000
mu03d_zz_zmu_2mu_2tau_compHEP	1 000
bt03_b_pt30-50	150 000
bt03_b_pt50-80	150 000
bt03_b_pt80-120	150 000
bt03_b_pt120-170	150 000
bt03_b_pt170up	150 000

Table A.1: The different background samples

A.6 CMKIN card

An example CMKIN card used to produce the signal sample $m_{H^{\pm\pm}} = 200$ GeV.

```
C
C Data card:
C
C     Hpp --> mu mu
C     ============
C
C     Hpp mass = 200 GeV
C
C defined by Tanja Rommerskirchen 24.06.200 (rommersk@physik.rwth-aachen.de)
C
C

LIST

C
C Pythia parameters
C -----------------
C
C  Specify output file:

   CFIL 'EVTO' 'mcevents_Hpp_200_mumu.ntpl'

C --------------
C Set RUN number
C --------------

   KRUN 001

C --------------------------
C PYTHIA Particle Properties
C --------------------------

   PMAS 5,1 = 4.8            !mass of b quark
   PMAS 6,1 = 175.0            !mass of top quark


   PMAS 353,1 = 200           ! mass of Hlpp
   PMAS 354,1 = 200           ! mass of Hrpp

C ------------------------
C PYTHIA Process Selection
C ------------------------

   MSEL = 0                  ! Hlpp production
   MSUB 349  = 1
   MSUB 351  = 0

C   PARP 181 = 0
C   PARP 182 = 0
C   PARP 183 = 0
```

```
C   PARP 184 = 0
C   PARP 185 = 0.1
C   PARP 186 = 0
C   PARP 187 = 0
C   PARP 188 = 0
C   PARP 189 = 0

C Switch off all Hlpp decay channels beside Hlpp --> mu mu



   MDME 4271, 1 = -1            ! Hl --> e + e
   MDME 4272, 1 = -1            ! Hl --> e + mu
   MDME 4273, 1 = -1           ! Hl --> e + tau
   MDME 4274, 1 = 1            ! Hl --> mu + mu
   MDME 4275, 1 = -1           ! Hl --> mu + tau
   MDME 4276, 1 = -1            ! Hl --> tau + tau
   MDME 4277, 1 = -1            ! Hl --> W + W



   MSTJ 11 = 3           !Choice of the fragmentation function
   MSTP 2 = 1           !which order running alphaS
   MSTP 33 = 0           !(D=0) inclusion of K factors in hard cross sections for parton-parton
   MSTP 51 = 7           !structure function chosen
   MSTP 81 = 1           !multiple parton interactions 1 is Pythia default
   MSTP 82 = 4           !Defines the multi-parton model
   PARJ 71 = 10.           !for which ctau  10 mm
   PARP 82 = 1.9           !pt cutoff for multiparton interactions
   PARP 89 = 1000.           !sqrts for which PARP82 is set
   PARP 83 = 0.5           !Multiple interactions: matter distrbn parameter Registered by Chris
   PARP 84 = 0.4           !Multiple interactions: matter distribution parameter Registered by
   PARP 90 = 0.16           !Multiple interactions: rescaling power Registered by Chris.Seez@ce



C
C -----------------
C PYTHIA Kinematis
C -----------------


C --------------
C PYTHIA Trigger
C --------------


C ---------
```

```
C GENERATOR
C ---------

   KSEL = 0                  !similar to Pythia's MSEL
   NSEL = 5000              !maximal number of subevents per AA event (hier einstellen wieviele Events
   TRIG = 100000            !maximum number of tries
   ECMS = 14000              !center of mass energy
   MRPY 1 = 1293894893948           !random seed for PYTHIA

   PARP 85 = 0.33            !gluon prod. mechanism in MI Registered by Alexandre.Nikitenko@cern.ch
   PARP 86 = 0.66            !gluon prod. mechanism in MI Registered by Alexandre.Nikitenko@cern.ch
   PARP 87 = 0.7            ! Registered by Alexandre.Nikitenko@cern.ch
   PARP 88 = 0.5            ! Registered by Alexandre.Nikitenko@cern.ch
   PARP 91 = 1.0            !kt distribution Registered by Alexandre.Nikitenko@cern.ch


C ------------------
C PYTHIA Rarely used
C ------------------

END
EOF
```

Bibliography

[1] Collaboration, CMS: *CMS Physics - Technical Design Report*. Vol. I. CERN/LHCC 2006, 2005

[2] P.Schmüser: *Feynman-Graphen und Eichtheorien fuer Experimentalphysiker*. Vol. 2. Springer, August 1994. – ISBN 3–540–58486–2

[3] C.Berger: *Elementarteilchenphysik*. Springer, 2002. – ISBN 3–540–41515–7

[4] M.Zöller. *Suche nach dem Higgs-Boson in hadronischen Endzustaenden mit fehlender Energie bei LEP*. 2005

[5] K.Zuber: Neutrino Physics. (2003). ISBN 0–7503–0750–1

[6] A.Strumia ; F.Vissani: Implications of neutrino data circa 2005. . – arXiv:hep-ph/0503246 v1

[7] T.Hebbeker: Elementarteilchenphysik II RWTH Aachen, Neutrinooszillationen III. *http://www.physik.rwth-aachen.de/ hebbeker/lectures/p245/p245_l09.pdf* (WS 2004/2005)

[8] A.G.Akeroyd ; M.Aoki: Single and Pair Production of Doubly Charged Higgs Bosons at Hadron Colliders. (2005), June. – arXiv:hep-ph/0506176v2

[9] K.Huitu, *et al.*: Doubly charged Higgs at LHC. . – arXiv:hep-ph/9606311 v1

[10] J.F.Gunion, *et al.*: Higgs Bosons in Left-Right-Symmetric Model. *Phys. Rev. D* 40 Number 5

[11] W.Grimus: Introduction to left-right symmetric models. *Invited talk at Lectures given at 4th Hellenic School on Elementary Particle Physics, Corfu, Greece* (1992), September

[12] J.F.Gunion ; H.E.Haber ; G.Kane ; S.Dawson: *The Higgs Hunter's Guide*. Addison-Wesley Publishing Company, 1990

[13] M.Mühlleitner ; M.Spira: A Note On Doubly-Charged Higgs Pair Production at Hadron Colliders. *PSI-PR-03-07* (2003), May. – hep-ph/0305288

[14] Collaboration., L3: Search for Doubly-Charged Higgs Bosons at LEP. *CERN-EP/2003-060* (2003), September. – hep-ex/0309076 v1

[15] Collaboration., CDF: Search for Doubly-Charged Higgs Bosons Decaying to Dileptons in $p\bar{p}$ Collisions at $\sqrt{s} = 1.96$ TeV. *Phys.Rev.Lett. 93(2004)221802* (2004). – hep-ex/0406073

[16] Collaboration., CDF: Search for the Quasi-Stable Doubly Charged Higgs Using the Two-Track Signature. *CDF Note 7155* (2004), July

[17] DESY: TESLA, an international, interdisciplinary center for research. `http://tesla.desy.de/new_pages/TDR_CD/brochure` (2001)

[18] The QCD and Standard Model Working Group: Summary Report. (2000), May. – arXiv:hep-ph/0005114

[19] Collaboration, CMS: *The Level-1 Trigger - Technical Design Report.* Vol. I. CERN/LHCC 2000-038, December 2000

[20] LHC Machine Outreach. `http://lhc-machine-outreach.web.cern.ch/lhc-machine-outreach`

[21] . – `http://cmsinfo.cern.ch/outreach/CMSdocuments/DetectorDrawings`

[22] Collaboration, CMS: *The Tracker System Project - Technical Design Report.* CERN/LHCC 94-38, December 1994

[23] Collaboration, CMS: *The Hadron Calorimeter Project - Technical Design Report.* CERN/LHCC 97-31, June 1997

[24] Collaboration, CMS: *The Muon Project - Technical Design Report.* CERN/LHCC 97-32, December 1997

[25] M.Bontenackels ; H.Reithler: Private Communications.

[26] Collaboration, TOTEM: *TOTEM - Technical Design Report.* CERN/LHCC 2004-002, 2004

[27] Collaboration, CMS: *The Trigger and Data Acquisition Project - Technical Design Report.* Vol. II. CERN/LHCC 2002-026, December 2002

[28] T.Sjostrand ; L.Lonnblad ; S.Mrenna: PYTHIA 6.2: Physics and manual. (2001). – hep-ph/0108264

[29] G.Marchesini, *et al.*: HERWIG: A Monte Carlo event generator for simulating hadron emission reactions with interfering gluons. Version 5.1 - April 1991. *Comput. Phys. Commun.* 67, p. 465–508

[30] S.R.Slabospitsky ; L.Sonnenschein: TopReX generator (version 3.25). Short manual. *Computer Physics Communications* 148 (2002), January, p. 87. – arXiv:hep-ph/0201292

[31] CMKIN Project Page. `http://cmsdoc.cern.ch/cmsoo/projects/CMKIN/index.html`

[32] FORTRAN. `http://www.fortran.de`

[33] A.Pukhhov ; E.Boos ; M.Dubinin, *et al.*: CompHEP- a package for evaluation of Feynman diagrams and integration over multi-particle space, User′s manual for version 33. (1999). – arXiv:hep-ph/9908288

[34] OSCAR. `http://cmsdoc.cern.ch/oscar`

[35] S.Agostinelli, *et al.*: GEANT4: A simulation toolkit. *Nucl. Instrum. Meth.* A506 (2003), p. 250–303

[36] ORCA - USER GUIDE. `http:// cmsdoc.cern.ch/orca` (2005)

[37] PAX. `http://pax.home.cern.ch/pax/`

[38] M.Erdmann, *et al.*: Physics Analysis eXpert, Users Guide. `http://cern.ch/pax` (2005), November

[39] Collaboration, CMS: *The Computing Project - Technical Design Report.* CERN/LHCC 2005-023, June 2005

[40] LCG. `http://lcg.web.cern.ch/LCG/`

[41] C.Zecher, *et al.*: Leptonic Signals from off-shell Z Boson Pairs at Hadron Colliders. (1994). – Z.Phys. C64 (1994) 219-226

[42] F.Maltoni: Theoretical Issues and Aims at the Tevatron and LHC, talk on HCP2005. `http://hcp-2005.web.cern.ch` (2005), 08. Juli

[43] Group, Particle D.: *Particle Physics Booklet.* LBNL and CERN, July 2004

[44] J.M.Campbell: W/Z + B anti-B/jets at NLO using the Monte Carlo MCFM. . – arXiv:hep-ph/0105226

[45] P.Bartalini ; H.Stenzel ; A.Sherstnev: CMS note in preparation, presented by A. Korytov at the $H \rightarrow ZZ^{(*)} \rightarrow 4l$ meeting. `http://indico.cern.ch/conferenceDisplay.py?confId=a061694`

[46] F.Maltoni ; T.Steltzer: MadEvent: Automatic Event Generation with MadGraph, JHEP 0302(2003).

[47] A.Drozdetskiy: Brief note on x-sections, K-factors, event weights. (2005), December

[48] P.Eraerds: Analysis of Mono-jet Events at the Tevatron. (2006). – Diploma thesis in Physics

[49] CMS OO Reconstruction. `http://cmsdoc.cern.ch/orca`

[50] CMS Computing Production. `http://cmsdoc.cern.ch/cms/production/www/html/general/`

[51] A.L.Read: Presentation of Search Results: The CL_S Technique. . – J. Phys. G28 (2002) 2693-2704

[52] E.Gross ; A.L.Read: Prospects for Standard Model Higgs Search in the LEP 2000 Run. (2000). – Proceedings of 14th Rencontres de Physique de la Valle d'Aoste: Results and Perspectives in Particle Physics

[53] A.L.Read: Modified Frequentist Analysis of Search Results (The CL_s Method). . – Prepared for Workshop on Confidence Limits, Geneva, Switzerland (2000)

[54] M.Kadastik: Doubly Charged Higgs Boson Decay To Muons At The LHC. (2005). – Master's Thesis

[55] Collaboration, CMS: *CMS Physics - Technical Design Report 2.* Vol. II. CERN/LHCC 2006, 2005

[56] M.Aldaya, *et al.*: Search for the Standard Model Higgs boson in the H→ZZ→4μ decay channel using a mass-independent analysis. (2006). – CMS AN-2006/049

[57] S.Beauceron, *et al.*: Search for $H \to 4\mu$ using M(4mu)-dependent cuts. (2006). – CMS AN-2006/055

[58] Collaboration, CMS: *The Electromagnetic Calorimeter Project - Technical Design Report.* CERN/LHCC 97-33, December 1997

[59] E.J.Chun ; K.Y.Lee ; S.C.Park: Testing Higgs Triplet Model and Neutrino Mass Patterns. . – arXiv:hep-ph/0304069

[60] N.G.Deshpande, *et al.*: Left-right-symmetric electroweak models with triplet Higgs field. *Phys. Rev. D* 44 Number 3 (1991), August

[61] F.Halzen ; A.D.Martin: *Quarks and Leptons: An introductory Course in Modern Particle Physics.* John Wiley & Sons, February 1984. – ISBN 0–471–88741–2

[62] A.Favara ; M.Pieri: Optimal statistical Analysis of search Results. (1997). – L3 Internal Note 2066

[63] W.Grimus: Introduction to left-right symmetric models. *Invited talk at Lectures given at 4th Hellenic School on Elementary Particle Physics, Corfu, Greece* (2-20 Sep, 1992)

[64] IguanaCMS. `http://iguanacms.web.cern.ch/iguanacms`

[65] ORCA Software Cross-Reference. `http://cmsdoc.cern.ch/swdev/lxr/ORCA/source/ORCA/`

Acknowledgements

In the first place I want to thank my parents, who always believed in me and supported me in life and work. Even in the last year, which was a hard time for all of us, I knew I could always trust on them. They teached me that it is not so important what your job is as long as you do your very best in it and you do it wholeheartedly. I hope I was successful in following their advice with this thesis.

I would like to thank all the people who contributed to the completion of my diploma thesis:

First of all I want to thank Prof.Dr.Thomas Hebbeker not only for offering me this analysis as task for my diploma thesis but much more for his continuous support, which I think is in no way self-evident. He not only organized regular meetings where a lot of open questions could be solved and the right new questions were asked, but he gave me also the opportunity and the assistance to publish a note about my topic and to contribute to the PTDR II. Thanks.

Furthermore I am grateful to Prof.Dr.Martin Erdmann for being my second referee and contributing to the powerful analysis tool used in this diploma thesis, PAX.

For cross-reading my diploma thesis but much more for never loosing the patience with me and my never ending questions, I would like to thank Philipp Biallass, Carsten Hof, Michael Bontenackels and Patrick Eraerds.

Thanks also to my room mate and fellow diploma student Clemens Zeidler, for the support and the fruitful cooperation.

A special thanks goes out to Thomas Kress, Andreas Nowack and to all the other people who constantly spend their time with mending and improving our computing systems. Without their help and support this analysis would have been impossible.

I would also like to thank all the members of the CMS collaboration, who contributed to the software used within this analysis and who supported my note and my contribution to the PTDR II. I am especially grateful to Alexandre Nikitenko, Alexey Drotzdetskiy, Marc Zoeller, Mario Kadastik, Martti Raidal, Michael Spira, Norbert Neumeister, Sami Lehti and Torbjorn Sjostrand for their discussions and assistance and to my referees Pablo Garcia Abia, Guenakh Mitselmakher, Nancy Marinelli and Roberto Tenchini.

For the organization of so many trips during this last year I would like to thank Irene Gojdie, Iris Rosewick and Kirstin Erner.

Finally I want to thank a very special person, who gave me strength when I needed it the most.